W. Zhang

# Stochastic Modelling and Numerical Simulation of Fatigue Damage

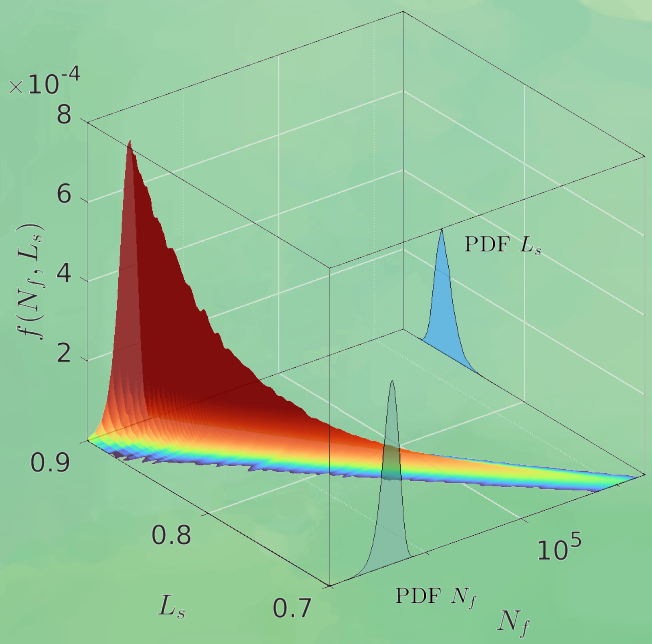


F 21/02
Institut für Baumechanik
und Numerische Mechanik
Gottfried Wilhelm Leibniz Universität Hannover

**Hauptreferent:**
*Prof. Dr.-Ing Udo Nackenhorst*

**Korreferent:**
*Prof. Dr. Amélie Fau*

**Doktorand:**
*M.Sc. Weiran Zhang*

# Stochastic Modelling and Numerical Simulation of Fatigue Damage

Von der Fakultät für
Bauingenieurwesen
und Geodäsie der
Gottfried Wilhelm Leibniz
Universität Hannover

zur Erlangung des Grades eines

*Doktor-Ingenieurs*

genehmigte Dissertation
von

*M.Sc. Weiran Zhang*

Hannover 2021

Tag der Einreichung:
16.06.2020
Tag der mündl. Prüfung:
11.11.2020

**Institut für
Baumechanik
und Numerische
Mechanik**

Herausgeber:
Prof. Dr.-Ing. Udo Nackenhorst

Verwaltung:
Institut für Baumechanik
und Numerische Mechanik
Gottfried Wilhelm Leibniz
Universität Hannover
Appelstraße 9A
30167 Hannover
Tel.: +49(0)511/762−3219
Fax.: +49(0)511/762−19053


Verwaltung:
Institut für Baumechanik
und Numerische Mechanik
Gottfried Wilhelm Leibniz
Universität Hannover
Appelstraße 9A
30167 Hannover



ISBN 978-3-935732-54-3

# Acknowledgment

First of all, I would like to express my sincere gratitude to Professor Udo Nackenhorst for his guidance and the financial support arranged by him from the German Research Foundation (DFG). He offered me the opportunity to participate in the International Research Training Group (IRTG) 1627, to cooperate with the Laboratoire de Mécanique et Technologie (LMT) at Université Paris-Saclay in Paris, and to work as a research assistant at the Institute of Mechanics and Computational Mechanics (IBNM). These experiences will fundamentally influence my professional career.

Meanwhile, I would like to thank Professor Amélie Fau warmly for her advice while working together in Hanover, Germany, and her effort being one of the examiners of this manuscript. I thank her contribution to the journal publication, and I remember the time we spend together talking about the research progress. I thank Professor Raimund Rolfes for chairing the promotion committee, and I appreciate Professor Dominik Schillinger and Professor Michael Beer for their active participation.

My special appreciation is given to Professor Rodrigue Desmorat for his guidance on damage mechanics during my research exchange in Paris, France. We used to have scientific discussions in a coffee bar near the subway station Denfert-Rochereau.

In the past few years, my great pleasure was to work in the IBNM team. Thank Alena for her help and patient support regarding the calculation of working travel costs and Daniel for the rapid troubleshooting with his proficient IT skills. Especially I want to thank Stefanie and Mohammed H. for sharing the office "Zi.116" with me and taking care of the plants when I was absent for business trips. I also want to thank Paula for the nice graphically designed latex template, which I used in my defence presentation. Meanwhile, I have many good memories of the institute seminars, Christmas parties, grill evens, free talks during every day's coffee break and lunch hour. I hereby deeply appreciate all my IBNM-colleagues, who are the creators of these memorable stories.

In the end, I want to thank my friends and family for encouraging me to overcome difficulties and bringing happiness into my life.

Hannover, July 2021

*Weiran Zhang*

# Abstract

A phenomenological damage modelling approach based on the stochastic process is proposed to reproduce the strongly scattered fatigue data. In this work, a concrete beam under four-point bending is computed using the finite element method. The stochastic damage evolution is modelled as a random process and produced by the Monte-Carlo method. The virtual flexural fatigue life of the quasi-brittle material is compared with experimental data and empirical estimation results. For high-cycle fatigue problems, the efficient "jumping-cycle" algorithm is implemented to reduce the computational cost. This modelling approach enables the simulation of the fatigue process with probabilistic information in an extensive time interval.

In continuum damage mechanics (CDM), fatigue is a phenomenon associated with a degeneration of material integrity, e.g. a continuous material stiffness reduction. Numerically, it can be simulated as an accumulation of damage process. Since the resistance of concrete material reduces drastically after the initiation of macroscopic cracks, fatigue life can be approximated using damage models as the number of cycles by which the material continuity vanishes. The fatigue scatter is an interpretation of material heterogeneity and uncertain external influences. It can be reproduced by treating the damage evolution as a stochastic process.

Inspired by the application of the stochastic process in molecular physics, the deterministic damage evolution rate of the Lemaitre model is modified as a stochastic differential equation to characterise the random damage increment. The implicit Euler scheme associated with Monte-Carlo simulation is demonstrated as a practical approach to solve the stochastic integration problem. The stochastic damage model is designed carefully to obey the thermodynamic principles and the deterministic damage law. Particular efforts are addressed to determine suitable random distributions, avoiding negative random damage increments in individual realisations, to have a statistically unbiased mean. To adequately approximate the high-cycle fatigue damage with random noise, the "jumping-cycle" algorithms with different extrapolation strategies are investigated.

As a highlight of this study, this damage model is further implemented in the simulation of four-point flexural fatigue of concrete beam, solved by the finite element method. The numerically reproduced fatigue data closely fit the published experimental results and the empirical solution, both in the mean and standard deviation. Compared to the Gaussian white noise, the Weibull random variable has broad applicability to simulate random fatigue damage and other physical processes.

**Keywords** Stochastic Process, Fatigue Damage, Finite Element Method, Monte-Carlo Simulation

# Zusammenfassung

Um die Streuung der Messdaten in der Materialermüdung zu beschreiben, wird basierend auf Zufallsprozessen ein phenomenologische Modellierung vorgestellt. Erprobt wird die Modellierung an einem Betonbalken mit ebener Finite Element Diskretisierung, wobei die stochastischen Ermüdungsgleichungen mit der Monte Carlo Methode gelöst werden. Die simulierten Ermüdungsprozesse unter Biegebeanspruchung des quasi-spröden Materials werden mit experimentellen Daten und etablierten empirischen Gleichungen vergleichen. Um hochzyklische Beanspruchungen zu behandeln, wird ein „jumping-cycle“ Algorithmus angewendet, mit dem die Rechenzeiten stark reduziert werden. Dieser Modellansatz ermöglicht die Simulation von Ermüdungsprozessen mit probabilistischen Information in einem sehr langen Zeitintervall.

In der Kontinuums-Modellierung geht der Prozess der Materialermüdung mit einer Degeneration der materiellen Integrität einher, die sich z.B. in der Abnahme des elastischen Moduls niederschlägt. Numerisch wird dies als ein kumulativer Schädigungsprozess modelliert. Weil der Materialwiderstand von Beton nach der Entstehung makroskopischer Risse drastisch abnimmt, kann die Ermüdungslebensdauer unter zyklischer Beanspruchung durch ein Schädigungsmodell praktisch sehr gut abgeschätzt werden, sobald das Auftreten makroskopischer Risse prognostiziert wird. Die Streuung in experimentell ermittelten Ermüdungskurven kann durch die mikro-Heterogenität der Materialien und Unsicherheiten in weiteren externen Faktoren verstanden werden, mittels einer Modellierung der Schädigungsentwicklung als stochastische Prozessgleichungen kann diese gut reproduziert werden.

In Anlehnung an die Beschreibung stochastischer Prozesse in der theoretischen Physik werden die Evolutionsgleichungen für die Schädigungsentwicklung des Lemaitre-Modells als stochastische Differentialgleichungen dargestellt. Diese werden mittels impliziter Euler-Verfahren und Monte-Carlo Methoden effizient gelöst. Um die thermodynamische Konsistenz sicherzustellen, insbesondere negative Inkremente der Schädigungsentwicklung zu vermeiden, und unverzerrte statistische Mittel-werte zu erhalten, werden klassische Gaußsche Prozesse durch Weibull-Verteilungen substituiert. Für hochzyklische Belastungen werden „jumping-cycle“ Algorithmen hinsichtlich der Extrapolations-strategien systematisch untersucht.

Am Beispiel eines Betonträgers unter Biegebeanspruchung wird das Ermüdungsverhalten simuliert und mit experimentellen Ergebnissen aus der Literatur und empirischen Formeln vergleichen. Der vorgeschlagene Modellierungsansatz zeigt eine gute Übereinstimmung der Mittelwerte und Standardabweichungen mit den publizierten Erkenntnissen. Wenngleich die hier verwendete Weibull-Statistik im strengen mathematischen Sinne nicht konsistent sein sollte, hat sich diese jedoch als physikalisch konsistent erwiesen, um streuende Ermüdungsschädigung effizient zu beschreiben.

**Stichworte** Zufallsprozesse, Ermüdungsschädigung, Finite-Elemente-Methode, Monte-Carlo Verfahren

# Contents

# Chapter 1

# Introduction

## 1.1 Motivation

The mechanical performance of concrete is significantly influenced by its components, e.g. the size and type of aggregates, the mixing ratio between aggregates and the binder material, etc. The level of heterogeneity of concrete material depends on the atomistic behaviour on the nano-scale and the existing microstructure. By controlling the production process, one can produce concrete with desired properties for civil engineering applications. An example is to add steel fibre reinforcement into the binding material to improve the tensile and the shear performance of concrete-made structures. Even though this is an undergoing process, the use of concrete in engineering practices may lead to safety risks, e.g. the degradation of material stiffness. Therefore, a systemic understanding of its mechanical performance from the reliability perspective is of great importance.

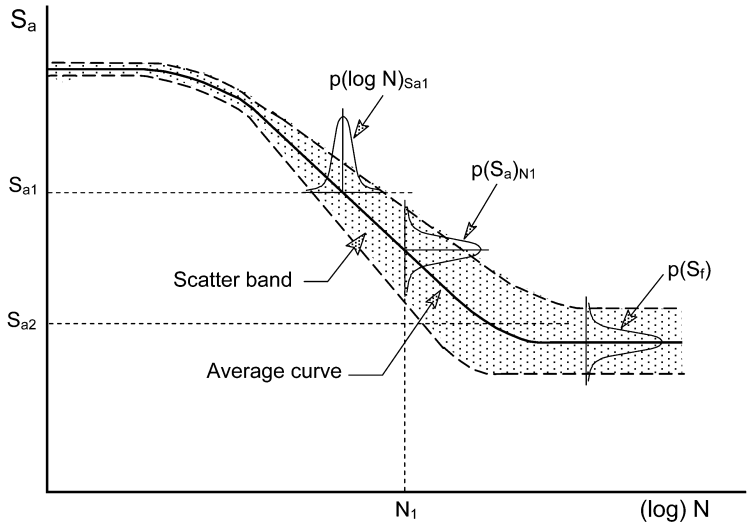


Figure 1.1: An S-N diagram with scattered fatigue data and statistical information [1]

One common type of failure in concrete is fatigue, which is a phenomenon of material stiffness reduction under cyclic load. From the perspective of material continuity, it is an accumulative

process of microcracks [2]. Fatigue appears in the applications such as high-way, railway bridges and wind turbines, where the load repeats periodically. Once the macroscopic crack appears, the service time of the concrete structure can be shortened drastically. Because classical material has no self-repairing ability, the macro cracks can propagate quickly in the direction towards the highest stress concentration till a catastrophic failure. Therefore, to predict the microcrack initiation in terms of the location and elapsed time is the key for fatigue life estimation of concrete structures. Due to the material heterogeneities at the micro and nanoscales, the uncertain external factors in reality, e.g. random load, environmental fluctuation, experimental fatigue data, contain considerable randomness. These factors lead to uncertain fatigue performance, which is often captured as fatigue scatters (see fig. 1.1). Often the horizontal and vertical directions on the S-N diagram denote the loading levels and the fatigue life. Statistically, it is possible to gain the probabilistic fatigue information with a sufficient amount of data. The fitted empirical relation can be used as a reference to analyse the structural reliability. However, the resistance of concrete under compression is by nature much greater than under tension and shear. This phenomenon is named the unilateral effect. The empirical S-N relation, which represents a particular laboratory configuration, can be less reliable to predict fatigue life in reality. Meanwhile, fatigue data obtained by laboratory tests can be rather expensive. For example, a high-cycle ($10^6$ cycles) fatigue test with traditional facilities requires approximately three months experimental time. Due to the high cost and limit of test approaches, multiple fatigue data up to the high-cycle regime is less available. Therefore, fatigue behaviour beyond this number is still under investigation. Numerical simulations which have contrasty faster speed than the real-time test, are helpful to analyse fatigue behaviours. Because the loading condition of engineering structures is very complex or even random, a generalised modelling approach focusing on the simulation of fatigue randomness with low computational cost and good adaptivity to diverse structure and loading conditions is desired.

## 1.2 Literature overview

In literature, there are mainly two subdivisions in the field of deterministic fatigue modelling: the non-progressive (empirical) approach which relies on a large amount of S-N data [3, 4]; the CDM based progressive approach that studies the detailed material behaviour during the fatigue process [5, 6]. The empirical model often provides a simple algebraic S-N relation based on regression analysis of experimental data. However, its application on the multi-axial problem can be rather difficult [7]. Though the progressive approach is computationally expensive, it can capture the evolution of material state by temporal discretisation. The sophisticated coupling with complex loading conditions and other physics can be simulated [8]. For rate-dependent CDM models [9], the damage increment has to be evaluated on fine-discretised time steps. Its long-term evolution, e.g. the high-cycle fatigue computation, can be numerically challenging. To reduce the computational cost, several strategies are proposed in the literatures, such as jumping-cycle methods [10, 11], the multi-temporal scale approach [12] and the model order reduction method [13, 14].

The modelling of fatigue uncertainties is, however, still under development. An overview of the existing modelling approaches is presented in fig. 1.2. Empirical models are introduced using Weibull distribution to describe the statistical behaviour of fatigue scatters [15, 16, 17]. Recently, the frequency and mean-stress effects on fatigue uncertainties are considered by the literature [18, 19, 20, 21]. However, the algebraic expression becomes complex, with many model parameters having

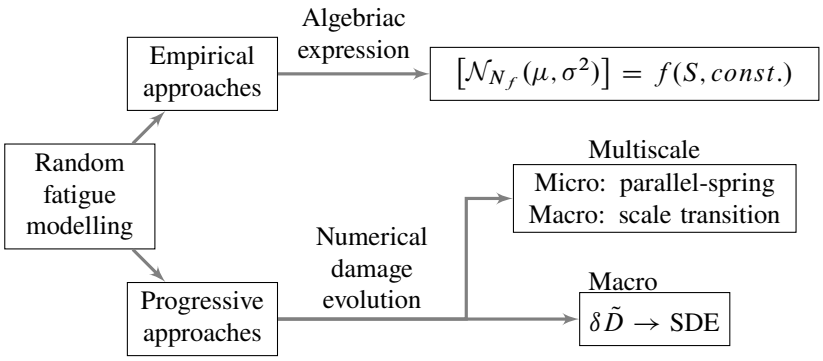


Figure 1.2: Overview of modelling approaches for random fatigue

no clear definition in classical mechanics. The lack of adaptivity barriers the application of these empirical models. Besides the study [22] from the fracture mechanics, damage mechanics based stochastic progressive approaches can be divided into two branches, i.e. the phenomenological approach [23, 24, 25] and the micromechanics involved multi-scale methods [26, 27, 28, 29, 30]. In contrast, multi-scale models use the parallel-spring model and its variants with uncertain failure criteria to describe the uncertain damage evolution at the micro-scale. These approaches have two common weaknesses. First, the micro-damage evolution is almost identical to the cumulative distribution function. Despite the spatial correlation [27] and sophisticated micro-elements [28, 29, 30] are introduced, the microstructural heterogeneity is still barely interpreted. Second, to propose a proper transition between different scales, one relies on empirical functions. The idea of modifying irreversible macroscopic damage evolution as a stochastic process is commonly taken by phenomenological approaches. The key step is to represent the deterministic damage evolution rate by a stochastic differential equation. Regardless of the drift term, the main difference of these works is on the treatment of stochastic diffusion, where both proportional [23] and non-proportional [24] diffusion are proposed. In the work [23] the deterministic Lemaitre damage law is directly adopted by the modelling procedure, with the noise intensity suggested being proportional to the current damage value. The advantage is that the original definition of the thermodynamic and dissipative potentials in the CDM are maintained. The stochastic material macroscopic behaviour can be obtained by the constitutive relations. However, this work provides only a general framework, and the model applicability is not verified by numerical studies. In the works [31, 24], the damage evolution rate is proposed as a stochastic Langevin equation using the Gaussian white noise. The main goal is to investigate different approaches to solve the damage SDE. The indirect solution corresponds to solving the equivalent Fokker-Plank equation and the direct solution is obtained using the 1.5 order implicit scheme. However, in this study less attention is paid to the damage evolution. The deterministic damage law is represented by an arbitrary third-order polynomial function, and the damage evolution path is piece-wisely unreal due to negative increments. Another study [25] assumes the initial damage state is random, and a zero-mean Markov process is added to the deterministic Helmholtz free energy. The proposed stochastic damage evolution law contains unique parameters and quantities that cannot benefit from deterministic studies. The common weakness of the studies listed above is that the finite element solution of the proposed random damage law is generally missing.

## 1.3 Objective

The main goal of this study is to apply the stochastic damage evolution law on structural fatigue problems solved by the finite element method. The reproduced virtual fatigue scatter is desired to confirm with the experimental data statistically. With the help of modern computers, the simulation procedure shall be finished in a reasonable time, providing a highly accurate probabilistic description on the S-N diagram. This study follows the the phenomenological approach, such that the damage evolution is simulated as a stochastic diffusive process. The drift term, which controls the mean of the stochastic process, is assumed identical to the deterministic quasi-brittle damage law. The stochastic diffusion, which determines the intensity of random noise, shall be carefully configured. The challenge is to maintain the thermodynamic consistency while modelling the damage process. This includes calibrating the random numbers to represent accurate experimental results, developing efficient numerical schemes for high-cycle fatigue computation and generating sufficient Monte-Carlo realisations.

This thesis is arranged by following chapters: In chapter 2, a brief introduction of the stochastic process and the evaluation schemes is given. In chapter 3, the background of continuum damage mechanics is reviewed. In chapter 4, a detailed literature survey is presented to compare the determinist and stochastic modelling approaches of concrete damage behaviour. In chapter 5, a systemic review on fatigue theories and simulation techniques is given. In chapter 6, the innovative modelling approach of stochastic damage law is exposed, with investigations on the model parameter. A in-depth discussion of the numerical scheme is given in chapter 7. Finally, in chapter 8 the finite element simulation of the four-point flexural fatigue problem is presented.

# Chapter 2

# Stochastic Processes

Stochastic processes are classically used to simulate the random movement of particles, i.e. the Brownian motion. Applications based on its remarkable statistical property are now extended to interdisciplinary fields such as modelling of infectious diseases, quantitative financial analysis, etc. This chapter provides a brief review of the stochastic process regarding to its mathematical interpretation and numerical simulation method. For a comprehensive explanation of the theories, one can refer to the following books [32, 33].

## 2.1 Probability and Stochastic Processes

Consider a probabilistic space $(\Omega, \mathcal{A}, P)$, where $\Omega$ denotes the sample space, $\mathcal{A}$ is a set of events, $P$ is the probability measure function. For the time interval $T \in [0, \infty)$, a stochastic process $X$ is a collection of time-dependent random variables denoted as

$$X = \{X(t, \omega), t \in T, \omega \in \Omega\}. \tag{2.1}$$

Mathematically, it is a mapping defined as $X : T \times \Omega \to \mathcal{S}$, where $\mathcal{S}$ is a measurable real number space. For each $t \in T$, $X(t, \cdot)$ is a random variable, and for each $\omega \in \Omega$, $X(\cdot, \omega)$ is a realisation or a sample path of the stochastic process. $X(t, \omega)$ is often simplified as $X(t)$ under the condition of having static $\Omega$. To evaluate the stochastic moments of $X(t)$, operators for the statistical mean $\mathbb{E}(\cdot)$ and variance $\mathbb{V}(\cdot)$ are needed. The statistical property of $X(t)$ at different time can be described by the covariance as

$$\mathrm{Cov}\left[X(t,s)\right] = \mathbb{E}\Big(\big[X(t) - \mathbb{E}\big(X(t)\big)\big] \cdot \big[X(s) - \mathbb{E}\big(X(s)\big)\big]\Big), \tag{2.2}$$

in which $t, s$ are two different time instances in $T$. The normalised covariance known as the correlation is given by

$$\mathrm{Cor}\left[(t,s)\right] = \frac{\mathrm{Cov}(t,s)}{\sqrt{\mathbb{V}(X(t))}\sqrt{\mathbb{V}(X(s))}}. \tag{2.3}$$

### 2.1.1 Classification of Stochastic Process

Stochastic processes can be classified from many different perspectives. By analysing the stochastic dependency to the random number, the stationariness of a stochastic process $X(t)$ is determined by

the probabilistic distribution during a specified time interval. $X(t)$ is strictly stationary, if for any time subset $\{t_1, t_2, \cdots, t_n\}$ of $T$ and for any arbitrary time increment $\delta t$, the following two joint cumulative distribution functions

$$F_{t_1,t_2,\cdots,t_n}(x_1, x_2, \cdots, x_n) := P\{X(t_1) < x_1, X(t_2) < x_2, \cdots, X(t_n) < x_n\} \tag{2.4}$$

and

$$F_{t_1+\delta t,t_2+\delta t,\cdots,t_n+\delta t}(x_1, x_2, \cdots, x_n) := P\{X(t_1+\delta t) < x_1, X(t_2+\delta t) < x_2, \cdots, X(t_n+\delta t) < x_n\} \tag{2.5}$$

equal to each other. In another word, the probabilistic distribution of a strictly stationary process has to be fully identical for all $t \in T$. In contrast, the weakly stationary requires fixed stochastic moments in terms of mean and variance. In this case, the covariance of multiple variables relates to the time difference, namely

$$\begin{cases} \mathbb{E}(X(t)) = const. \\ \mathbb{V}(X(t)) = f(0) = const. \\ \mathrm{Cov}(t,s) = f(s-t) \end{cases}, \tag{2.6}$$

where $f$ is a finite function that can be evaluated for all $t, s \in T$. For unspecified random distributions, the strictly stationary process is a subset of the weakly stationary process.

By analysing the conditional probability between the random numbers at different time, a stochastic process is a Markov process if the following relation holds,

$$P\left(X(t_{n+1})\middle|X(t_n)\right) = P\left(X(t_{n+1})\middle|X(t_1), X(t_2), \ldots, X(t_n)\right) \text{ with } \{t_1, t_2 \ldots t_n\} \in T. \tag{2.7}$$

In other words, a process is Markovian, if its current state only depends on its state at the last reference time. Stochastic processes with Markov property are widely implemented to simulate memoryless physical phenomenons including randomness, e.g. the motion of a molecule.

### 2.1.2 Gaussian and Wiener Process

Gaussian process is a specific class of stochastic process in which the random variable follows Gaussian distribution for all the time instances. A stochastic process $X(t, \omega)$ is a Gaussian process, if it satisfies the necessary and sufficient condition, that the finite linear combination $Z$ in the form,

$$Z(\omega) = \sum_{i=1}^{n} \alpha_i X(t_i, \omega), \ \forall \alpha_i \in \mathbb{R}, \ \forall t_i \in T, \tag{2.8}$$

is Gaussian. It means $X(t_i)$ has to be Gaussian for all $t_i \in T$. The standard Wiener process $W(t)$ is a specified Gaussian process having the Markov property. Given an initial value $W(t_0) = 0$, a constant zero mean $\mathbb{E}\big(W(t)\big)$ is kept for all the time. Its variance increases by time, namely $\mathbb{V}\big(W(t)\big) = \tau$, where $\tau$ is the nondimensionalized counterpart of $t$. The covariance of a Wiener process at two different time steps $s$ and $t$ is given by

$$\mathrm{Cov}\big(W(s), W(t)\big) = \min(s, t). \tag{2.9}$$

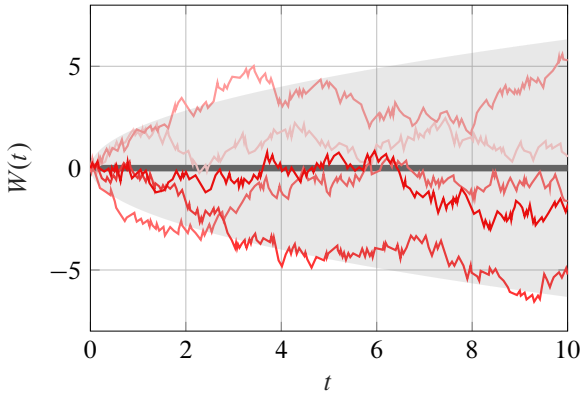


Figure 2.1: A demonstration of several Wiener process realisations with the mean marked by a bold line and 95% confident region filled by light grey colour

For any $\delta t$, the Wiener increment $\delta W := W(t + \delta t) - W(t)$ follows Gaussian, as the mean $\mathbb{E}(\delta W) = 0$ and the variance $\mathbb{V}(\delta W) = \delta\tau$. Therefore, for $\{t_1, t_2 \dots t_n\} \in T$ the increment $\{W(t_2) - W(t_1), W(t_3) - W(t_2), \dots, W(t_n) - W(t_{n-1})\}$ are independent from each other, which yields to the Markovian criteria. The Wiener process sampled at any arbitrary time $t_n$ can be given by the accumulation form

$$W(t_n) = \sum_{i=1}^{n} \delta W_i = \sum_{i=1}^{n} \big[W(t_i) - W(t_{i-1})\big]. \tag{2.10}$$

As an example, several realisations of Wiener process in the period of $t \in [0, 10]$ s are shown in fig. 2.1. The 95% confidence interval increases sub-linearly along the time, while the mean is expected to be zero. The probabilities that $W(t)$ is evaluated with positive and negative values are theoretically equal. Therefore, a single trajectory can cross the mean without limitation, neither the crossing time nor the number of total occurrences. It also means, $W(t)$ is not a monotonic function. Due to the random increment, $W(t)$ is nowhere differentiable. The classical Monte-Carlo (MC) method needs many Wiener realisations to reproduce accurate statistical mean and variance.

## 2.2 Stochastic Calculus

Stochastic differential equations, in short form SDEs, have been originally introduced by Langevin to describe the motion of small particles in differential forms. The velocity $X(t)$ of the particle is assumed to have perturbations, and the acceleration is derived as an ordinary differential equation (ODE), known as the Langevin function,

$$\frac{dX}{dt} = g(t, X) + h(t, X)\, \xi_t^{\mathrm{N}}, \tag{2.11}$$

where $g(t, X)$ represents a speed-dependent frictional force and $h(t, X)\, \xi_t^{\mathrm{N}}$ is the random molecular force with $\xi_t^{\mathrm{N}}$ representing the standard Gaussian white noise and $h$ controlling the intensity of the noise. By separating the time, eq. (2.11) can be rewritten as

$$dX = g(t, X)\, dt + h(t, X)\, dW_t, \tag{2.12}$$

where $dW_t$ is the infinitesimal Wiener increment at $t$. A stochastic integral can be applied on the two sides of eq. (2.12), namely

$$X(t) = X(t_0) + \int_{t_0}^{t} g(s, X(s))\, ds + \int_{t_0}^{t} h(s, X(s))\, dW_s, \tag{2.13}$$

in which the first integral follows the classical Riemann rule,

$$\int_{t_0}^{t} g(s, X) ds = \lim_{n\to\infty} \sum_{i=1}^{n} g(t_i, X_i)\Delta t_i, \tag{2.14}$$

whereas the second one is calculated via the Ito integral as,

$$\int_{t_0}^{t} h(s, X) dW_s = \lim_{n\to\infty} \sum_{i=1}^{n} h(t_i, X_i)(W_i - W_{i-1}). \tag{2.15}$$

Using another notation $\circ\, dW_t$, the stochastic integral can be represented in the Stratonovich form, namely

$$\int_{t_0}^{t} h(t, X) \circ dW_s = \lim_{n\to\infty} \sum_{i=1}^{n} \frac{h(t_i, X_i) + h(t_{i-1}, X_{i-1})}{2}(W_i - W_{i-1}). \tag{2.16}$$

Although both approaches are mathematically correct, there are many discussions regarding the application of the Ito and Stratonovich integral in different situations. In general, Ito calculus is mainly used in mathematical finance, where the SDE represents a continuous time limit of a discrete-time problem [34]. The Stratonovich form is consistent with the Riemann integral and the classical calculus chain rule. For both method, the guideline is to have smooth perturbations while modelling physical processes because the intensity of the white noise has to be very small [32].

**Ito and Stratonovich integral** The fundamental difference between the two approaches is on the integration point. Ito evaluates the diffusion at the last time step $t_{i-1}$ instead the current one $t_i$. On the stochastic integral problem of $\int_0^t W_t dW_t$ the Ito setting causes a time-unsymmetrical integral as

$$\begin{aligned}
\int_{t_0}^{t} W_t dW_t &= \lim_{t\to\infty} \sum_{i=1}^{n} W_{i-1}(W_i - W_{i-1}) \\
&= \frac{1}{2} \lim_{t\to\infty} \left( \sum_{i=1}^{n} (W_i^2 - W_{i-1}^2) - \sum_{i=1}^{n} (W_i - W_{i-1})^2 \right) \\
&= \frac{W_t^2 - W_{t_0}^2}{2} - \frac{\tau - \tau_0}{2}.
\end{aligned} \tag{2.17}$$

Stratonovich approach is similar to the trapezoidal rule such that the integral is on the averaged function value at two time steps, e.g.

$$\int_{t_0}^{t} W_t \circ dW_t = \lim_{t\to\infty} \sum_{i=1}^{n} \frac{W_i + W_{i-1}}{2}(W_i - W_{i-1}) = \frac{W_t^2 - W_{t_0}^2}{2}. \tag{2.18}$$

Unlike eq. (2.17) the solution given by eq. (2.18) is time-symmetric and identical to the classical Riemann solution. However, the Ito integral cannot be judged as a worse approach, since the consistency between stochastic and the Riemann integral is not required. To support this opinion $W_t$ is neither a smooth nor a differentiable function. After a simple mathematical transformation on the drift term, Ito and Stratonovich integrals are equivalent to each other, namely

$$\begin{aligned} dX &= g(t,X)\,dt + h(t,X)\,dW_t \\ &= \left(g(t,X) - \frac{1}{2}\frac{\partial h}{\partial X}h(t,X)\right)\,dt + h(t,X)\circ\,dW_t. \end{aligned} \tag{2.19}$$

Usually, the drift can be determined by the physical laws. Ito integral allows the stochastic model to be formulated straightforwardly by directly substituting the known information into the drift term. The expectation of the SDE can be kept identical to the deterministic solution without modifying the diffusion term [23, 22]. In the following chapter, the stochastic process is computed by the Ito integral to simulate random damage evolution.

## 2.3 Numerical Approximation of SDEs

Depending on the expression of the drift and diffusion, some SDEs are algebraically solvable. However, the drift and diffusion terms can be strongly non-linear in the reality that the model can only be solved numerically. In the following context, numerical techniques for solving SDEs are listed, including discussions on the convergence performance, stability issues, and the influence of the random number generator.

### 2.3.1 Numerical Schemes

The Euler method and its variations are effective in solving ordinary differential equations. The Euler-Maruyama method is specified for linear approximation of SDE problems. Consider the eq. (2.12) with initial value $X(0) = X_0$ as an example. The standard (or explicit) Euler-Maruyama scheme is given by

$$X_{i+1} = X_i + g(t_i, X_i)\Delta t_{i+1} + h(t_i, X_i)\Delta W_{i+1}, \tag{2.20}$$

with

$$\begin{cases} \Delta t_{i+1} = t_{i+1} - t_i, \\ \Delta W_{i+1} = W(t_{i+1}) - W(t_i). \end{cases} \tag{2.21}$$

To improve the accuracy an implicit scheme evaluating $g$ and $h$ on $t_{i+1}$ is written by

$$X_{i+1} = X_i + g(t_{i+1}, X_{i+1})\Delta t_{i+1} + h(t_{i+1}, X_{i+1})\Delta W_{i+1}. \tag{2.22}$$

According to the definition of the Wiener process, each $\Delta W_i$ is a random variable obtained as

$$\Delta W_i = \xi_i \sqrt{\Delta t_i}. \tag{2.23}$$

Based on the Taylor expansion, the Milstein method takes the diffusion ratio to achieve a higher convergence speed. The standard explicit scheme is written as

$$\begin{aligned} X_{i+1} &= X_i + g(t_i, X_i)\Delta t_{i+1} + h(t_i, X_i)\Delta W_{i+1} \\ &\quad + \frac{1}{2}h(t_i, X_i)\frac{\partial h}{\partial X_i}(\Delta W_{i+1}^2 - \Delta\tau_{i+1}). \end{aligned} \tag{2.24}$$

The Milstein method delivers the same performance as the the explicit Euler-Maruyama if $h$ is independent of $X$. The strong error[1] convergence rate is order 0.5 for the explicit Euler-Maruyama and order 1 for the Milstein method. Other high-order approaches such as the strong order 1.5 Taylor method proposed by Kloeden and Platen [35] is implemented by Silberschmidt [24] on dynamic mechanical problems in which $X$ denotes the stochastic damage evolution. The scheme reads

$$\begin{aligned} X_{i+1} &= X_i + g\Delta t_{i+1} + h\Delta W_{i+1} + \frac{1}{2}h\frac{\partial h}{\partial X_i}(\Delta W_{i+1}^2 - \Delta\tau_{i+1}) \\ &\quad + \frac{\partial g}{\partial X_i}h\Delta Z_i + \frac{1}{2}\left(g\frac{\partial g}{\partial X_i} + \frac{1}{2}h^2\frac{\partial^2 g}{\partial X_i^2}\right)\Delta t_{i+1}^2 \\ &\quad + \left(g\frac{\partial h}{\partial X_i} + \frac{1}{2}h^2\frac{\partial^2 h}{\partial X_i^2}\right)(\Delta W_{i+1}\Delta t_{i+1} - \Delta Z_{i+1}) \\ &\quad + \frac{1}{2}h\left(h\frac{\partial^2 h}{\partial X_i^2} + \left(\frac{\partial h}{\partial X_i}\right)^2\right)\left(\frac{1}{3}\Delta W_{i+1}^2 - \Delta\tau_{i+1}\right)\Delta W_{i+1}, \end{aligned} \tag{2.25}$$

in which $\Delta Z_{i+1}$ is an additional random variable,

$$\Delta Z_i = \frac{1}{2}\Delta t_i(\Delta W_i + \Delta\hat{W}_i/\sqrt{3}), \tag{2.26}$$

with $\hat{W}_i = \xi_i\sqrt{\Delta t_i}$ generated independently from $\Delta W_i$. If the diffusion and drift term are strongly non-linear functions of $X$ the scheme above converges faster than the Milstein method. For better accuracy, a Runge-Kutta based approach is implemented by Kloeden and Platen [36] in which a function system have to be evaluated within each time iteration. Details about the high-order numerical schemes for SDEs can be found in [32].

### 2.3.2 Strong and Weak Convergence

The numerical error of the SDE solution can be defined mathematically in terms of the strong and weak errors. Let $X_t$ be the numerical solution of an SDE at time $t$. If the corresponding analytical solution $X(t)$ exists, the strong error is given by the expression

$$e^{\mathrm{st}} = \mathbb{E}\left|X_t - X(t)\right|, \tag{2.27}$$

where $|\cdot|$ denotes the $L_1$ norm. Since both $X_t$ and $X(t)$ are random variables, a statistical mean is needed to measure the mean of the absolute error. On the contrary, the weak error is defined as the error of mean, namely

$$e^{\mathrm{wk}} = \mathbb{E}\left|X_t\right| - \mathbb{E}\left|X(t)\right|. \tag{2.28}$$

[1] see section 2.3.2

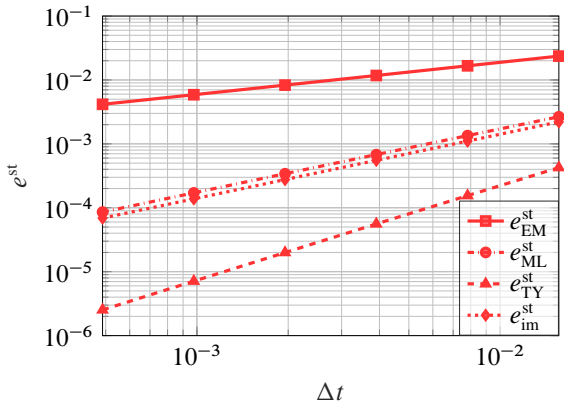


Figure 2.2: Strong error convergence performance of several numerical schemes (EM: standard Euler-Maruyama, ML: Milstein, TY: Taylor, im: implicit EM)

Theoretically, both errors approach zero when the time step is infinitely small. Indeed, the error converges in the order of $p$, if a constant $C$ exists such that

$$\varepsilon \leq C\Delta t^{p}. \tag{2.29}$$

Often, the strong and weak convergence rates delivered by a numerical scheme are different.

**Example** In order to compare the methods listed in section 2.3.1, an exactly solvable SDE with initial value $X(0) = 0$ is introduced in the form

$$dX = -\sin(X)\cos^3(X)dt + \cos^2(X)dW_t. \tag{2.30}$$

The analytical solution of the above SDE reads

$$X(t) = \arctan\big(W_t + \tan(X(0))\big). \tag{2.31}$$

The time interval $[0, 1]$ is discretised by different time step size and the numerical errors are evaluated at $t = 1$. For every single trajectory, each method uses the same Wiener process realisation $W_t$. A total of $10^6$ realisations are generated to reduce the sampling error. A comparison of the performance of the listed numerical methods on the strong error convergence is demonstrated in fig. 2.2.

For strongly non-linear diffusion and drift term in eq. (2.30), the accuracy is improved significantly while using the high-order schemes, and the effect becomes dramatic with small $\Delta t$. Particularly regarding the example problem, the strong convergence rates are assigned to Euler-Maruyama, Milstein, and Taylor method with order 0.5, 1, and 1.5 respectively. This observation corresponds to the literature [32]. Meanwhile, the implicit Euler-Maruyama method reaches a similar convergence speed and a slightly better accuracy than the standard Milstein method. The weak error convergence performance is illustrated in fig. 2.3 having noticeable difference compared to the results in fig. 2.2. Both the explicit Euler-Maruyama and the Milstein methods show an order 1 weak convergence rate, whereas the Taylor and the implicit Euler-Maruyama is order 2. Compared to the explicit Euler-Maruyama method, the accuracy of the implicit scheme is improved dramatically.

Although high-order schemes are numerically more accurate, the computational cost and the complexity of applying the high-order Taylor expansion are not negligible. The derivative computation can be rather expensive, especially when the explicit forms of the drift and diffusion

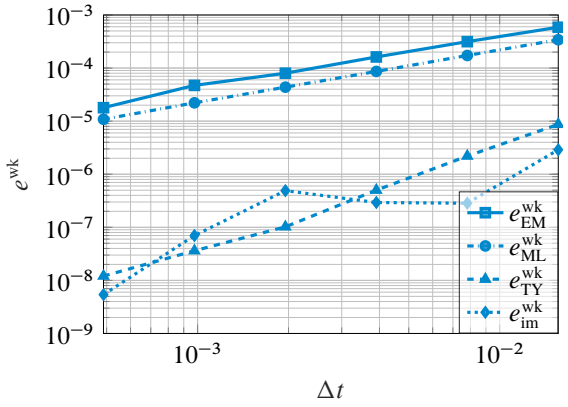


Figure 2.3: Convergence performance of numerical schemes on weak error (EM: standard Euler-Maruyama, ML: Milstein, TY: Taylor, im: implicit EM)

are not available. Indeed, the imprecision of numerical differentiation can be accumulated at every iteration step which finally enlarges the global error. Besides, high-order methods also rely on extra random numbers, e.g. the $\Delta Z_i$ term in eq. (2.26). It requires a large amount of preallocated computational resources for both the generation and the storage of random variables. Therefore, the implicit Euler-Maruyama method is a good solution, to have a balance between the computational effort and the convergence performance.

### 2.3.3 Stability Issues

Classically, stability issues of a deterministic ODE are classified into two categories, the system stability and numerical stability. Due to the random term, stability studies on SDEs are often complicated. For a stable system, its output shall fluctuates under control, if a small perturbation is introduced to the input. A quantitative definition is given by [32] that a stochastically stable sequence has to be bounded by a positive real number $\epsilon$, at any time after initiation, namely

$$P\left\{\sup_{t>t_0}|X(t)|<\epsilon\right\}=1. \tag{2.32}$$

If $X(t)$ approaches zero surely in a long time, it is an asymptotic stable sequence. The mathematical definition of the asymptotic stability is given by

$$P\left\{\lim_{t\to+\infty}|X(t)|=0\right\}=1. \tag{2.33}$$

In contrast, a stochastic sequence has the mean-square stability if

$$P\left\{\lim_{t\to+\infty}\mathbb{E}\left|X^2(t)\right|=0\right\}=1. \tag{2.34}$$

Numerical stability analysis on SDEs deals with a proper set of numerical parameters, particularly, numerical solutions under different time discretisation. The initial value problem while solving stiff ODEs is well known that explicit solvers with large time steps have difficulties to converge to the real solution. Implicit schemes are designed to improve the convergence performance, which is less sensitive to the time step size. However, the classical approach to

analyse the numerical stability of SDE solvers has limitations. For demonstration, assume the one-step iteration is obtained by a numerical scheme,

$$X_{i+1} = f(\Delta t, \Delta W_i, \cdots)X_i, \tag{2.35}$$

in which the dots denote the other variables. It is numerically stable if the following deterministic expression exist, i.e.

$$|f(\Delta t, \Delta W_t, \cdots)| < 1. \tag{2.36}$$

Because of the random part, only the probability of the above relationship can be obtained, namely

$$P\left\{|f(\Delta t, \Delta W_t, \cdots)| < 1\right\}. \tag{2.37}$$

Therefore, the numerical stability of an SDE solver in a deterministic sense is difficult to obtain. Meanwhile, stability study on problem similar to eq. (2.11) is often complicated if the function is non-linear and non-homogenous. In this case, the SDE may not be explicitly solvable using the classical linearisation method [37]. As an example, consider the non-linear SDE given by

$$\frac{dX}{dt} = f(X, t, \xi). \tag{2.38}$$

For any interesting value, $\hat{X}$, the Jacobian $\partial f(\hat{X})$ can vary significantly due to the strong randomness. Therefore, eigenvalues-based stability analysis loses its effectiveness in this case. Recently, attention has been drawn specifically to the stability study of non-linear SDEs, including jumps and delays, because of the high value of these random models in the stock market [38] and machine learning fields [39]. In the following context, the stability of linear SDEs and numerical stabilities are reviewed.

**Linear SDE stability** A linear SDE including two constants $\lambda$ and $\mu$ in the form

$$dX = \lambda X dt + \mu X dW_t, \tag{2.39}$$

with an explicit solution

$$X(t) = X(0)\exp\left[\left(\lambda - \frac{1}{2}\mu^2\right)t + \mu W_t\right], \tag{2.40}$$

is often a good examples to explain the stability theory [40, 41]. The explicit solution is asymptotically stable if

$$\mathrm{Re}\left\{\lambda - \frac{1}{2}\mu^2\right\} < 0, \tag{2.41}$$

while the mean square stability is satisfied by the following condition

$$\mathrm{Re}\left\{\lambda\right\} + \frac{1}{2}\mu^2 < 0, \tag{2.42}$$

where $\mathrm{Re}\left\{\cdot\right\}$ denotes the real part of a complex number. For this specified problem, any combination of parameters that ensures the mean squared stability automatically satisfies the asymptotic stability, because

$$\mathrm{Re}\left\{\lambda - \frac{1}{2}\mu^2\right\} < \mathrm{Re}\left\{\lambda\right\} + \frac{1}{2}\mu^2. \tag{2.43}$$

This conclusion can be proven graphically, as the mean square stability region is totally covered by the asymptotic one (see fig. 2.4).

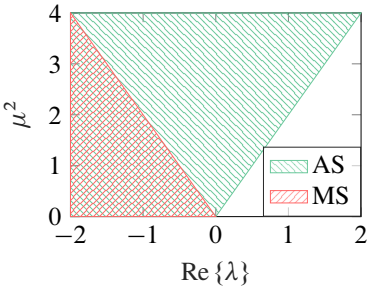


Figure 2.4: Comparison of stability regions using problem eq. (2.39) as the example (AS: asymptotic stability region, MS: mean square stability region)

**Numerical stability** According to the mathematical definition given by eqs. (2.33) and (2.34) the numerical asymptotic stability and mean-square stability are represented as

$$P\left\{\lim_{i\to+\infty}|X_i|=0\right\}=1, \tag{2.44}$$

and

$$P\left\{\lim_{i\to+\infty}\mathbb{E}\left|X_i^2\right|=0\right\}=1, \tag{2.45}$$

where $X(t)$ is replaced by the numerical solution $X_i$. Applying schemes listed in section 2.3.1 on eq. (2.39) the finite difference equations are obtained in form eq. (2.35). The explicit Euler-Maruyama scheme has the following iteration

$$X_{i+1}=(1+\Delta t\lambda+\mu\sqrt{\Delta t}\xi_i)X_i. \tag{2.46}$$

Taking the conclusion to the first and second stochastic momentum, i.e. $\mathbb{E}\,|\xi_i|=0$ and $\mathbb{E}\left|\xi_i^2\right|=1$, one has the expectation of the squared value as

$$E\left|X_{i+1}^2\right|=\left(|1+\Delta t\lambda|^2+\Delta t|\mu|^2\right)\mathbb{E}\left|X_i^2\right|. \tag{2.47}$$

In view of eq. (2.45) the numerical mean-square stability is guaranteed under the condition that

$$|1+\Delta t\lambda|^2+\Delta t|\mu|^2<1. \tag{2.48}$$

By replacing $\Delta t\lambda$ with $p$ and $|\mu|^2\Delta t$ with $q$, the mean-square stability region can be plotted as $(1+p)^2+q<1$. Let $V_i$ denote $1+\Delta t\lambda+\mu\sqrt{\Delta t}\xi_i$, eq. (2.46) is rewritten as a sequential product, namely

$$X_{i+1}=\left(\prod_{i=1}^{n}V_i\right)X_0. \tag{2.49}$$

For any $X_0\neq 0$ the logarithmic operation of the above equation gives

$$\log(|X_{i+1}|)=\sum_{i=0}^{n}\log(|V_i|)+\log(|X_0|). \tag{2.50}$$

Due to the non-bias approximation under a large amount of realisations, namely

$$\lim_{n\to\infty}\frac{\sum_{i=0}^{n}\log(|V_i|)}{n+1}-\mathbb{E}\log(|V_i|)=0, \tag{2.51}$$

the necessary and sufficient condition for asymptotic stability reads

$$\mathbb{E}\log(|V_i|) < 0. \tag{2.52}$$

However, as stated in the study [42] the derivation of a deterministic asymptotic stability function has considerable difficulties, since the integral

$$\int_{-\infty}^{+\infty} \log(|1 + p \pm \sqrt{q}x|)\frac{1}{\sqrt{2\pi}}e^{\frac{-x^2}{2}}dx = \mathbb{E}\log(|V_i|), \tag{2.53}$$

requires the Meijer G-function operation. By applying the second-order Taylor expansion at $|V_i|$ the following relationship yields

$$\mathbb{E}\log(|V_i|) \leq \log(\mathbb{E}|V_i|), \tag{2.54}$$

which indicates that $\mathbb{E}|V_i|<1$ is a sufficient condition for the numerical asymptotic stability. The integration

$$2\int_{0}^{+\infty} (1 + p \pm \sqrt{q}x)\frac{1}{\sqrt{2\pi}}e^{\frac{-x^2}{2}}dx = \mathbb{E}|V_i|, \tag{2.55}$$

provides a deterministic expression to ensure the asymptotic stability, namely

$$0 < 1 + p \pm \sqrt{\frac{2q}{\pi}} < 1. \tag{2.56}$$

Based on eqs. (2.48) and (2.56) the mean-square and asymptotic stability region of explicit Euler-Maruyama method is plotted in fig. 2.5. The mean-square stability region is smaller but not fully covered by the asymptotic stability region.

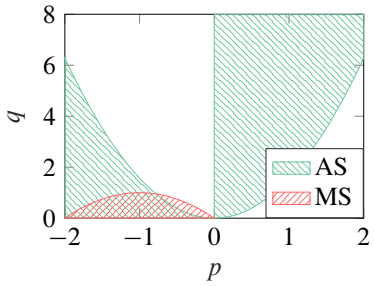


Figure 2.5: Numerical stability regions while applying the explicit Euler-Maruyama method on eq. (2.39)

The mean-square stability of the other numerical schemes listed in section 2.3.1 can be obtained as follows:

- implicit Euler-Maruyama:

$$\frac{1 + |\Delta t\mu^2|}{|1 - \Delta t\lambda|^2} < 1; \tag{2.57}$$

- Milstein method:

$$|1 + \Delta t\lambda|^2 + |\Delta t\mu^2| + \frac{1}{2}|\Delta t\mu^2|^2 < 1; \tag{2.58}$$

- Taylor scheme:

$$|1 + \Delta t\lambda|^2 + |1 + \Delta t\lambda|^2|\Delta t\mu^2| + \frac{1}{2}|\Delta t\mu^2|^2 + \frac{1}{6}|\Delta t\mu^2|^3 < 1. \tag{2.59}$$

According to the mean-square stability region illustrated in fig. 2.6, the implicit Euler-Maruyama scheme shows its advantage in stabilising the numerical solution. The asymptotic stability is not plotted here, since in most cases, mean-square stability is more strict. In conclusion, the stability issue has to be concerned while solving SDEs. It is always necessary to check the combination of the drift and diffusion with the time step size to avoid unrealistic results. Using implicit numerical schemes with a relatively small time step is more likely to reach a stable solution.

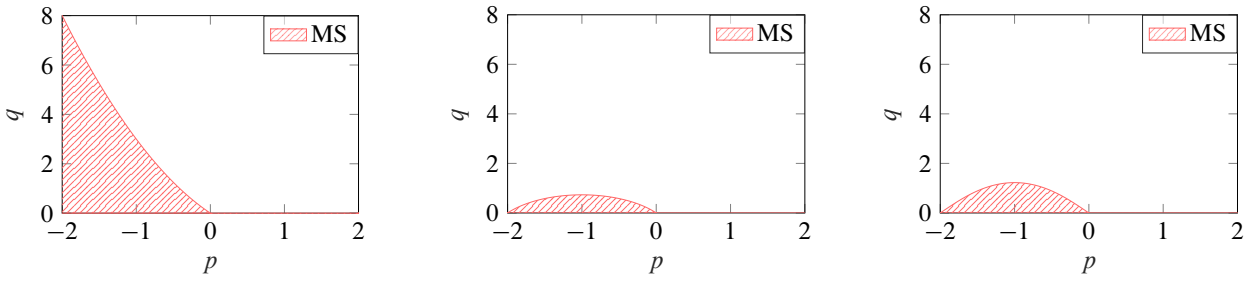


(a) implicit Euler-Maruyama (b) Milstein (c) Taylor

Figure 2.6: Comparison of mean-square stability of three numerical schemes on problem eq. (2.39)

### 2.3.4 Low-Discrepancy Sampling

In the previous context, the stochastic processes are realised by the MC simulation using pseudo-random numbers generated by the Mersenne-Twister (MT) algorithm. Although the random number generation is numerically very fast, the classical MC method is well-known for its low convergence rate in approximating the expectation. Depending on the sampling amount $N$ the quadrature error of classical MC sequence converges in the order of $\mathcal{O}(N^{-0.5})$ without dependence on the dimension. The quasi-random sequence improves the coverage in a $d$-dimensional hypercube to achieve a faster convergence rate in the order of $\mathcal{O}(N^{-1}(\log N)^{d-1})$ [43]. Therefore, much fewer random numbers are required while using the quasi-Monte-Carlo (QMC) to produce the same precision. As the method is designed for integration problem, the QMC is often very effective to accurately approximate the stochastic moments. However, its efficiency reduces when the dimension of the desired random number is very high [44]. In practice, the dimension is often limited by 150 [45].

Quasi-random sequences are deterministic in which the variables are correlated. Comparing to the pseudo-randomness, the uniformity of quasi-random number is quantitatively very low, named the low-discrepancy. The randomized-quasi-Monte-Carlo (RQMC) sequence is formed as an unbiased estimator by introducing randomness carefully to each QMC variable. Since RQMC points are rarely identical, the approximation error can be quantified while repeating the simulation. Compared to the classical MC method, RQMC is considered a variance reduction approach [44]. For the RQMC simulation, different approaches such as the Sobol and Halton scrambled sequences are frequently used. The characteristics of different random sequences in two dimensions are

illustrated in fig. 2.7. The grid is less equally filled by the MC points, whereas the QMC shows specific patterns due to the deterministic sequence. In contrast, the RQMC method improve the coverage with less "pattern-effect".

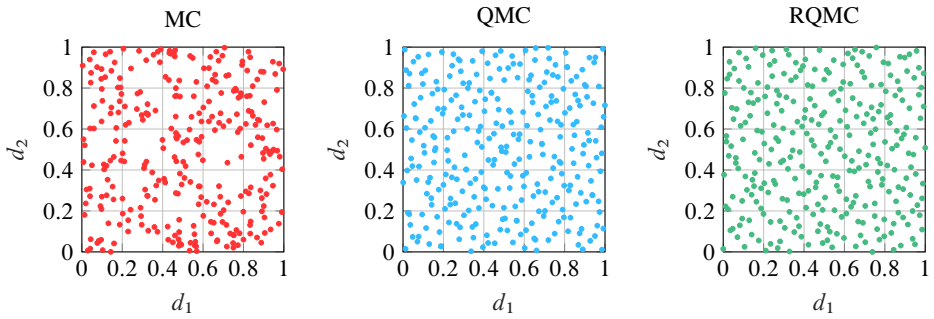


Figure 2.7: Comparison of two dimensional random number generated by MC, QMC using unscrambled Sobol, RQMC with scrambled Halton

Recently, RQMC methods implemented in financial engineering to generate stochastic process realisations. The studies [46, 47, 45] state that the main challenge is the limitation of the applicable dimension, a quantity governed by the number of time discretisation. For demonstration, MC and RQMC methods are tested on the generation of standard Wiener process. The simulation is conducted in the time interval $[0, 500]$s with $\Delta t = 1$s using $10^4$ trajectories repeated by $10^3$ times. Since $\mathbb{E}[W(t)]$ and $\mathbb{S}[W(t)]$ can be obtained explicitly, they are compared with their expectations during the interval (see fig. 2.8). Although for all the methods, their sampling errors are accumulated

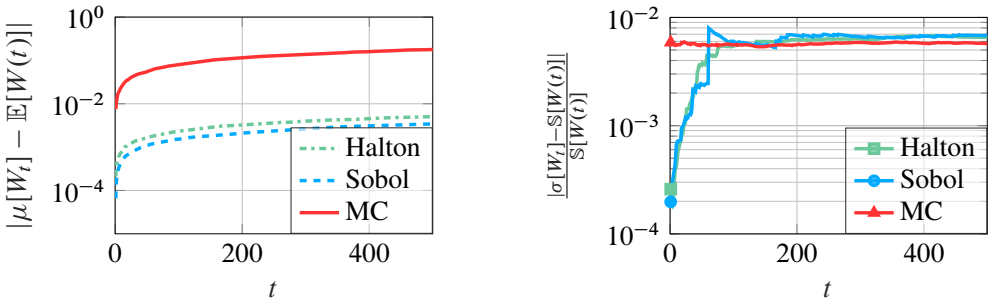


(a) absolute error of mean

(b) normalised absolute error of standard deviation

Figure 2.8: Comparison of MC and RQMC on the generation of Wiener process

by the time, approximately $10^2$ times less error in the statistical mean is achieved by the RQMC methods. Moreover, according to fig. 2.8a, the scrambled Halton sequence produces a slightly more accurate mean than the Sobol. In fig. 2.8b the MC sampling error in the standard deviation remains constant, whereas the RQMC produces roughly 15 times smaller error at the beginning. During the simulation, the error of RQMC increases and becomes less accurate than the MC after around 150 time steps. It demonstrates that the performance of RQMC methods in variance reduction is only valid for low-dimensional problems. This observation matches with the outcome from the previous study regarding the maximum practical dimension of the RQMC. In conclusion, particular attention

needs to be drawn while applying the RQMC to sample stochastic processes. First, it is effective to approximate the process expectation, though the dimension is high. Second, it is not suitable for long-term simulation in which the variance has to be accurately approximated.

Compared to the one-dimensional Wiener process, the complexity of numerical integration increases dramatically for real engineering applications. It is very challenging to develop robust low-discrepancy sequences with guaranteed variance reduction performance for high-dimensional integration problems. Although some recently developed methods, e.g. the Latin hypercube, show less restriction on the maximum number of dimensions, its efficiency is unsure for a small sampling amount [48, 49]. Due to simplicity and robustness, the classical MC is often the first choice for engineering simulation [50, 51, 52].

# Chapter 3

# Continuum Damage Mechanics

For an overview of the CDM theory, section 3.1 introduces the macroscopic observation and the microscopic mechanism of material damage. Section 3.2 describes the thermodynamics of damage process. Section 4.1.3 demonstrates the derivation of the kinetic damage evolution law. The theoretical background of CDM has been successively developed in the past few decades by the works [53, 54, 55]. For further information, the reader may refer to the literature [2, 56].

## 3.1 Fundamental Aspect of Damage

Material damage is often a mechanical phenomenon determined by the debonding of microscopic matter. Under external loading, material imperfections, such as the micro-cracks and voids, can be enlarged by the micro-stress. This process is often associated with a progressive reduction of the material stiffness, which finally triggers the global failure. For engineering materials, it is usually difficult to characterise the micro-discontinuities in detail. Therefore, for continuous media, a representative elementary volume (REV) at the mesoscale is introduced to average the heterogeneous material properties. Depending on the material microstructure, the REV size varies for metals ($\approx 0.1\text{mm}^3$) and plain concrete ($\approx 100\text{mm}^3$).

The concept of considering the damage as an effective surface density of micro-defects is established by Kachanov [53]. Various of microscopic defects and imperfections, e.g., nucleation, voids, cavities, are statistically averaged to a damage variable at a larger scale. On a plane defined by a point $P$ and a normal vector $\vec{n}$ within a given RVE, the isotropic damage variable $D$ is represented by

$$D = 1 - \frac{\tilde{A}}{A}, \tag{3.1}$$

where $A$ is the original cross-section area and $\tilde{A}$ is after removing the defects using effective configuration. For a uniaxial load with a magnitude of $F$, the uniaxial stress $\sigma$ is evaluated as

$$\sigma = \frac{F}{A}, \tag{3.2}$$

for undamaged material. The effective stress $\tilde{\sigma}$ is introduced then using an isotropic damage variable, namely

$$\tilde{\sigma} = \frac{\sigma}{1 - D}. \tag{3.3}$$

Generalised to the multi-axial case, the effective stress tensor $\tilde{\boldsymbol{\sigma}}$ is derived by

$$\tilde{\boldsymbol{\sigma}} = \mathbb{M} : \boldsymbol{\sigma}, \tag{3.4}$$

where $\boldsymbol{\sigma}$ is the stress tensor, and $\mathbb{M}$ is the fourth-order damage effect tensor [2].

**Strain equivalence principle** The principle of strain equivalence is introduced to share the same derivation of the constitutive law for virgin and damaged material given by

$$\begin{cases} \boldsymbol{\varepsilon}_e = \mathcal{F}(\boldsymbol{\sigma}, \cdots) = \mathbb{C}^{-1}\boldsymbol{\sigma} & \text{virgin material,} \\ \boldsymbol{\varepsilon}_e = \mathcal{F}(\tilde{\boldsymbol{\sigma}}, \cdots) = \tilde{\mathbb{C}}^{-1}\tilde{\boldsymbol{\sigma}} & \text{damaged material,} \end{cases} \tag{3.5}$$

where $\mathbb{C}$ and $\tilde{\mathbb{C}}$ denote the fourth-order elasticity tensor before and after damage, $\boldsymbol{\varepsilon}_e$ is the equivalent strain. By applying the principle of strain equivalence, the elasticity modulus of the damaged material $\tilde{E}$ can be derived from the original elastic modulus $E$ as

$$\tilde{E} = E(1 - D). \tag{3.6}$$

The relationship between the damaged and undamaged elasticity tensor is given by

$$\tilde{\mathbb{C}} = (\mathbb{I} - \mathbb{D})\mathbb{C} = \mathbb{M}^{-1}\mathbb{C}, \tag{3.7}$$

where $\mathbb{D}$ and $\mathbb{I}$ represent the damage tensor and identity matrix both in fourth-order.

**Critical damage value** In the context of material continuity, failure happens when the REV overrides its countability of being a continuum volume [54]. Indeed, macroscopic defects occur when the damage variable is over $D_c$. After this point, the propagation of macroscopic defects causes material instability. Due to the interpretation of $D_c$, CDM becomes particularly suitable for studying the material behaviour during the initiation of macroscopic cracks.

Generally, the value of $D_c$ varies from 0.15 to 0.85 depending on different materials and loading conditions. For monotonic load, $D_c \approx 0$ and $D_c \approx 1$ correspond to purely brittle and ductile fracture, respectively. For ductile material, $D_c$ is often obtained as a damage value associated with rupture and necking in the case of a monotonic test [57, 25]. Whereas for fatigue test, $D_c$ is related to the initiation of macroscopic cracks [58, 59].

## 3.2 Thermodynamics of Damaged Material

Material damage is an irreversible thermodynamic process associated with energy dissipation. This concept is one of the core theory of CDM, which has been successfully implemented in the works [58, 60, 2]. Based on thermodynamic principles, the state potential of a material can be written as a function in which the relationship between state variables is performed. Through the derivation of this function, an energy-based damage criterion can be obtained. According to the law of energy conservation, for a closed (isolated) system, the applied external work $W$ and the received heat $Q$ is transformed into the internal energy $U$ and the kinetic energy $K_e$, namely

$$\dot{U} + \dot{K}_e = \dot{W} + \dot{Q}, \tag{3.8}$$

where ( $\dot{}$ ) denotes the time derivative of each quantity. The Helmholtz free energy $\Psi$, which measures the effective work obtained by a closed thermodynamic system, is given by

$$\Psi = U - TS, \tag{3.9}$$

where $T$ is the absolution temperature, $S$ is the system entropy. Comparing with the Clausius-Duhem inequality, i.e.

$$\dot{S} - \frac{\dot{Q}}{T} \geq 0, \tag{3.10}$$

a relationship can be obtained as follows

$$\delta\Psi \leq \delta W - \delta K_e. \tag{3.11}$$

It means the maximum energy to be released from the system is bounded by the applied work. The state of a thermodynamic system is described by a set of macroscopic variables. Consider the Helmholtz free energy as a continuous scalar function, which is concave for $T$ and convex for $\mathbf{X}$, namely

$$\Psi = \Psi(\mathbf{X}, T), \tag{3.12}$$

where $\mathbf{X}$ denote all the remaining state variables of the system excluded from temperature. Following the chain rule, the time derivative of $\Psi$ can be written as

$$\dot{\Psi} = \frac{\partial\Psi}{\partial\mathbf{X}}\dot{\mathbf{X}} + \frac{\partial\Psi}{\partial T}\dot{T}. \tag{3.13}$$

Combined with the inequality given by eq. (3.10), the dissipation rate $\Phi$ is defined as

$$\Phi := \dot{W} - \dot{K}_e - \frac{\partial\Psi}{\partial\mathbf{X}}\dot{\mathbf{X}} - \left(\frac{\partial\Psi}{\partial T} + S\right)\dot{T} \geq 0. \tag{3.14}$$

By the hypothesis of constant temperature eq. (3.14) yields to

$$\Phi = \dot{W} - \dot{K}_e - \frac{\partial\Psi}{\partial\mathbf{X}}\dot{\mathbf{X}} \geq 0. \tag{3.15}$$

The thermodynamic process is reversible if the condition $\Phi = 0$ can be satisfied. For example, the frictionless rigid body kinetic motion, with which the external work is converted into the kinetic energy without any loss, i.e. $\dot{\mathbf{X}} = \mathbf{0}$.

**Constitutive relations** The thermodynamic constraints demonstrated above are generalised for any closed system. To study the mechanical behaviour of material damage, constitutive equations that adhere to the thermodynamic principles have to be introduced at the REV level. Specifying the general closed system to be a continuum deformable body $\mathcal{B}$ with surface $\partial\mathcal{B}$, the internal energy $U$ and the kinetic energy $K$ can be computed by the integral on the unit volume $dV$ as

$$\dot{U} = \int_{\mathcal{B}} \rho\,\dot{e}\,dV, \tag{3.16}$$

and

$$\dot{K} = \int_{\mathcal{B}} \rho \, \boldsymbol{v} \cdot \dot{\boldsymbol{v}} \, dV, \tag{3.17}$$

where $\rho$, $e$ and $\boldsymbol{v}$ denote the mass density, specific energy and the velocity, respectively. The applied external mechanical power can be separated into two parts, which are the body force $\boldsymbol{f}$ on the unit mass $\rho \, dV$ and the surface traction $\boldsymbol{t}$ on the unit area $dS$, given by

$$\dot{W} = \int_{\mathcal{B}} \rho \, \boldsymbol{f} \cdot \boldsymbol{v} \, dV + \int_{\partial\mathcal{B}} \boldsymbol{t} \cdot \boldsymbol{v} \, dS. \tag{3.18}$$

The rate of received heat to the body is defined as

$$\dot{Q} = \int_{\mathcal{B}} r \, dV - \int_{\partial\mathcal{B}} \boldsymbol{q} \cdot \boldsymbol{n} \, dS, \tag{3.19}$$

where $r$ denotes the heat generation rate per unit volume, $\boldsymbol{q}$ and $\boldsymbol{n}$ are the heat flux and unit normal vector towards outside of the surface. The energy convention for a deformable body can be obtained by substituting eqs. (3.16) to (3.19) into eq. (3.8) as

$$\begin{aligned} \int_{\mathcal{B}} \rho \, (\dot{e} + \boldsymbol{v} \cdot \dot{\boldsymbol{v}}) \, dV &= \int_{\mathcal{B}} (\rho \, \boldsymbol{f} \cdot \boldsymbol{v} + r) \, dV + \int_{\partial\mathcal{B}} (\boldsymbol{t} \cdot \boldsymbol{v} - \boldsymbol{q} \cdot \boldsymbol{n}) \, dS, \\ &= \int_{\mathcal{B}} \rho \, \boldsymbol{f} \cdot \boldsymbol{v} + r + \operatorname{div} (\boldsymbol{\sigma} \boldsymbol{v} - \boldsymbol{q}) \, dV, \end{aligned} \tag{3.20}$$

which can be further derived as

$$\int_{\mathcal{B}} [(\rho \, \boldsymbol{f} + \operatorname{div}\boldsymbol{\sigma} - \rho \, \dot{\boldsymbol{v}}) \cdot \boldsymbol{v}] \, dV + \int_{\mathcal{B}} (\boldsymbol{\sigma} : \operatorname{grad}\boldsymbol{v} - \operatorname{div}\boldsymbol{q} + r - \rho \, \dot{e}) \, dV = 0. \tag{3.21}$$

By applying the Cauchy momentum equation,

$$\rho \, \boldsymbol{f} + \operatorname{div}\boldsymbol{\sigma} - \rho \, \dot{\boldsymbol{v}} = \boldsymbol{0}, \tag{3.22}$$

the first integral in eq. (3.21) can be cancelled, with which the function yields to

$$\int_{\mathcal{B}} (\boldsymbol{\sigma} : \operatorname{grad} \boldsymbol{v} - \operatorname{div} \boldsymbol{q} + r - \rho \, \dot{e}) \, dV = 0. \tag{3.23}$$

For small deformations, the equation above in the local form can be derived as

$$\rho \dot{e} = \boldsymbol{\sigma} : \dot{\boldsymbol{\varepsilon}} - \operatorname{div} \boldsymbol{q} + r, \tag{3.24}$$

using the strain rate $\dot{\boldsymbol{\varepsilon}}$. Let $s$ denote the specific entropy. The entropy of body $\mathcal{B}$ is obtained as

$$S = \int_{\mathcal{B}} \rho s \, dV. \tag{3.25}$$

According to eqs. (3.10) and (3.19) the Clausius-Duhem inequality is given by

$$\int_{\mathcal{B}} \rho \dot{s}\, dV - \int_{\mathcal{B}} \frac{r}{T}\, dV + \int_{\partial\mathcal{B}} \frac{\boldsymbol{q}\cdot\boldsymbol{n}}{T}\, dS \geq 0, \tag{3.26}$$

whereas its local form can be written as

$$\rho \dot{s} + \operatorname{div}\left(\frac{\boldsymbol{q}}{T}\right) - \frac{r}{T} \geq 0. \tag{3.27}$$

Combining eq. (3.27) with eq. (3.24), one has the energy dissipation rate as follows

$$\phi = \boldsymbol{\sigma} : \dot{\boldsymbol{\varepsilon}} - \rho(\dot{\psi} + s\dot{T}) - \boldsymbol{q} \cdot \frac{\operatorname{grad} T}{T} \geq 0, \tag{3.28}$$

where $\psi$ denotes the local Helmholtz free energy per unit mass. Indeed, eq. (3.28) is the thermodynamic governing equation which shall be satisfied for any process associated with mechanical deformation. In case of isothermal deformation, eq. (3.28) is simplified as

$$\phi = \boldsymbol{\sigma} : \dot{\boldsymbol{\varepsilon}} - \rho\dot{\psi} \geq 0. \tag{3.29}$$

**State variables** As a dissipative process, material state is described by the state variables and the associated variables. Let $\psi$ be a function of all the state variables, as

$$\psi = \psi(\boldsymbol{\theta}, \boldsymbol{\beta}), \tag{3.30}$$

where $\boldsymbol{\theta}$ is a collection of the observable variables, namely $\boldsymbol{\theta}\ \{\theta_i | i = 1, \cdots, n\}$, and $\boldsymbol{\beta}$ for the internal (or invisible) variables, as $\boldsymbol{\beta}\ \{\beta_i | i = 1, \cdots, n\}$. For any $\beta_i$, $B_i$ is the associated variable given by

$$B_i = -\rho \frac{\partial \psi}{\partial \beta_i}. \tag{3.31}$$

In the case of isothermal elastic damage, let the local Helmholtz free energy be a function of elastic strain $\boldsymbol{\varepsilon}^e$ and isotropic damage $D$, namely $\psi(\boldsymbol{\varepsilon}^e, D)$. Equation (3.29) can be rewritten as

$$\phi = \left(\boldsymbol{\sigma} - \rho \frac{\partial \psi}{\partial \boldsymbol{\varepsilon}^e}\right) : \dot{\boldsymbol{\varepsilon}}^e - \rho \frac{\partial \psi}{\partial D}\dot{D} \geq 0. \tag{3.32}$$

The equality holds under the following conditions,

$$\dot{D} = 0, \tag{3.33}$$

and

$$\boldsymbol{\sigma} = \rho \frac{\partial \psi}{\partial \boldsymbol{\varepsilon}^e}, \tag{3.34}$$

with which the constitutive equation for stress tensor is obtained. Since the inequality must be satisfied for any elastic deformation dominated damage process, it requires

$$-\rho \frac{\partial \psi}{\partial D}\dot{D} \geq 0. \tag{3.35}$$

Classically, the damage associated variable $Y := -\rho\frac{\partial\psi}{\partial D}$ is often considered as a thermodynamic driving force of damage evolution, given by a positive quadratic function of elastic strain energy per unit volume as

$$Y = \frac{1}{2}\boldsymbol{\varepsilon}^e : \mathbb{C} : \boldsymbol{\varepsilon}^e. \tag{3.36}$$

Therefore, the damage evolution rate $\dot{D}$ has to be always non-negative, namely

$$\dot{D} \geq 0. \tag{3.37}$$

For isothermal elasticity coupled damage with plasticity behaviour in the small deformation scenario, $\psi$ can be separated into two parts as

$$\psi(\boldsymbol{\varepsilon}^e, p, D) = \psi^e(\boldsymbol{\varepsilon}^e, D) + \psi^p(\bar{\varepsilon}^p), \tag{3.38}$$

with damage and elastic deformation governed by $\psi^e$, and $\psi^p$ is a function responsible to plastic deformation [61]. Here $\bar{\varepsilon}^p$ denotes the effective plastic strain, a scalar valued internal state variable, obtained from plastic strain tensor rate $\dot{\boldsymbol{\varepsilon}}^p$ as

$$\bar{\varepsilon}^p = \int_0^t \sqrt{\frac{1}{2}|\dot{\boldsymbol{\varepsilon}}^p : \dot{\boldsymbol{\varepsilon}}^p|}dt. \tag{3.39}$$

The time derivative of $\psi$ is written as

$$\dot{\psi} = \frac{\partial\psi^e}{\partial\boldsymbol{\varepsilon}^e} : \dot{\boldsymbol{\varepsilon}}^e + \frac{\partial\psi^e}{\partial D}\dot{D} + \frac{\partial\psi^p}{\partial\bar{\varepsilon}^p}\dot{\bar{\varepsilon}}^p, \tag{3.40}$$

which introduces the effective stress as

$$\bar{\sigma} = -\rho\frac{\partial\psi^p}{\partial\bar{\varepsilon}^p}. \tag{3.41}$$

Assume that the total strain tensor $\boldsymbol{\varepsilon}$ can be decomposed into the elastic part $\boldsymbol{\varepsilon}^e$ and the plastic part $\boldsymbol{\varepsilon}^p$. The cause of total energy dissipation is then separated by the elastic-damage $\phi^d$ and the plastic deformation $\phi^p$. Thus, eq. (3.29) can be rewritten as

$$\phi = \underbrace{\left(\boldsymbol{\sigma} - \rho\frac{\partial\psi^e}{\partial\boldsymbol{\varepsilon}^e}\right) : \dot{\boldsymbol{\varepsilon}}^e - \rho\frac{\partial\psi^e}{\partial D}\dot{D}}_{\phi^d \geq 0} + \underbrace{\boldsymbol{\sigma} : \dot{\boldsymbol{\varepsilon}}^p - \rho\frac{\partial\psi^p}{\partial\bar{\varepsilon}^p}\dot{\bar{\varepsilon}}^p}_{\phi^p \geq 0} \geq 0. \tag{3.42}$$

To sufficiently satisfy the Clausius-Duhem inequality, the conditions, $\phi^d \geq 0$ and $\phi^p \geq 0$, have to be fulfilled. Both the elastic and elastoplastic scenarios are reviewed above because they are considered in previous studies on the modelling of concrete damage (see chapter 4).

**Damage criterion** For material modelling, the damage evolution rate given by eq. (3.37) should always be satisfied to ensure thermodynamic consistency. To obtain a mathematical expression of $\dot{D}$, a scalar quantity $F^d$ is introduced to define the elastic domain. It is a function convex in $Y$ with dependency on further variables, i.e.

$$F^d = F^d(Y, \cdots). \tag{3.43}$$

Let $\Lambda$ denote the Lagrange multiplier. A Lagrange function can be given by

$$\mathcal{L} = \rho\frac{\partial\psi}{\partial D}\dot{D} + \Lambda F^d \quad \text{with} \quad -Y = \rho\frac{\partial\psi}{\partial D}. \tag{3.44}$$

The stationary solution of eq. (3.44), which indicates the maximum energy dissipation, is obtained by solving the optimisation problem

$$\frac{\partial\mathcal{L}}{\partial Y} = -\dot{D} + \Lambda\frac{\partial F^d}{\partial Y} = 0, \tag{3.45}$$

with which the damage evolution is given by

$$\dot{D} = \Lambda\frac{\partial F^d}{\partial Y}. \tag{3.46}$$

Usually, $\Lambda$ is replaced by a function $\Phi$ depending on the increment of $Y$ as

$$\dot{D} = \Phi(\dot{Y})\frac{\partial F^d}{\partial Y}. \tag{3.47}$$

The expression of $\dot{D}$ may vary from materials and loading configurations. Meanwhile, identification of damage model parameters strongly relies on experimental data. Applications on different types of damage problem, e.g. ductile fracture, brittle fatigue, can be reviewed from [58, 60, 61].

For elastic damage, $\dot{D}$ is suggested by Lemaitre [57] to be proportional to $Y \cdot \dot{Y}$, namely

$$\dot{D} \propto Y \cdot \dot{Y}. \tag{3.48}$$

In this case, the Lagrange multiplier is replaced directly by $\dot{Y}$, and $F^d$ is proportional to $Y^2$. The damage evolution for both loading and unloading situations has to satisfy the Karush-Kuhn-Tucker (KKT) conditions given by

$$\begin{cases} \Lambda \geq 0 \\ F^d \leq 0 \\ \Lambda F^d = 0 \end{cases}. \tag{3.49}$$

It assumes that damage grows only during the loading phase, whereas it keeps constant for unloading [2]. Since the strain energy release rate $Y$ is a dominant variable to the damage and its propagation, a threshold defined in terms of $Y$, i.e. $Y_D$, is introduced to judge the initiation of damage growth. Given eq. (3.36) for elastic damage, the expression of $Y_D$ is written as

$$Y_D = \frac{1}{2}\boldsymbol{\varepsilon}^e_D : \mathbb{C} : \boldsymbol{\varepsilon}^e_D, \tag{3.50}$$

where $\boldsymbol{\varepsilon}^e_D$ is the minimum strain for damage growth. Combined with the Kuhn-Tucker conditions, the thermodynamically consistent damage evolution can be delivered as

$$\dot{D} = \begin{cases} \Phi(\dot{Y})\frac{\partial F^d}{\partial Y} & \text{if} \quad Y > Y_D \ \text{ and } \ \dot{Y} > 0 \\ 0 & \text{otherwise.} \end{cases} \tag{3.51}$$

In summary, material damage is a thermodynamic dissipative process. The damage variable $D$ is interpreted as an average of micro-defects in the REV bounded between 0 and 1. The damage evolution rate $\dot{D}$ is restricted by the thermodynamic principles as a non-negative quantity. For general solid material, damage evolution rate shall be related to the elastic energy release rate $\dot{Y}$ [54, 60, 2]. Particularly for concrete damage, modelling approaches are reviewed in chapter 4.

# Chapter 4

# Deterministic and Stochastic Damage Constitutive Laws of Concrete

Modelling of material constitutive relation is the core of computational mechanics, as it defines the fundamental internal strain and stress relation of the solid deformable body subjected to external effects. Due to the strong heterogeneous microstructure, the complexity in constitutive modelling of concrete is considerably high. In the past decades, multiple theories, e.g. classical elastic mechanics, elastoplastic mechanics and fracture mechanics, have been continuously implemented on this topic. However, the lack of a comprehensive description of the mechanical reaction of deformed concrete still exists after an enormous amount of investigations into these theories. Due to the difficulties in constitutive modelling, studies on concrete structures maintained at the empirical level until the 1980s. After that, the concept of continuum damage mechanics has been planted in material modelling. It brings new possibilities for refined analysis of the mechanical behaviour of concrete structures.

Phenomenological approaches study the influence of damage on mechanical performance at the macroscopic level using continuum mechanics. In contrast, mesoscopic approaches aim to describe material textile architecture at a lower scale. These methods are often associated with kinematic constrains and homogenisation techniques, such as using the micro-plane theory and parallel strings. Comparing the completeness of reflecting the characteristics of material damage, there are deterministic (or incomplete) and stochastic (with limited completeness) damage models exposed by literature. Classical deterministic models are generally classified as the ones based on macroscopic CDM theories [62, 61, 63, 64], and those using micro plane theory [65, 66, 67]. In contrast, for stochastic damage modelling, the phenomenological approaches are proposed in [23, 25], whereas at the mesoscale parallel-spring models can be seen in [68, 27, 69]. This chapter briefly reviews both deterministic and stochastic damage models of concrete material, which can be applied on fatigue computation. Since mesoscale approaches are not the goal of this study, only macroscopic models are involved in detailed discussion.

## 4.1 Deterministic CDM Models for Concrete

It is commonly agreed that a general CDM model exhibits the following three characteristics [62, 61, 63, 2]:

1. a thermodynamic potential is defined to establish the relation between state variables and the corresponding conjugated thermodynamic force.

2. a dissipation potential is clarified to govern the irreversible thermodynamic process.

3. a damage evolution law is proposed with a certain damage criteria.

For concrete material two main issues have been intensively discussed by literatures while formulate their models, i.e. the damage evolution driving variable and the unilateral effect. Two resent studies [70, 9] proceed a systemic study on the classification of CDM models by their driving variables and selection of damage criteria. The study [70] agrees to relate damage to a measure of strain, which are specified in literatures as total strains [63], elastic strains [62] and sliding strains [64], etc. Regarding the damage criteria, CDM models are compared by [9] as strain controlled [62, 61], stress controlled [71, 72] and damage conjugated thermodynamic force controlled [63, 64, 73]. As an extension of these two studies, an overview of classical CDM models for concrete material is presented in the following context to compare their modelling concept.

### 4.1.1 Brittle versus Plastic Damage

Compared to ductile materials, which perform significant plastic deformation before rupture, brittle damage often occurs with negligible plasticity. Elastic strain conduced damage is assumed by studies at the early stage as the main form of concrete failure [62, 74]. The unit volume Helmholtz free energy of elastic damage is given by

$$\rho\psi = \frac{1}{2}\mathbb{C}(1-D) : \boldsymbol{\varepsilon}^e : \boldsymbol{\varepsilon}^e, \tag{4.1}$$

in which the contribution of plastic deformation is fully omitted. In this framework, both elastic strain [74, 62] and elastic strain energy release rate [75] are individually employed as the damage driving variable to determine the damage evolution law and the damage criteria. For different applications, it is debatable to derive the damage evolution law by an empirical function or by a differential equation. Studies [74, 75] prefer to derive an explicit damage evolution function $\hat{f}$, which provides the damage value directly from the combination of state variable and material parameters, i.e.

$$D = \hat{f}(\boldsymbol{\theta}, \boldsymbol{\beta}, \cdots). \tag{4.2}$$

As an empirical formulation, it has considerable model brevity. Besides, function $\hat{f}$ is often introduced with good smoothness, which is beneficial for finite element analysis to get convergence. The simulated stiffness reduction of concrete within fewer loading cycles is similar to the experimental observations. However, the ability to describe the loading history is missing. On the contrary, an ODE is used by this study [62] to represent the rate-dependent damage evolution as

$$\dot{D} = \hat{g}(\boldsymbol{\varepsilon}^e, D; \dot{\boldsymbol{\varepsilon}}^e). \tag{4.3}$$

Via integral on time, this formulation can capture the damage historical dependence, such as long-range weak-strength cyclic load and random load. Meanwhile, brittle damage laws are further improved by the studies [76, 77, 78, 79] to model anisotropic damage behaviour.

Brittle damage law has a fundamental weakness because it neglects the non-linear plastic deformation, which is significant for concrete under compression. Since the late 1980s, researchers have introduced plasticity and its evolution rule into the constitutive damage relation. The free energy equation given by eq. (3.38) proposed in [61] is a simplified damage plasticity with its theoretical background established by Lemaitre [57]. The damage driving factor is the elastic strain energy release rate only and the contribution of plastic deformation to the growth of microcrack is neglected. However, these models which depends on brittle damage law and additive plasticity, as argued by [80], are physically improper. To couple damage evolution with plastic flow, a local free energy is considered in the study [80], namely

$$\psi(\boldsymbol{\varepsilon}, D, \boldsymbol{q}) = (1 - D)\psi^0(\boldsymbol{\varepsilon}^e, \boldsymbol{q}), \tag{4.4}$$

where $\boldsymbol{q}$ represents all the necessary variables for plasticity, and $\psi^0$ is the undamaged potential energy. The uncoupling of elastic and plastic potential function gives

$$\psi(\boldsymbol{\varepsilon}, D, \boldsymbol{q}) = (1 - D)\left(\psi_e^0(\boldsymbol{\varepsilon}^e) + \psi_p^0(\boldsymbol{q})\right). \tag{4.5}$$

Thus, the damage conjugated thermodynamic force depends on both the elastic strain and the plasticity governing variables as

$$Y = \rho\psi^0(\boldsymbol{\varepsilon}^e, \boldsymbol{q}) = \rho\psi_e^0(\boldsymbol{\varepsilon}^e) + \rho\psi_p^0(\boldsymbol{q}). \tag{4.6}$$

Since the strain-based damage criterion is only suitable for elastic damage, a damage threshold in terms of $Y$ is employed to overcome this weakness. This modelling approach is continuously developed by [66, 81], which has been successfully applied in modern commercial FE-software for concrete damage simulation.

Instead of the strain decomposition, a tensor $\boldsymbol{\omega}$ is employed to contain all the non-linear response, such as damage and plasticity, to be coupled with the total strain [63]. The free energy is then proposed as

$$\rho\psi(\boldsymbol{\varepsilon}, \boldsymbol{\omega}) = \frac{1}{2}\lambda(\mathrm{tr}\boldsymbol{\varepsilon})^2 + \mu\mathrm{tr}(\boldsymbol{\varepsilon} : \boldsymbol{\varepsilon}) + g^a\mathrm{tr}(\boldsymbol{\varepsilon}, \boldsymbol{\omega}) + \alpha^a\mathrm{tr}(\boldsymbol{\varepsilon})\mathrm{tr}(\boldsymbol{\varepsilon}, \boldsymbol{\omega}) + 2\beta^a\mathrm{tr}(\boldsymbol{\varepsilon}, \boldsymbol{\varepsilon}, \boldsymbol{\omega}), \tag{4.7}$$

where $\lambda, \mu$ are the Lame constants, $\alpha^a, \beta^a, g^a$ are other material constants relate to moduli degradation and residual stress. In contrast, concrete damage is assigned to its inelastic strain, namely the sliding strain $\boldsymbol{\varepsilon}^\pi$ [64]. The free energy is proposed as

$$\rho\psi = \frac{1}{2}(1 - D)\boldsymbol{\varepsilon} : \mathbb{C}_1 : \boldsymbol{\varepsilon} + (1 - D)(\boldsymbol{\varepsilon} - \boldsymbol{\varepsilon}^\pi) : \mathbb{C}_2 : (\boldsymbol{\varepsilon} - \boldsymbol{\varepsilon}^\pi) + \frac{1}{2}Kz^2 + \frac{1}{2}\gamma\boldsymbol{\alpha} : \boldsymbol{\alpha}, \tag{4.8}$$

in which $\mathbb{C}_1$ and $\mathbb{C}_2$ are components of the full elasticity tensor after decomposition, scalar $z$ and $\boldsymbol{\alpha}$ are the isotropic hardening variable and kinematic hardening tensor, $K$ and $\gamma$ are moduli for isotropic and kinematic hardening. The above two models are tested on fatigue problem with 50 loading cycles, showing similar results, and comparable numerical efficiency [70].

The classical elastic-plastic damage theory is suitable to predict the material behaviours, such as ductile failure and low-cycle fatigue in which plastic deformations are often observable at the macroscopic level [2, 82]. However, the high-cycle fatigue (HCF), as a key design factor of engineering concrete structures, is difficult to be modelled by the conventional yield surface theory

[56]. The main difficulty is that the HCF loading strength is far smaller than the dominant yield stress, with which the material state shall be macroscopically elastic. This conflict between the model property and physical demands restricts the application of damage plasticity models on concrete HCF problem. Alternatively, some multi-scale approaches are invented to overcome the shortage of classical single scale models, by considering the localised plastic deformation at the micro level, e.g. the two-scale damage model [54, 5].

Often the computational cost of the return mapping algorithm for damage plasticity is very high, especially when multiple scales are involved. For the demand of fine space discretisation and large-time-interval, structural analysis can be costly, such that the advantage of simulation vanishes. In contrast, a generalised macroscopic rate-dependent brittle damage model, focusing on the strength loss process with a proper damage criteria of loading and unloading, can be suitable for concrete HCF simulation due to two main reasons. First, brittle damage and concrete HCF share common features, e.g. mainly elastic strain is observed at the RVE level before the initiation of macroscopic cracks. Second, compared to the two-scale models, the brittle damage model has fewer internal variables, which is computationally cheaper with less complexity while implementing the jumping-cycle algorithm.

### 4.1.2 Modelling of Unilateral Effect

Engineering brittle materials, such as concrete, ceramic, glass, exhibit considerably higher compressive strength than tensile strength. In practice, brittle materials are often used under heavy compressive load. The phenomenon of a general difference of material mechanical property in correlation with the loading sign is named unilateral. Observations at the microscopic level show that the macroscopic mechanical performance reduces when micro-cracks are opened by tension. However, when the micro-cracks are closed by compression, they are nearly non-effective to the material macroscopic behaviour. Due to the closure effect, the damage evolution rate under tension is generally higher than under compression. This inequality from the prospective of physics can be considered an anisotropic character, although the material is isotropic [83].

Theoretically, the unilateral effect shall be represented by a fourth-rank damage tensor. However, the numerical difficulties are discussed in many references [56, 84, 85]. The model complexity is also noticeable, despite a second-order damage tensor is implemented [86, 87, 88, 84]. In comparison, the effort in implementation and computation can be significantly reduced by using scalar damage variable. In order to simulate the micro-crack closure effect, it is commonly agreed by the literature to assign unequal damage evolution for tension and compression. Different modelling approaches specified for isotropic brittle damage including unilateral phenomenon are compared in the following context.

**Chow and Wei's model [89]** This approach considers two damage variables $D_{(1)}$ and $D_{(2)}$ with which two new scalar variables $D_w$ and $\mu_w$ shall be formed as follows,

$$D_w = 1 - \frac{(1 - D_{(1)})(1 - D_{(1)} - D_{(2)}) - 2D_{(2)}^2}{1 - D_{(1)} - D_{(2)}}, \tag{4.9}$$

$$\mu_w = \frac{D_{(2)}}{(1 - D_{(1)} - D_{(2)})}. \tag{4.10}$$

Depending on the variable setting the explicit expressions of damaged Young's modulus $\tilde{E}_w$ and Poisson's ratio $\tilde{\nu}_w$ are given by

$$\tilde{E}_w(D_w, \mu_w) = \frac{E(1-D_w)^2}{1-4\nu\mu_w + 2(1-\nu)\mu_w^2}, \tag{4.11}$$

and

$$\tilde{\nu}_w(D_w, \mu_w) = \frac{v_0 - 2(1-\nu)\mu_w - (1-3\nu)\mu_w^2}{1-3\nu\mu_w + 2(1-\nu)\mu_w^2}, \tag{4.12}$$

where $E$ and $\nu$ denote the undamaged material Young's modulus and Poisson's ratio respectively. The second-order elastic tensor for damaged material in Voigt notation yields to

$$\tilde{\mathbf{C}}^{-1}(D_w, \mu_w) = \frac{1}{\tilde{E}_w}\begin{bmatrix} 1 & -\tilde{\nu}_w & -\tilde{\nu}_w & 0 & 0 & 0 \\ -\tilde{\nu}_w & 1 & -\tilde{\nu}_w & 0 & 0 & 0 \\ -\tilde{\nu}_w & -\tilde{\nu}_w & 1 & 0 & 0 & 0 \\ 0 & 0 & 0 & 2(1+\tilde{\nu}_w) & 0 & 0 \\ 0 & 0 & 0 & 0 & 2(1+\tilde{\nu}_w) & 0 \\ 0 & 0 & 0 & 0 & 0 & 2(1+\tilde{\nu}_w) \end{bmatrix}. \tag{4.13}$$

The isotropic damage can be modelled by eq. (4.13), although the Young's modulus and Poisson's ratio are influenced by damage in different intensity. For the unilateral effect a scalar parameter $\alpha_w$ is introduced as an efficiency factor to adjust the damage caused by tensile stress $\boldsymbol{\sigma}$ and compressive stress $-\boldsymbol{\sigma}$. Combing the contribution of two directions, an arbitrary active stress tensor $\boldsymbol{\sigma}_{act}$ is obtained as

$$\boldsymbol{\sigma}_{act} = \langle \boldsymbol{\sigma} \rangle + \alpha_w \langle -\boldsymbol{\sigma} \rangle. \tag{4.14}$$

The Macaulay brackets $\langle \bullet \rangle$ denote the positive part of the quantity $\bullet$, i.e. $\langle \bullet \rangle = \max(\bullet, 0)$. Using this notation the tension and compression are separated without losing the thermodynamic consistency and their differentiability with respect to the full stress tensor. The free energy for brittle damage material using this method is given by

$$\rho\psi_W = \frac{1}{2}\boldsymbol{\sigma}_{act} : \tilde{\mathbf{C}}^{-1}(D_w, \mu_w) : \boldsymbol{\sigma}_{act}. \tag{4.15}$$

The disadvantages of this method are pointed out as follows. First, the strongly coupling of the two damage variables $D_{(1)}$ and $D_{(2)}$ raises computational costs. Second, extra efforts are needed for determining the unilateral effect parameter.

**Mazars model [61, 75]** The total damage is assumed as a linear combination of two scalar damage variables, $D^+$ and $D^-$, caused by tension and compression respectively. The expression of the coupling is given by

$$D = \alpha^+ D^+ + \alpha^- D^-, \tag{4.16}$$

where the parameters $\alpha^+$ and $\alpha^-$ are determined by the principle strains as

$$\alpha^+ = \sum_{i=1}^{3} \frac{\langle \varepsilon_i \rangle \langle \varepsilon_i \rangle}{\langle \varepsilon_1 \rangle + \langle \varepsilon_2 \rangle + \langle \varepsilon_3 \rangle}, \tag{4.17}$$

and

$$\alpha^- = \sum_{i=1}^{3} \frac{\langle -\varepsilon_i \rangle \langle \varepsilon_i \rangle}{\langle \varepsilon_1 \rangle + \langle \varepsilon_2 \rangle + \langle \varepsilon_3 \rangle}. \tag{4.18}$$

Although the value of $D^+$ and $D^-$ are obtained explicitly by empirical functions, the highlight of this idea is to separate the damage from tension and compression.

**Ladeveze and Lemaitre's model [54, 90]** The volumetric part is obtained from tensor decomposition with respect to the full stress tensor. After that, a scalar closure parameter $h$ is embedded to tune the damage evolution caused by compression. A special free energy for brittle damage is then represented as

$$\rho\psi_L = \frac{1+\nu}{2E}\left[\frac{\langle \boldsymbol{\sigma} \rangle : \langle \boldsymbol{\sigma} \rangle}{1-D} + \frac{\langle -\boldsymbol{\sigma} \rangle : \langle -\boldsymbol{\sigma} \rangle}{1-hD}\right] - \frac{\nu}{2E}\left[\frac{\langle \mathrm{tr}\boldsymbol{\sigma} \rangle^2}{1-D} + \frac{\langle -\mathrm{tr}\boldsymbol{\sigma} \rangle^2}{1-hD}\right], \tag{4.19}$$

The strain-stress relationship is obtained by the first order derivative regarding to $\boldsymbol{\sigma}$, namely

$$\boldsymbol{\varepsilon} = \rho\frac{\partial\psi_L}{\partial\boldsymbol{\sigma}} = \frac{1+\nu}{2E}\left[\frac{\langle \boldsymbol{\sigma} \rangle}{1-D} + \frac{\langle -\boldsymbol{\sigma} \rangle}{1-hD}\right] - \frac{\nu}{2E}\left[\frac{\langle \mathrm{tr}\boldsymbol{\sigma} \rangle}{1-D} + \frac{\langle -\mathrm{tr}\boldsymbol{\sigma} \rangle}{1-hD}\right]\mathbf{I}, \tag{4.20}$$

where $\mathbf{I}$ is the second order identity matrix. The inverse of the elastic tensor with isotropic damage can be given by the second order derivative as

$$\begin{aligned}\tilde{\mathbb{C}}^{-1} = \rho\frac{\partial^2\psi_L}{\partial\boldsymbol{\sigma}^2} =& \frac{1+\nu}{2E}\left[\frac{1}{1-D}\frac{\langle \boldsymbol{\sigma} \rangle}{|\boldsymbol{\sigma}|} + \frac{1}{1-hD}\frac{\langle -\boldsymbol{\sigma} \rangle}{|\boldsymbol{\sigma}|}\right]\mathbb{I} \\ &- \frac{\nu}{2E}\left[\frac{1}{1-D}\frac{\langle \mathrm{tr}\boldsymbol{\sigma} \rangle}{|\boldsymbol{\sigma}|} + \frac{1}{1-hD}\frac{\langle \mathrm{tr}\boldsymbol{\sigma} \rangle}{|\boldsymbol{\sigma}|}\right]\mathbf{I}\otimes\mathbf{I},\end{aligned} \tag{4.21}$$

The parameter $h$ is theoretically bounded by $[0, 1]$. When $h = 0$ it means the material strength is fully recovered under compression, or no damage caused by compressive load. For $h = 1$, the closure effect is deactivated. It is recommended by the literature to reduce the contribution from compression by assigning $h \approx 0.2$. The advantage of this method is also evident that no extra damage variable is required.

Based on the pattern of brittle failure, literature agrees that tension caused damage is often dominant, whereas the contribution from compression is negligible [63, 91, 56]. A frequently made assumption is that stiffness recovers fully by crack-closure, namely $h = 0$. For example, the free energy considered by Hürkamp and Nackenhorst [82],

$$\rho\psi_H = \frac{1}{2E}\left[\frac{\langle \boldsymbol{\sigma} \rangle : \langle \boldsymbol{\sigma} \rangle}{1-D} + \langle -\boldsymbol{\sigma} \rangle : \langle -\boldsymbol{\sigma} \rangle\right] + \frac{\nu}{2E}\left[\boldsymbol{\sigma} : \boldsymbol{\sigma} - \mathrm{tr}^2\boldsymbol{\sigma}\right], \tag{4.22}$$

assumes that the compression has no influence on damage. Similarly, using the deviatoric and volumetric stress tensor, namely $\boldsymbol{\sigma}_D$ and $\boldsymbol{\sigma}_H$, an effective stress is derived by Bhattacharyya et al. [12] as

$$\tilde{\boldsymbol{\sigma}} = \frac{\boldsymbol{\sigma}_D}{1-D} + \left[\frac{\langle \boldsymbol{\sigma}_H \rangle}{1-D} - \langle -\boldsymbol{\sigma}_H \rangle\right]\mathbf{I}, \tag{4.23}$$

in which the compressive volumetric stress is not assigned to damage. For particular loading scenarios, e.g. the four-point bending, these models [82, 12] meet however some numerical difficulties such as unrealistic stress concentration. In practice, the contact problem between the specimen and the supports are often simplified as nodal displacement constrains. For short beams, this configuration causes stress concentration in the finite elements near to the supports, rather than at the bottom centre of the beam. To avoid the expensive computation of contact problem, while obeying experimental observations, a new damage model for isotropic brittle material is needed.

### 4.1.3 A New Isotropic Brittle Damage Model

In view of [12] the free energy per unit volume for material elastic deformation can be written as a contribution of the deviatoric and volumetric part as

$$\rho\psi = \underbrace{G\boldsymbol{\varepsilon}^e_D : \boldsymbol{\varepsilon}^e_D}_{\text{deviatroic}} + \underbrace{\frac{K}{2}\Big[\langle \operatorname{tr}\boldsymbol{\varepsilon}^e\rangle^2 + \langle -\operatorname{tr}\boldsymbol{\varepsilon}^e\rangle^2\Big]}_{\text{volumetric}}, \tag{4.24}$$

where $\boldsymbol{\varepsilon}^e_D$ is the deviatoric strain tensor obtained via

$$\boldsymbol{\varepsilon}^e_D = \boldsymbol{\varepsilon}^e - \boldsymbol{\varepsilon}^e_H \mathbf{I}, \tag{4.25}$$

with the hydrostatic strain $\boldsymbol{\varepsilon}^e_H$ given by

$$\boldsymbol{\varepsilon}^e_H = \frac{1}{3}\operatorname{tr}\boldsymbol{\varepsilon}^e. \tag{4.26}$$

The bulk and shear modulus are denoted by $K$ and $G$, respectively. While assuming the fully effective crack-closure [82], the free energy for isotropic brittle damage reads

$$\rho\psi = G\,(1-D)^{\varphi}\,\boldsymbol{\varepsilon}^e_D : \boldsymbol{\varepsilon}^e_D + \frac{K}{2}\Big[(1-D)\,\langle \operatorname{tr}\boldsymbol{\varepsilon}^e\rangle^2 + \langle -\operatorname{tr}\boldsymbol{\varepsilon}^e\rangle^2\Big], \tag{4.27}$$

where $\varphi$ is a positive parameter with a value between $[0, 1]$. The introduction of this parameter is used to adjust the damage contribution of the deviatoric part [92]. According to eqs. (3.34) and (3.36), the stress tensor and the thermodynamic force are given by

$$\boldsymbol{\sigma} = \rho\frac{\partial\psi}{\partial\boldsymbol{\varepsilon}} = 2G\,(1-D)^{\varphi}\,\boldsymbol{\varepsilon}_D + K\Big((1-D)\,\langle \operatorname{tr}\boldsymbol{\varepsilon}\rangle\,\mathbf{I} - \langle -\operatorname{tr}\boldsymbol{\varepsilon}\rangle\,\mathbf{I}\Big), \tag{4.28}$$

and

$$Y = -\rho\frac{\partial\psi}{\partial D} = G\varphi\,(1-D)^{\varphi-1}\,\boldsymbol{\varepsilon}_D : \boldsymbol{\varepsilon}_D + \frac{K}{2}\,\langle \operatorname{tr}\boldsymbol{\varepsilon}\rangle^2. \tag{4.29}$$

The damaged material elastic tensor is obtained by

$$\tilde{\mathbb{C}} = \frac{\partial\boldsymbol{\sigma}}{\partial\boldsymbol{\varepsilon}} = \rho\frac{\partial^2\psi}{\partial\boldsymbol{\varepsilon}^2} = 2G\,(1-D)^{\varphi}\,\mathbb{P} + \left[(1-D)\frac{\langle \operatorname{tr}\boldsymbol{\varepsilon}\rangle}{|\operatorname{tr}\boldsymbol{\varepsilon}|} - \frac{\langle -\operatorname{tr}\boldsymbol{\varepsilon}\rangle}{|\operatorname{tr}\boldsymbol{\varepsilon}|}\right] K\,\mathbf{I}\otimes\mathbf{I}, \tag{4.30}$$

where $\mathbb{P} = \dfrac{\partial\boldsymbol{\varepsilon}_D}{\partial\boldsymbol{\varepsilon}}$ is a fourth order projection matrix.

Inspired by [2] the damage dissipative potential is defined as follows

$$F^d = \frac{S}{s_1 + 1} \left\langle \frac{Y}{S} \right\rangle^{s_1+1} - Y_D, \tag{4.31}$$

in which $s_1$ and $S$ are the material parameters, $Y_D$ is the damage threshold defined in terms of energy release rate. The expression of $Y_D$ is given by a linear function of damage as

$$Y_D = SD + Y_{D0}, \tag{4.32}$$

in which $Y_{D0}$ is the initial damage threshold as a material constant. With this configuration the damage surface $f^d$ can be written in the form

$$f^d = F^d = f(Y) - g(D) \leq 0. \tag{4.33}$$

The damage evolution can be obtained from the derivation of $F^d$ with respect to $Y$ via the normality law as

$$\dot{D} = \Phi(\dot{Y}) \frac{\partial F^d}{\partial Y}. \tag{4.34}$$

Let the concave function $\Phi$ defined by $\dot{Y}$ with material parameter $s_2$ as

$$\Phi(\dot{Y}) = \left\langle \dot{Y} \right\rangle^{s_2}. \tag{4.35}$$

In view of eq. (3.47) the damage evolution law for brittle material is given by

$$\dot{D} = \left\langle \frac{Y}{S} \right\rangle^{s_1} \left\langle \dot{Y} \right\rangle^{s_2}. \tag{4.36}$$

Equation (4.36) allows damage to increase only if $Y$ is over the threshold under loading, whereas during the unloading phase, damage remains constant, namely $\dot{D} = 0$. Using this assumption, $\dot{D}$ is strictly restricted to be non-negative, which is consistent to its thermodynamic constrains.

## 4.2 Stochastic Damage Models

Experiments show that damage evolution at the macro-level have considerable randomness [10]. This natural property is less interpreted by deterministic damage models since statistically it covers only the mean of material damage [23]. The stochastic modelling approach is developed under the demand of reliability analysis for a comprehensive probabilistic description of the damage process. Generally, microstructural heterogeneity and environmental fluctuation are the main factors of uncertain damage evolution. In the CDM framework, efforts are made on building phenomenological models, e.g. modelling of uncertain damage variable, introducing of stochastic thermodynamic potentials [23, 93, 31, 25, 24, 94]. In contrast, micromechanics based approaches relate the phenomenon of uncertain material damage to its root at the lower scale, e.g. inhomogeneous microstructure. The parallel-spring model [68] and its variations [26, 27, 28] are commonly used to simulate the material behaviour at the micro-scale in which the failure of micro-elements follow a particular random distribution. The macro-scale behaviour is interpreted by the statistics at the lower scale using the micro-macro transition.

### 4.2.1 CDM Based Phenomenological Approaches

**Woo and Li's model [23]** The idea is to modify the damage evolution rate as a stochastic differential equation in the form

$$\frac{d\,\tilde{D}}{dt} = g(t, D(t)) + h(t, D(t))\,\xi_t^N, \quad \forall t \geq 0, \tag{4.37}$$

where $\xi_t^N$ is Gaussian white noise, $g$ and $h$ are drift and diffusion depending on time and damage. With initial value $D(t_0)$ the solution of stochastic damage evolution is given by the time integral of above equation from $t_0$ to $t$ as

$$\tilde{D}(t, \omega) = D(t_0) + \int_{t_0}^{t} g\; ds + \int_{t_0}^{t_1} h\; d\,W, \tag{4.38}$$

which is a stochastic process. The mean of stochastic damage evolution has to be unbiased from the deterministic one. Therefore, it is suggested to replace $g$ by the deterministic damage evolution rate $\dot{D}$. The diffusion term is considered as proportional to the drift namely

$$h(t, D(t)) = \zeta \dot{D}, \tag{4.39}$$

in which $\zeta$ is a constant.

The Ito integral $\int_{t_0}^{t} d\,W$ is preferred by this model, since with this interpretation the drift coefficient can be kept as identical to $\dot{D}$. Indeed, solving eq. (4.38) numerically is a direct approach to obtain the stochastic damage evolution. This approach is later on implemented by Silberschmidt [24] to test the convergence performance of 1.5 Taylor scheme. Another one, the indirect method, solves the corresponding Fokker-Planck equation [31]. It focuses on the development of damage transition probability $P(t, D(t); t_0, D(t_0))$, instead of individual trajectories of damage evolution.

Woo and Li's model has advantages in the model generality and brevity. Since expressions of the drift and diffusion term come directly from CDM, the mathematical scheme eq. (4.38) is flexible to simulate different types of damage progress, such as brittle, ductile, fatigue, and creep damage. The influence of uncertain material property and environmental variables on damage evolution is assumed to be fully interpreted by the diffusion term together with the Gaussian random variable. Thus, no extra effort is needed to modify the deterministic constitutive relation. The procedure of assigning randomness to the material parameters and environmental factors can also be avoided. This macroscopic model is numerically cheaper than the micro/mesoscopic approach because modelling of microstructural heterogeneity is not required. A major issue of this model is that the Gaussian random number cannot guarantee the positiveness of damage evolution rate. To this particular problem, detailed discussion and possible solutions are provided in chapter 6.

**Silberschmidt and Chaboche's work [31, 24]** The indirect approach for solving stochastic damage evolution is presented in [31], where the goal is to investigate the relation between random load and damage probability. The stochastic damage model is written as

$$\frac{d\,\tilde{D}}{dt} = g^s(\sigma, D) + \zeta^s \xi_t^N, \tag{4.40}$$

where $\zeta^s$ is the model constant, $g^s$ is a function of stress and damage. The expression of $g^s$ is given by a third-order polynomial as

$$g^s(\sigma, D) = -(a_1 D^3 + a_2 D^2 + a_3 D - a_4 \sigma), \tag{4.41}$$

which has a similar role as the drift term in eq. (4.38). The equivalent Fokker-Planck equation of the SDE eq. (4.40) is given by

$$\frac{\partial f}{\partial t} + \frac{d}{dD}\left(g^s(D) f - \frac{1}{2}\zeta^s \frac{\partial f}{\partial D}\right) = 0, \tag{4.42}$$

in which the general stationary solution at $\frac{\partial f}{\partial t} = 0$ is obtained as

$$f = \left[\int_{-\infty}^{+\infty} \exp(-2V/\zeta^s) dD\right]^{-1} \exp\left(-2V/\zeta^s\right), \tag{4.43}$$

with the expression of $V$ given by

$$V = \frac{1}{4}a_1 D^4 + \frac{1}{3}a_2 D^3 + \frac{1}{2}a_3 D^2 - a_4 \sigma D. \tag{4.44}$$

Although this study invests large effort to illustrate the output of eq. (4.43) with different combinations of stress and damage value, the results are inconsistent with the reality. First, the stationary solution eq. (4.40) is obtained after applying the natural boundary condition, i.e.

$$\lim_{D \to \pm\infty} f(D) = 0. \tag{4.45}$$

This setting contradicts the fundamental definition of damage in which $D$ is bounded between 0 and 1. Indeed, the transformation from eq. (4.42) to eq. (4.43) is restricted to a certain configuration of the function. For example, the boundary condition eq. (4.45) can be applied on the variable $X(t, \omega)$ with its original definition assigned to the displacement of the molecule. Second, loading fluctuations shall have observable influences on the damage growth, and the damage evolution rate has to be time-dependent. These facts are ignored by this work. A polynomial based damage law with stationary assumption of Fokker-Plank equation is convenient to obtain analytical expression of damage probability. However, as commented by [31], it is more general to seek for numerical non-stationary solution of eq. (4.42).

In another work [24], the SDE in eq. (4.40) is solved by the direct approach using the strong Taylor 1.5 scheme eq. (2.25) to present the influence of noise intensity on the stochastic damage evolution. The increase of damage uncertainty and the failure probability are positively correlated to the noise intensity. In contrast, the damage mean is relatively less perturbed while changing the noise configuration. Due to negative Gaussian random noise, damage evolution trajectories are observed with local decreasing trend. This outcome cannot agree with thermodynamic principles. However, the issue is neglected by this work without further discussion. Indeed, the two works [31, 24] share the common weakness that they emphasise on the investigation of numerical schemes, whereas the model feasibility is not verified by structural analysis using the finite element analyses.

**Bhattcharya and Ellingwood's model [25]** In this model the evolution of Helmholtz free energy is described as a stochastic process. For a representative time interval from $t_0$ to $t_1$, the random free energy $\tilde{\Psi}$ at $t_1$ is given by

$$\tilde{\Psi}(t_1) = \tilde{\Psi}(t_0) + \int_{t_0}^{t_1} \frac{d\tilde{\Psi}}{dt}\, dt + \int_{t_0}^{t_1} \frac{dB}{dt} dt. \tag{4.46}$$

The second integral in eq. (4.46) assumes the free energy fluctuation as a zero-mean process $B(t, \omega)$. From the macroscopic point of view, it is an ensemble of stochastic contributions in terms of microstructure heterogeneity and uncertain environmental factors. Based on eq. (4.46), a stochastic damage evolution law is derived for uniaxial load as

$$\frac{d\tilde{D}}{dt} = -\frac{\sigma_\infty}{Y}\dot{\boldsymbol{\varepsilon}}(D, t) - \frac{\dot{\boldsymbol{\varepsilon}}(D, t)}{Y} X^o(t, \omega), \tag{4.47}$$

where $\sigma_\infty$ is the far-field stress and $X^o$ denotes the free energy fluctuation per unit volume, namely $\frac{dB}{dV}$. The expression of $X^o$ is given by the Langevin equation with positive constant $m_1$ and $m_2$ as

$$\frac{dX^o}{dt} = -m_1 X^o + \sqrt{m_2}\xi^N. \tag{4.48}$$

Indeed, by choosing a sufficient large value for $m_1$, the solution $X^o(t, \omega)$ is guaranteed to be zero-mean and stationary named Ornstein-Uhlenbeck (OU) process, which is a member of Gaussian process family. In practices it is approximated by simple white noise following the Gaussian distribution $N(0, \frac{m_2}{m_1^2})$. Under this configuration eq. (4.47) can be written as

$$d\tilde{D} = -\frac{\sigma_\infty}{Y}\dot{\boldsymbol{\varepsilon}}(D, t)dt - \frac{\sqrt{m_2}/m_1}{Y}\dot{\boldsymbol{\varepsilon}}(D, t)dW_t, \tag{4.49}$$

with its solution given by

$$\tilde{D}(t, \omega) = D_0 - \int_{t_0}^{t} \frac{\sigma_\infty}{Y}\dot{\boldsymbol{\varepsilon}}(D, t)ds - \int_{t_0}^{t} \frac{\sqrt{m_2}/m_1}{Y}\dot{\boldsymbol{\varepsilon}}(D, t)dW_s. \tag{4.50}$$

This particular model has considerable similarity to the generalised one proposed by Woo and Li [23]. The closed-forms of ductile, creep, and fatigue damage evolution are derived based on eq. (4.46), followed by model validation studies. Investigations in this work are comprehensive for each type of damage, including discussions on the evolution of random damage paths, statistics of failure. The appearance of negative damage increment is also mentioned in this study. The probability of having unrealistic damage increment is demonstrated to be positively correlated to the time step size. Compared to the deterministic damage evolution, the mean of random damage growth can be underestimated by the Ito integral, whereas the Stratonovich integral does not have this problem. Random fatigue damage growth of ductile material are also illustrated, including statistics of virtual S-N data up to 1 million loading cycles. Although the model parameters (e.g. $\sqrt{m_2}/m_1$) are calibrated, the simulated S-N data has a significant bias to the experimental one, both in the mean and variance. Like the previously mentioned works, the essential step after introducing a damage law, i.e. structural analysis based model verification, is also missing in this study. Meanwhile, despite a closed-form stochastic damage evolution function can be derived from this particular damage law, its applicability to multi-axial problems is not clear.

### 4.2.2 Micromechanics Based Multi-Scale Approaches

Comparing to CDM based stochastic damage laws, microscopic modelling approaches share the common two key steps: statistics and homogenisation of microscopic damage contributions. A general statistical damage model for uniaxial tensile loading is established in [68], where the material microstructure is simplified by parallel-string-element. The element size is fixed, which originally contains $N$ parallel springs, each having identical stiffness $k$. For perfectly brittle material, each spring is assumed to break immediately and lose the functionality when its tensile strength $f_i$ reaches the critical value $f_i^R$. The critical strength for each string is a random variable (RV) to generate randomness in the number of broken springs which further induces element-wise damage fluctuation. The microdamage occurrence is determined by the chosen random distribution $f_i^R$. Using the Weibull distribution with shape and scale parameters $\alpha$ and $u$, damage evolution versus strain in individual element at micro-scale has the explicit form

$$D(k,\varepsilon) = 1 - \exp\left[-\left(\frac{k\varepsilon}{u}\right)^{\alpha}\right], \tag{4.51}$$

which is the Weibull cumulative distribution function (CDF). The macroscopic response is obtained by the homogenisation process, which is identical to eq. (4.51). The major weakness of this model is that the damage evolution is statistics-based. Thus it is not confirmed with the thermodynamic principles. Meanwhile, the CDF shaped macroscopic damage evolution is not realistic for brittle material.

A two-scale stochastic damage approach for brittle material is developed in [95, 26], where the microfracture is driven by the Weibull CDF, and the micro-macro transition is approximated by the simple bundle concept. The macroscopic damage at each Gauss point of the finite element mesh is determined by the state of the corresponding parallel spring bundle, namely

$$D = \frac{N_r}{N_t}, \tag{4.52}$$

where $N_r$ and $N_t$ are the numbers of rupture and total springs in a bundle, respectively. The bundle volume is given by $N_t$, which is assimilated with the REV in the CDM framework. The rupture of every single spring for a given strain $\varepsilon$ is considered as an individual occurrence of micro-defect, which has a probability $P_r(\varepsilon)$ given by the Weibull CDF as

$$P_r(\varepsilon) = 1 - \exp\left[-\left(\frac{\varepsilon}{u}\right)^{\alpha}\right]. \tag{4.53}$$

Under the assumption of strain equivalence, the expectation of $N_r$ is obtained by

$$\mathbb{E}(N_r) = P_r(\varepsilon) N_t, \tag{4.54}$$

with which the mean of macroscopic damage is deduced identical to eq. (4.53). In practices, $N_r$ is random in each spring bundle, which simultaneously produces uncertain macroscopic damage value at each Gauss point. The constitutive relation proposed in [75] is applied in the finite element computation with modified macroscopic damage law. Certain numerical issues such as catastrophic failure, convergence problem are discovered by this work. Increasing the model complexity can be a solution, e.g. introducing neighbouring element effect and interaction between micro-defects.

The study [27] assumes the failure strain $\varepsilon_r$ of each spring is random with correlation to its neighbours. A one-dimensional log-normal random field (RF) with correlation length $l_c$ is employed to simulate the spatial dependence. Macroscopic experimental data is used to obtain the model parameter at the micro-scale. This procedure is criticised by the work [69], due to the mixing of problem scales. Refined models are developed to capture multiaxial non-elastic behaviour of concrete, such as introducing the plastic deformable components into the spring bundle [69, 29]. Other models with higher complexity can be seen in [96, 30]. The four-element model, including main elastic, fracture, friction and secondary elastic elements, is designed to simulate the deteriorating hysteretic phenomenon of quasi-brittle materials. Indeed micromechanics based model with such a degree of refinement are less applied to engineering problems, mainly due to the high computational cost.

A summary of the stochastic damage models mentioned above can be seen in tables 4.1 and 4.2. In order to quantify the macroscopic uncertainties, micromechanics based approaches have to overcome two main challenges:

1. to properly configure macro/micro-scale models, such that the microscopic material heterogeneity can be captured and the material macroscopic continuity is respected simultaneously;

2. to propose a certain transition law between different scales, with which the statistics of microstructural behaviour can be projected to the larger scale, and the macro-scale outputs obey experimental results;

Generally, due to the high computational cost and model complexity, micromechanics approaches have considerable difficulties in mass application. Based on the well-developed theory of solid mechanics, a phenomenological approach focusing on the random reduction of material stiffness is continuously discussed in the following chapters.

Table 4.1: Comparison of CDM based phenomenological stochastic damage models

| work | model | uniqueness (+) / weakness (-) |
|---|---|---|
| Woo and Li [23] | $\delta\tilde{D} = g(D,t)dt + h(D,t)\ dW_t$, with $g$ and $h$ consistent to deterministic damage law. | (+) generalised framework with wide applicability;<br>(+) proposal of direct and indirect solution.<br>(-) less discussion on numerical implementation;<br>(-) possible negative damage evolution. |
| Silberschmidt and Chaboche [31] | $\delta\tilde{D} = g^s(\sigma,D)dt + \zeta^s\ dW_t$, with drift $g^s$ polynomial and $\zeta^s$ constant diffusion. | (+) Analytical solution of FPE.<br>(+) non-uniform damage evolution for principal and shear stress.<br>(-) idealised damage law (-) no structural analysis |
| Silberschmidt [24] | $\delta\tilde{D} = g^s(\sigma,D)dt + \zeta^s\ dW_t$ | (+) numerical investigation of strong Taylor 1.5 scheme<br>(-) missing structural analysis |
| Bhattcharya and Ellingwood [25] | $\begin{cases}\delta\tilde{D} = g(D,t)dt + h(D,t)dW_t \\ g = -\frac{\sigma_\infty}{Y}\dot{\boldsymbol{\varepsilon}}(D,t) \\ h = \frac{\sqrt{m_2}/m_1}{Y}\dot{\boldsymbol{\varepsilon}}(D,t)\end{cases}$ | (+) random damage law derived on the hypothesis of free energy fluctuation;<br>(+) applied on ductile, creep and fatigue damage.<br>(-) lack of structural implementation. |

Table 4.2: Comparison of micromechanics based multi-scale stochastic damage models

| work | model | micro-damage threshold | macro-damage evolution | uniqueness (+) / weakness (-) |
|---|---|---|---|---|
| Krajcinovic and Silva [68] | parallel-spring | rupture stress $\sigma_r$ Weibull RV | Weibull CDF | (+) macroscopic damage evolution derived from Weibull distribution.<br>(-) damage law far from reality;<br>(-) macroscopic random damage not presented. |
| Breysse [26] | parallel-spring | rupture strain $\varepsilon_r$ Weibull RV | Weibull CDF | (+) clear scale definition and transition law;<br>(+) integration to Mazars [61] theory.<br>(-) numerical unstable. |
| Kandarpa, Kirkner, and Spencer Jr [27] | parallel-spring | rupture strain $\varepsilon_r$ 1D log-normal RF | log-normal CDF | (+) continues function of damage evolution mean and variance.<br>(-) empirical RF. |
| Li and Ren [69] and Yu et al. [29] | parallel-spring | rupture strain $\varepsilon_r$ 1D log-normal RF | log-normal CDF | (+) plastic micro-components included;<br>(+) empirical elastic deformation rule for reducing computational cost.<br>(-) uniaxial loading only. |
| Ren and Li [96] and Feng, Ren, and Li [30] | four-element | rupture strain $\varepsilon_r$ 1D log-normal RF | log-normal CDF with friction amplitude | (+) residual strain interpreted by friction components;<br>(+) good accuracy under cyclic loading.<br>(-) computationally expensive. |

# Chapter 5

# Characteristics and Assessment of Brittle Fatigue

In structural engineering, fatigue leads to the loss of material mechanical performance, which risks the full functionality of the object. As a prior condition of fatigue assessment, it is necessary first to understand the fatigue mechanism and its pattern. An overview of this topic is given in the first section of this chapter, particularly regarding observations on the graphical interpretation of fatigue data. After that, the empirical and progressive approaches for fatigue assessment are reviewed.

## 5.1 Fatigue Characteristics

Fatigue is a special type of damage associated with cyclical loading, which is observed with progressive and permanent material stiffness reduction. It is initialised at the microlevel when an irreversible micro-strain activates the crack tips. At this stage, fatigue is often a de-acceleration process that the rate of micro-cracks evolution reduces with regard to the number of cycles. The second stage of fatigue is characterised by the steady growth of micro-cracks in the REV. The endurance of this stage is one of the significant factors to evaluate the material fatigue performance. Depending on the loading condition and the structure geometry, micro-cracks accumulate faster at some locations with intensive stress and strain concentration. Consequently, macroscopic cracks are likely to be generated at these locations, where damage quickly reaches its critical value. In the third stage, fatigue macro cracks propagate very fast and finally causes global failure. The fatigue life is defined by the number of loading cycles with which the catastrophic failure happens. In practices, it is the number cycle to observe macro cracks [97]. Generally, fatigue life can be extended while reducing the external load. If the life cycle approaches infinity, the corresponding load level is assigned to the fatigue limit. The Wöhler curve, often known as the S-N diagram, is widely used for the fatigue assessment of engineering instance. Through changing the quantity measured for load levels, the diagram can be interpreted as stress-life or strain-life for different analysis purposes.

Though the material state at the last stage of fatigue is beyond the CDM theory, fatigue life approximated by CDM based approach is significant for two reasons. First, fatigue life is dominated by the two phases before the initiation of macro-cracks in which the material continuity is sufficiently satisfied. Second, the crack location and the tip opening direction are predictable using damage mechanics, with a proper modelling of material behaviour under cyclic load [2].

Depending on the number of fatigue cycles, fatigue studies are generally categorised into three areas, low-cycle (LCF), high-cycle (HCF) and super-high-cycle fatigue. A clear division of these categories by the number of cycles is often controversial. For concrete material, a widely accepted classification considering the different applied situation is summarised in table 5.1.

Table 5.1: Classification of fatigue regimes for concrete [98]

| Low-cycle fatigue | High-cycle fatigue | | Very-high-cycle fatigue | |
|---|---|---|---|---|
| $1 \sim 10^2$ | $10^3 \sim 10^4$ | $10^5 \sim 10^6$ | $10^7 \sim 10^8$ | $\geq 10^9$ |
| Earthquake engineering | Airport pavement | Highway and railway bridges | Mass Rapid Transit (MRT) structures | Sea structures |

Due to the strong material heterogeneity, the fatigue mechanism of plain concrete is complex, having distinguishable differences in the low- and high-cycle regime. The main feature of low-cycle fatigue is the formulation of distributed mortar cracks with continuous crack networks. In contrast, steady development of bond cracks is often observable in high-cycle fatigue. The fatigue limit is a quantity in terms of load commonly used in fatigue design. If the applied load is lower than the fatigue limit, the material is considered unlimited fatigue life. Unlike metallic materials, a clear fatigue limit of concrete is difficult to determine because plain concrete shows a limited life cycle for almost any stress levels. A commonly used design criterion is to check the material safety after $2 \times 10^6$ cycles of fatigue load [98, 99]. If the fatigue life exceeds this amount of cycles, the applied load level is recorded as the fatigue limit. According to experimental studies on uniaxial [100, 101] and flexural [16, 17] test, the fatigue life of plain concrete in both low- and high-cycle cases can be improved significantly after adding fibre reinforcement into the volume. Through the ductile deformation and bridging process of the reinforcement, the energy that usually causes crack propagation in plain concrete can be intensively dissipated.

### 5.1.1 Testing Methods

Force and displacement controlled test are two standard approaches for fatigue experiment in which the strain (or stress) amplitude are constantly kept. Unlike the monotonic test, fatigue load levels are much lower than the material strength to observe the cyclic reaction. The displacement controlled approach is often implemented for the low-cycle test, with which the specimen performs considerable inelastic deformation. Specimens having special geometry, e.g. with notches, are generally tested by this method. The force-controlled test is preferred for small deformable specimen subjected to high-cycle fatigue load [97]. Although the strain/stress is constrained, the material reaction varies by cycles due to the irreversible reduction of material stiffness. The fatigue life of concrete obtained under the displacement controlled test is prolonged compared to the force-controlled experiment [102].

Except for measuring the strain and stress relationship, fatigue damage can be detected by modern non-destructive techniques, e.g. computed tomography (CT). Through monitoring the periodically changed microstructural density, it is possible to quantify the stiffness response at the

macro-level [103]. Innovative experimental techniques, e.g. based on acoustic or electromagnetic resonance, are invented for high-cycle and very-high-cycle fatigue test. Fatigue data can be collected up to $10^{10}$ cycles in practice [104]. With these approaches, specimens are stimulated at an ultrasonic frequency close to 20 kHz, that the experimental time consumption can be reduced intensively. This method is preferred for statistical studies because a large amount of fatigue data can be obtained within a manageable laboratory time. Meanwhile, it has considerable flexibility for different stress (or strain) constraints, loading ratio, frequency and amplitude. The applicability of this technique is proven on a uniaxial test of alloy [105], concrete [102], three-point bending of composite material [106] and large-scale beam from rail system [107]. Although the environmental factors are not fully in effect within the shortened testing time, the influence of temperature, humidity and corrosion are investigated using ultrasonic frequency test [104]. Since the testing frequency has considerable difference to the real application, comparative studies are necessary to present their correlations and possibly to reduce experimental errors.

Through distinguishing the loading directions, fatigue test is classified into compression/tension and flexural test. Since brittle materials are mainly applied against massive compression, attentions are emphasised on the compressive fatigue performance than pure tension [108]. Due to the unilateral effect, fatigue of concrete material under reversing and multi-axial load is rather complex. Very few experimental results are available in these areas. In contrast to the lack of laboratory studies, fatigue models for unilateral and multiaxial load are well established for concrete materials [77, 64, 8, 70].

The industrial standard of quality control, e.g. the DIN 50100-1978, recommends verifying the uniaxial compressive fatigue strength using a cubic or cylinder-shaped concrete specimen. The material compressive (or tensile) fatigue strength can be obtained by changing the monotonic load to cyclic load. Besides the uniaxial performance, flexural strength is of particular interest in designing bridges and concrete pavement. During flexural experiment concrete specimens are mostly formed as beams placed on two supporting pins and subjected under two or single loading pin(s). The beam's cross-section is often a square with the side length ranging from 100 to 150 mm, and the length of the beam varies between 0.5 to 2.0 m. The flexural strength is a material constant commonly expressed as modulus of rupture (MR) in terms of stress. Comparing to the pure compression/tension test flexural test has the following characteristics. First, the material reaction with this type of load is a combination of tension, compression and shearing. It exposes the material overall mechanical performance required in real-life applications. Second, flexural fatigue life is sensitive to the manufacturing/casting quality of the specimen. In contrast to uniaxial fatigue data the flexural fatigue data include often higher randomness [109], which is of great interest for statistical analyses. Experimental studies [110, 111, 112] report that compressive and flexural strength of concrete material are strongly correlated. Therefore, it is possible to determine the compressive strength using the flexural data as reference [113].

Before the fatigue test, the corresponding monotonic strength shall be determined in advance. The maximum cyclic stress (or strain) is configured as a percentage of the monotonic strength using the parameter load level $L_s$. By changing this value, one has a interval of loading levels for fatigue test. In practice the maximum fatigue load is preferred to be $0.5 \sim 0.9$ times of monotonic strength. Using the Euler–Bernoulli beam theory the maximum flexural stress can be approximated by the applied force and the specimen's geometry. For example, the three- and four-point flexural tests show in fig. 5.1 use a beam with the length of $L$ and the side length of $H$. The squared cross section of this beam $A_s$ is given by $H^2$. The distance between the two supports is $L_s$ and for four-point

test the distance of the loading points is $L_i$. A force $F$ is applied perpendicular to the beam via the pin(s). Depending on the number of loading pins, the maximum flexural stress is calculated as

$$\sigma_f^{3p} = \frac{3FL_s}{2H^3} \tag{5.1}$$

and

$$\sigma_f^{4p} = \frac{3F(L_s - L_i)}{2H^3} \tag{5.2}$$

for the three- and four-point flexural test respectively. The bending moment of the three-point test

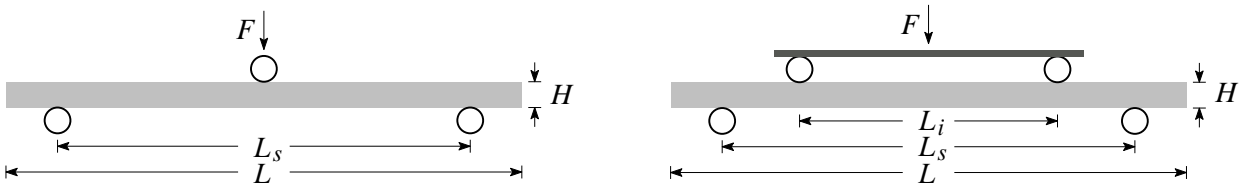


(a) three-point (b) four-point

Figure 5.1: Arrangement for a three- and four-point flexural test

has a triangle shape, which means the maximum flexural stress concentrates at the loading tip. However, the four-point has a trapezoidal shaped moment line, with which the flexural tress is well distributed between the loading points. This enables the four-point test to capture more realistic material reaction. For concrete material, the four-point fatigue life is generally longer than the three-point test [21]. However, the fatigue life of carbon-fibre composite material measured under three-point is smaller than the four-point setup [114]. In contrast, for ceramic, the result is on the opposite [115]. Besides the mean of fatigue life, the variation of flexural strength obtained by the four-point test is commonly greater than in the three-point test [114].

### 5.1.2 Frequency Effect

The stress (or strain) rate is proportional to the loading frequency by neglecting the change of material stiffness in one cycle. Based on the thermodynamics principles, mechanical energy is converted from the experiment machine into the internal energy of the specimen during the fatigue test. With the hypothesis of an isolated system, increasing the loading frequency for a given time interval can induce an evident rise of the material temperature because extra external work is applied. The correlation between the stress/strain ratio and the material temperature during fatigue is highly complex, relying on real-time microscopic observations. For simplicity, fatigue damage is modelled as an isothermal process in this study.

Generally, for low strength metallic materials, e.g. aluminium alloy, loading frequency is one of the dominant factors to fatigue strength. Compared to the loading frequencies $10 \sim 75$ Hz, the fatigue life of aluminium alloy is dramatically extended under 20 kHz test [116, 117], as well for the low carbon steel [118, 119]. However, frequency effect is very limited for high-strength metallic materials, especially for low-temperature-tempered steel [120, 121] and Ti–6Al–4V [122]. A statistical study by [28] covering the very-high-cycle regime of high-strength steel shows the same fatigue scatter band at 95 Hz and 20 kHz loading frequency.

The frequency effect on concrete material varies to its composition and other loading parameters, such as maximum cyclic stress. Studies on the frequency effect of plain concrete start in the 1930s using the uniaxial compressive test, showing that the frequency effect between 4.5 Hz and 7.5 Hz is slight, whereas the fatigue life reduced intensively if the frequency is below 0.16 Hz [123]. Another study [124] at the frequencies from 1 Hz to 15 Hz shows that the effect is negligible when the maximum cyclic stress is 0.75 times monotonic fracture strength, i.e. $L_s = 0.75$. Further investigations [125, 126] at 1, 10 and 200 Hz report no frequency effect when $L_s$ is less than 0.8. Once the factor is over 0.8, the frequency effect becomes however significant [127]. Fatigue life of four types of concrete materials are studied at 4 Hz, 1 Hz, 1/4 Hz and 1/16 Hz by [20] with $L_s = 0.85$. It shows that fatigue life and loading frequencies have a linear correlation on the log-log scale for plain concrete. However, high-strength concrete materials, such as the steel fibre reinforced concrete (SFRC) and the steel fiber reinforced self compacting concrete (SFRSCC), exhibit longer fatigue life with less frequency effect. Similar observations are reported in [102] using ultra-sonic-frequency test up to the very-high-cycle fatigue regime. A general description of frequency effect at different load levels can be seen in [4] in which the effect is consistently observed during the interval of $L_s$ from 0.6 to 0.95.

In conclusion, the frequency effect generally exists for various engineering materials. Its intensity depends on the combination of material static strength and the applied load level. For both metallic and concrete materials, the frequency effect and the static strength have a negative correlation, such that high-strength materials expose a more negligible frequency effect. For regular plain concrete, the frequency effect is significant when the fatigue load is near the static strength. By converting the fatigue life into the total duration of time, increasing the loading frequency induces a shortening in the service time.

### 5.1.3 Loading Ratio Effect

Fatigue behaviour of concrete under different loading ratio $R$ have noticeable differences [128, 129]. For force controlled test, the ratio is given by the maximum and minimum stress in a load cycle as

$$R = S_{\min}/S_{\max}, \tag{5.3}$$

with the sign of stress distinguished by compression and tension. The loading ratio has interaction with the mean stress $\bar{S}$ given by

$$\bar{S} = \frac{S_{\max} + S_{\min}}{2}, \tag{5.4}$$

and the stress amplitude $\Delta S$ evaluated as

$$\Delta S = \frac{S_{\max} - S_{\min}}{2}. \tag{5.5}$$

For example, given $S_{\max}$ and $R > 0$, i.e. for pure tension or compression, increasing $R$ can enlarge the mean stress, which leads to the reduction of fatigue life. An intuitive approach to assess the correlation between $\bar{S}$ and $\Delta S$ is to use the constant-life diagram. The combinations of the two variables introducing equal fatigue life under different loading ratios are demonstrated by contour lines. Due to the lack of experimental data, these contour lines in the early age were assumed to be linear, such as Goodman diagram. However, as argued in [130] there is no physical evidence

supporting the Goodman hypothesis. Indeed, non-linear constant life diagrams are successfully implemented in [131, 132, 133, 134] to predict fatigue life of fibre reinforced composite material. An empirical model [131] for constant life assessment is proposed as

$$\frac{S_f - S_{\min}}{S_{\max}} = \alpha \left( \frac{S_{\max}}{S_f} \right)^{\beta} (\bar{N}_f - 1), \tag{5.6}$$

where $S_f$ is the fracture strength either in monotonic tension or compression, $\alpha, \beta$ and $\gamma$ denote parameters for a certain loading ratio and frequency, and $\bar{N}_f$ is the average of fatigue life. As

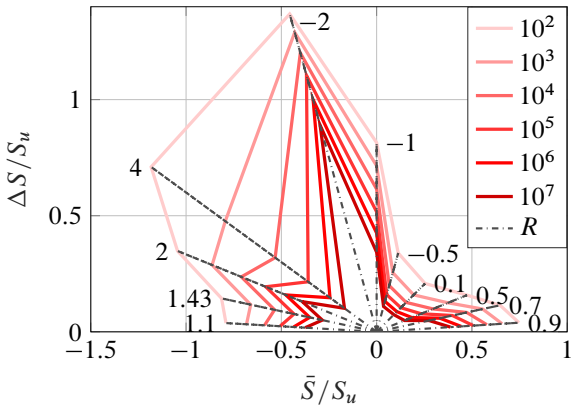


Figure 5.2: A demonstration of constant life diagram modelled by eq. (5.6) using stress amplitude and mean-stress both normalised by ultimate tension strength $S_u$ with the contour lines distinguished by decent colours

illustrated in fig. 5.2 for a required life-cycle the good combinations of $\Delta\sigma$ and $\bar{\sigma}$ have to be within the corresponding contour area. Because of the good readability, constant life diagrams are powerful for fatigue design in terms of the loading ratio effect. However, it is only valid for certain loading frequencies that are available on the diagram. The applicability of instances subjected to random loading is not proven. To improve the quality of this diagram, a very fine discretisation on the load levels with an extensive testing range is required. Meanwhile, the experiment settings have to cover different loading ratios and testing frequencies for better applicability in the real-life.

Alternatively, if a large amount of fatigue data are available, the constant life diagram can be presented as the statistical minimum of the fatigue life. The statistical mean and variance of the S-N relation can be obtained using regression analysis on the fatigue scatters. Instead of the fatigue mean, the lower/upper bonds of the fatigue confidence interval can be plotted on the constant life diagram, to help the design of reliability. For the lack of experimental data, the empirical 95% confidence interval is often used in practice. The minimum life cycles $N_f^{95}$ are calculated through an empirical relation to its average as

$$\log_{10} N_f^{95} = \log_{10} \bar{N}_f - \log_{10} N_\alpha, \tag{5.7}$$

where $N_\alpha$ is a parameter obtained from experiment for a certain loading ratio and frequency.

## 5.2 Fatigue Life Assessment

S-N curve is a standard approach for fatigue life assessment. The horizontal direction represents the fatigue life in cycles $N_f$, and the vertical axis can be the value of maximum or mean of cyclic

stress/strain, more often, load levels marked by $L_s$. Experimental fatigue data are observed with two common characteristics. First, most materials show better resistance under lower loading amplitude than the higher one. Second, fatigue data have strong uncertainties, such that fatigue life is often random for every load levels. Under the assumption of a perfect experimental environment, namely by neglecting the epistemic uncertainties, the uncertain empirical fatigue data is a phenomenological representation of the material heterogeneity. The variation of mechanical performance caused by random microstructure cannot be fully removed as a nature of concrete. Effort on the quality control of the casting process, e.g. hardening time and environment, is possible to reduce the variation. Besides the material uncertainties, the limited number of fatigue data and unpredictable environmental factors, such as random load, increase fatigue life assessment difficulty in reality.

### 5.2.1 Empirical Approaches

**Deterministic models** To reduce the experimental cost, fatigue data are often obtained with sparse load levels, such that only a few samples are available. Empirical approaches aim to provide an analytical expression of the S-N relation based on the regression analysis of the experimental data. The Wöhler equation assumes, the fatigue stress $S$ is correlated to the logarithmic fatigue life $\log_{10} N_f$ by

$$S = \alpha \log_{10} N_f + \beta, \tag{5.8}$$

where $\alpha$ and $\beta$ are the parameters fitted from the fatigue data. This model with a simple equation is very friendly to engineers for the design of fatigue. The major weaknesses are the lack of physical interpretation of the two parameters and the missing capability to describe the effect of loading frequency and the loading ratio. Since the S-N relation is modelled by an algebraic function with almost no thermodynamic constraints, it is difficult to assign a proper physical quantity to both parameters. The combination of the parameters is only valid for a certain fatigue load. Meanwhile, this model cannot capture the correct non-linear S-N relationship when cyclic stress is near fracture strength.

To include the load-ratio effect the model given by eq. (5.8) is modified in [135] as follows,

$$\frac{S_{\max}}{S_f} = 1 - (1 - R)\beta \log_{10} N_f, \tag{5.9}$$

using the assumption, $N = 1$ when $\dfrac{S_{\max}}{S_f} = L_s = 1$. For concrete the value of $\beta$ is obtained as 0.064 under compression [135] and recommend by [15] as 0.0690 for flexural fatigue. This model is however only valid for $R \geq 0$, namely not for reverse loading [136]. To overcome this shortage the following expression is proposed in [137],

$$\alpha \frac{S_{\max}}{S_f} + \beta \frac{S_{\min}}{S_f} = \log_{10} N_f, \tag{5.10}$$

in which $R$ is replaced by the incorporation between $S_{\max}$ and $S_{\min}$. In view of the modelling concept the Suntherland model given by eq. (5.6) is a variation of eq. (5.9) with considerable similarity to eq. (5.10), whose applicability is extended for $R < 0$.

An analytical S-N model concerning frequency effect is first introduced in [138]. As mentioned in section 5.1.2, fatigue life can be influenced by the interaction of the load levels and loading

frequencies. Two different expressions are assigned separately to high and low cycle fatigue of concrete as

$$\begin{cases} \dfrac{S_{\max}}{S_f} = 1 - 0.0662(1 - 0.556R)\log_{10} N_f - 0.0294\log_{10} T, & \text{for HCF,} \\ \dfrac{S_{\max}}{S_f} = 1.2 - 0.2R - 0.133(1 - 0.779R)\log_{10} N_f - 0.053(1 - 0.445R)\log_{10} T, & \text{for LCF,} \end{cases} \tag{5.11}$$

where $T$ denotes the loading period. However, this model is argued in [136] having less evidence about its applicability on reversal load. A further improvement is made by the study [136] in which a loading rate coefficient $C_f$ is introduced into eq. (5.9) as

$$\frac{S_{\max}}{S_f} = C_f \left[1 - (1 - R)\beta \log_{10} N_f\right], \tag{5.12}$$

with

$$C_f = ab^{-\log_{10} f_q} + c, \tag{5.13}$$

where $f_q$ is the applied frequency, $a$, $b$ and $c$ are the material parameters determined by experiments. Under this setting $C_f$ and $f_q$ are positively correlated. The chance of loading frequency can be reflected by the change in fatigue life. The applicability of this model is tested with a wide range of frequencies from $10^{-3}$ Hz to 30 Hz and loading ratio from $-1$ to 0.5.

Although the effects of stress reversal and loading frequencies are included, only the deterministic S-N relationship is considered by the models listed above. There is a common lack of description on the randomness of fatigue data. These models are sufficient for classical fatigue design in which the safety factor is the designing object. Whereas for reliability design, The development of probabilistic models is needed.

**Probabilistic models** The probabilistic models commonly agree that the material property and external loading are subjected to uncertainties. Given the models [15, 19], the general approach is to build a probability function of fatigue failure, which correlates the model parameters to the material and testing parameters.

Statistically, with a certain configuration of fatigue load, the output of a deterministic model is an approximation of the mean of fatigue life, namely $\mathbb{E}\left\{N_f^1, N_f^2, \cdots, N_f^i\right\}$ with $i$ denoting the sequence of data samples. Instead, by considering fatigue life as a random distribution, probabilistic models are able to deliver further stochastic moments, such as the variance $\mathbb{V}\left\{N_f^1, N_f^2, \cdots, N_f^i\right\}$. Random distribution functions, e.g. log-normal, Weibull, are involved in the statistical description of fatigue data. However, as stated in [139] log-normal is not compatible with the material irreversible reaction under fatigue loadings since its hazard function decreases with an increasing number of cycles. Weibull is widely applied on distribution regression of concrete fatigue data obtained under compression [20, 19], three- and four-point flexural test [21, 15, 17]. The common procedure of developing probabilistic models is explained in the following context.

The fist step is to fit the fatigue data by a suitable random distribution. Let the cumulative distribution function (CDF) $F_d(t)$ denote the probability of failure at $t$. The current reliability $R_e(t)$ is given by

$$R_e(t) = 1 - F_d(t). \tag{5.14}$$

Normally, the reliability reduces in time with its expression given by

$$R_e(t) = \exp\left(-\int_0^t h_a(\tau)d\tau\right), \tag{5.15}$$

in which $h_a$ denote the hazard function. The term $h_a(t) \cdot \Delta t$ is a conditional probability that the object fails in the interval $(t, t + \Delta t)$ after surviving in $(0, t)$, namely,

$$h_a(t) \cdot \Delta t \; = \; P\left(\Delta t | R_e(t)\right). \tag{5.16}$$

This gives the expression of $h_a(t)$ as

$$h_a(t) = \lim_{\Delta t \to 0} \frac{R_e(t) - R_e(t + \Delta t)}{\Delta t R_e(t)} = \frac{f_d(t)}{R_e(t)}, \tag{5.17}$$

where $f_d$ is the probability density function (PDF). It is required to have a monotonic increasing $h_a$ which can be suitable to the irreversible accumulation of microscopic damage during fatigue process [15]. As a proof of the conclusion from [139], one may consider a log-normal fatigue life with standard deviation $\sigma$. The corresponding hazard function is written as

$$h_a^{\log}(N_f\sigma) = \frac{1}{N_f\sigma} f_d^N\left(\frac{\ln N_f}{\sigma}\right) / F_d^N\left(\frac{-\ln N_f}{\sigma}\right), \tag{5.18}$$

in which $f_d^N$ and $F_d^N$ denote the PDF and CDF of the standard normal distribution, respectively. The monotonicity of eq. (5.18) cannot be always ensured under the influence of $\sigma$, thus log-normal distribution is avoided by the studies [16, 17, 15, 19, 21]. The PDF and CDF of the two parameter Weibull distribution can be expressed as

$$f_d^{\mathrm{wb}}(x) = \frac{\alpha}{u}\left(\frac{x}{u}\right)^{\alpha-1} \exp\left[-\left(\frac{x}{u}\right)^{\alpha}\right], \tag{5.19}$$

and

$$F_d^{\mathrm{wb}}(x) = 1 - \exp\left[-\left(\frac{x}{u}\right)^{\alpha}\right], \tag{5.20}$$

in which the $u$ is the characteristic life (or scale parameter) and $\alpha$ is the shape parameter. Based on eq. (5.17) the hazard function of Weibull distribution is obtained as

$$h_a^{\mathrm{wb}}(x) = \alpha\left(\frac{x}{u}\right)^{\alpha-1}, \tag{5.21}$$

which is a monotonic increasing function $\forall x \geq 0$. By replacing the variable $x$ with $N_f$ the Weibull distribution is compatible to the expected fatigue behaviour. Generally, there are three methods to determine the parameters $\alpha$ and $u$, the graphical method, the stochastic moment method and the maximum likelihood method.

*Graphical method* Based on eq. (5.20) the reliability function in terms of fatigue cycles is obtained as

$$R_e(N_f) = 1 - F_d^{\mathrm{wb}}(N_f) = \exp\left[-\left(\frac{N_f}{u}\right)^{\alpha}\right]. \tag{5.22}$$

The logarithmic operation on two sides of the equation above provides

$$\ln R_e = -\left(\frac{N_f}{u}\right)^{\alpha}. \tag{5.23}$$

By repeating the operation on eq. (5.23), one has

$$\ln\left[\ln\left(\frac{1}{R_e}\right)\right] = \alpha \ln N_f - \alpha \ln u, \tag{5.24}$$

which can be represented as a linear function

$$\mathcal{Y} = \alpha\mathcal{X} + \zeta, \tag{5.25}$$

with $\mathcal{Y} = \ln\left[\ln\left(\frac{1}{R_e}\right)\right]$, $\mathcal{X} = \ln N_f$ and $\zeta = -\alpha \ln u$. The distribution parameters can be read from the plot of fatigue data, if a linear trend of $\mathcal{X}$ versus $\mathcal{Y}$ is observable. Once the Weibull parameters are determined, the proposed distribution is an empirical approximation of the fatigue life subjected under the corresponding load. For example the following table 5.2 collects a sequence of fatigue data published in the study [17] for concrete under four-point flexural test. The

Table 5.2: Empirical reliability and failure probability obtained from experimental data

| $i$ | $R_e \approx 1 - \frac{i}{\max(i)+1}$ | $F_d^{\mathrm{wb}} = 1 - R_e$ | $N_f^i$ |
|---|---|---|---|
| 1 | 0.9231 | 0.0769 | 75,668 |
| 2 | 0.8462 | 0.1538 | 96,251 |
| 3 | 0.7692 | 0.2308 | 119,562 |
| 4 | 0.6923 | 0.3077 | 131,198 |
| 5 | 0.6154 | 0.3846 | 150,947 |
| 6 | 0.5385 | 0.4615 | 178,217 |
| 7 | 0.4615 | 0.5385 | 191,326 |
| 8 | 0.3846 | 0.6154 | 211,319 |
| 9 | 0.3077 | 0.6923 | 235,282 |
| 10 | 0.2308 | 0.7692 | 346,603 |
| 11 | 0.1538 | 0.8462 | 394,352 |
| 12 | 0.0769 | 0.9231 | 468,581 |

procedure starts by sorting the fatigue data in an increasing order in terms of $N_f^i$. The reliability is approximated by the empirical survivor function, namely,

$$R_e(i) \approx 1 - \frac{i}{n+1} \tag{5.26}$$

in which $n$ denotes the number of samples. Applying the operations of eqs. (5.22) to (5.25) on $N_f^i$ and $R_e$, one has the result plotted in fig. 5.3. The variables $\mathcal{X}$ and $\mathcal{Y}$ are linearly correlated in the plot, with parameters estimated as $\alpha = 1.78$ and $\zeta = -22.15$. Therefore, the Weibull distribution

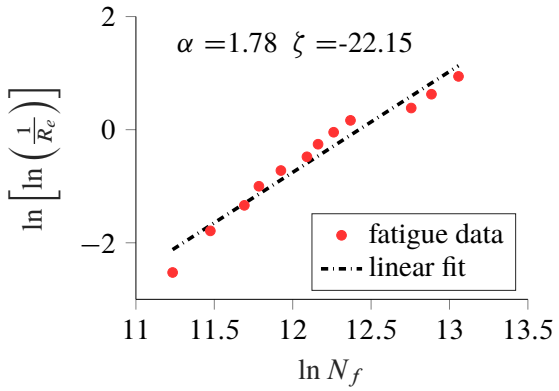


Figure 5.3: Fatigue data provided by Goel and Singh [17] fitted to Weibull distribution based on linear regression of eq. (5.25)

with shape parameter 1.78 and scale parameter $2.48 \times 10^5$ is a good approximation of these fatigue data.

*Stochastic moments method* With this method the Weibull parameters are correlated to the stochastic moments in terms of mean and variance as

$$\mathbb{E}(N_f^i) = u\Gamma\left(1 + \frac{1}{\alpha}\right), \tag{5.27}$$

and

$$\mathbb{V}(N_f^i) = u^2\left[\Gamma\left(1 + \frac{2}{\alpha}\right) - \left(\Gamma\left(1 + \frac{1}{\alpha}\right)\right)^2\right]. \tag{5.28}$$

It is possible to estimate the distribution parameters, once the statistical mean and variance is available. Since both $\mathbb{E}(N_f^i)$ and $\mathbb{V}(N_f^i)$ have dependency on $\alpha$ and $u$, the algebraic equations eq. (5.27) and eq. (5.28) have to be transformed in the following steps to separate the parameters. A dimensionless quantity $C_v$ named as the coefficient of variation, is introduced to determine $\alpha$. It is the measure of variability of Weibull samples given by

$$(C_v)^2 = \frac{\mathbb{V}(N_f^i)}{\mathbb{E}^2(N_f^i)} = \left[\Gamma\left(1 + \frac{2}{\alpha}\right) \cdot \Gamma^{-2}\left(1 + \frac{1}{\alpha}\right)\right] - 1. \tag{5.29}$$

As suggested in [15, 140] eq. (5.29) is equivalent to the reduced form

$$\alpha = (C_v)^{-1.08}. \tag{5.30}$$

for the given concrete material. The data samples shown in table 5.2 have a statistical mean $\mathbb{E}(N_f^i) = 2.16 \times 10^5$ and variance $\mathbb{V}(N_f^i) = (1.24 \times 10^5)^2$ which gives $C_v = 0.57$. By substituting into eq. (5.30) and eq. (5.27) one has $\alpha = 1.82$ and $u = 2.44 \times 10^5$. This result shows considerable similarity to the approximation made by the graphical method. It is mentioned in Oh [15] that the parameter proposed in eq. (5.30) is only applicable for the stress level $L_s = 0.8$. However, the data collected in table 5.2 is from experiment with $L_s = 0.75$ and the parameter approximation is successful. The observation above verifies the applicability of stochastic moments method in parameter analysis of Weibull distribution, particularly, for fatigue data obtained from foreign load levels.

*Maximum likelihood method* This method is suggested by the standardisation organisations in prescriptions, e.g. DIN EN 843 and ASTM C1239 [141]. It seeks for a combination of shape

and scale parameters that maximises the Weibull likelihood function of the experimental data. This method has its advantage in the quality of estimate parameters, because maximum likelihood estimation is statistically unbiased. The Weibull likelihood function is given by the joint density of the data samples as

$$\mathcal{L}(u,\alpha|N_f) = \prod_{i=1}^{n} f_d^{\mathrm{wb}}(N_f^i) = \prod_{i=1}^{n} \frac{\alpha}{u}\left(\frac{N_f^i}{u}\right)^{\alpha-1} \exp\left[-\left(\frac{N_f^i}{u}\right)^{\alpha}\right], \tag{5.31}$$

whose maximum value has to be determined. The logarithmic operation is applied on eq. (5.31) to linearise the problem as

$$\mathcal{L}_{\ln} = \ln \mathcal{L}(u,\alpha|N_f) = n\ln\alpha - n\alpha\ln u - \sum_{i=1}^{n}\left(\frac{N_f^i}{u}\right)^{\alpha} + (\alpha-1)\sum_{i=1}^{n}\ln N_f^i. \tag{5.32}$$

Since the logarithmic transformation has a monotonic increasing trend, the maximum of eq. (5.32) and eq. (5.31) give equivalent result. The gradient of eq. (5.32) with respect to $u$ and $\alpha$ are given by

$$\frac{\partial \mathcal{L}_{\ln}}{\partial u} = -n\alpha\frac{1}{u} + \alpha\sum_{i=1}^{n}\left(N_f^i\right)^{\alpha}\frac{1}{u^{\alpha+1}}, \tag{5.33a}$$

$$\frac{\partial \mathcal{L}_{\ln}}{\partial \alpha} = \frac{n}{\alpha} - n\ln u - \sum_{i=1}^{n}\ln\left(\frac{N_f^i}{u}\right)\exp\left[\alpha\ln\left(\frac{N_f^i}{u}\right)\right] + \sum_{i=1}^{n}\ln N_f^i. \tag{5.33b}$$

The equilibrium points of eqs. (5.33a) and (5.33b) therefore provide the best approximation of the shape and scale parameters, namely $\alpha^*$ and $u^*$. A mathematical transformation on eq. (5.33a) gives

$$u^* = \left[\frac{1}{n}\sum_{i=1}^{n}\left(N_f^i\right)^{\alpha^*}\right]^{\frac{1}{\alpha^*}}. \tag{5.34}$$

Through substituting eq. (5.34) into eq. (5.33b) one has the expression for the solution of $\alpha^*$ as

$$\alpha^* = \left[\frac{\sum_{i=1}^{n}\left(N_f^i\right)^{\alpha^*}\ln N_f^i}{\sum_{i=1}^{n}\left(N_f^i\right)^{\alpha^*}} - \sum_{i=1}^{n}\ln(N_f^i)\right]^{-1}. \tag{5.35}$$

A closed form solution of eq. (5.35) is however not available. Instead it can be solved by iterative schemes, e.g. Newton-Raphson [140]. The shape and scale parameters using the maximum likelihood method are obtained by the Matlab program as $u = 2.46\times10^5$ and $\alpha = 1.96$ for the data in table 5.2.

As a short summary, the three methods presented in the previous context are generally applied in fitting Weibull distribution to experimental fatigue data. The result of parameter estimation is similar with differences in approximation quality. The maximum likelihood method has its complexity in the implementation, whereas it shows better fitting performance than the others. The graphical and stochastic moments methods are intuitive for demonstration purpose, although they are less accurate.

Once the distribution of fatigue data is confirmed, it is necessary to introduce the experimental variables, e.g. stress level, frequency, loading ratios, into the probability of failure, ideally as

$$F_d^{\mathrm{wb}}(N_f; S, f_q, R, \cdots) = 1 - \exp\left[-\left(\frac{N_f}{u(S, f_q, R, \cdots)}\right)^{\alpha(S, f_q, R, \cdots)}\right], \tag{5.36}$$

in which $N_f$ is the primary variable, the secondary variables $u$ and $\alpha$ are written as functions of loading parameters. For an explicit formulations of $\alpha$ and $u$ particular regression analysis regarding to the experimental variables are needed. Since the shape and scale parameter rely on large amount of fatigue data under certain loading condition, which is often unavailable, regression study meets considerable difficulties [20]. In the framework of eq. (5.36) two probabilistic fatigue models are introduced in the following paragraphs.

The probabilistic model [15] is frequently used for four-point bending fatigue prediction. It can be considered as a simplification of eq. (5.36) in which the Weibull scale parameter has only dependency on the stress level. This model is developed on the deterministic assumption given by

$$N_f \left(\frac{S_{\max}}{S_f}\right)^{-m} = C, \tag{5.37}$$

in which $m$ and $C$ are material parameters observed by fitting S-N curves. Since $N_f$ in deterministic model represents the statistical mean of fatigue data, eq. (5.37) is substituted into eq. (5.24) to obtain the following explicit relation,

$$u(S_{\max}) = \exp\left[\frac{-\ln\left[\ln\left(\frac{1}{R_e}\right)\right]}{\alpha}\right] \cdot C \left(\frac{S_{\max}}{S_f}\right)^{-m} \approx \exp\left(\frac{0.5772}{\alpha}\right) \cdot C \left(\frac{S_{\max}}{S_f}\right)^{-m}, \tag{5.38}$$

whereas the shape parameter $\alpha$ is reduced to a material constant. The validity of this model for fatigue design is proven in [140, 16, 17] on concrete material with different volume density (0.5%,1.0% and 1.5%) of steel fibre reinforcement.

Another model [19] is recently developed considering probabilistic influence of loading ratio and frequency. This model is developed with two assumptions. First, the failure strength under fatigue loading $S_{f_d}$ and static strength $S_{f_0}$ are not identical but correlated by the loading rate, written by

$$\frac{S_{f_d}}{S_{f_0}} = \left(\frac{\dot{S}_d}{\dot{S}_0}\right)^{\vartheta}, \tag{5.39}$$

where $\dot{S}_d$ and $\dot{S}_0$ are the time derivative of fatigue and monotonic stress, $\vartheta$ is a material parameter. Second, the probability of failure is a Weibull CDF function mainly depending on the static material property as

$$F_d^{\mathrm{wb}}(S_{f_0}) = 1 - \exp\left[-\left(\frac{S_{f_0} - S_D}{\lambda}\right)^{k}\right], \tag{5.40}$$

where $k$ and $\lambda$ are the shape and scale constant, $S_D$ is the fatigue limit in terms of static stress. The idea is to explore an explicit expression of $S_{f_0}(S_{\max}, f_q, R, N_f)$ which can be substituted into eq. (5.40). The relationship between $S_{f_d}$ and $S_{f_0}$ is obtained as

$$S_{f_d} - S_D = (S_{f_0} - S_D) N_f^{\left[b + c\ln(1+f_q)\right](1-R)}, \tag{5.41}$$

with material constant $b$ and $c$, under the following three limits conditions

$$\begin{cases} \lim\limits_{N\to\infty} S_{f_d} = S_D, \\ \lim\limits_{R\to 1} S_{f_d} = S_{f_0}, \\ \lim\limits_{N\to 1} S_{f_d} = S_{f_0}. \end{cases} \tag{5.42}$$

By inserting eq. (5.41) into eq. (5.40) one has

$$F_d^{\mathrm{wb}}(N_f; S_f, f_q, R, S_D, \lambda, k) = 1 - \exp\left[ -\left( \frac{S_f - S_D}{\lambda N_f^{-\left[b + c\ln(1+f_q)\right](1-R)}} \right)^k \right], \tag{5.43}$$

with $S_f$ derived from eq. (5.39) as

$$S_f = S_{\max}\left( \frac{\dot{S}_0}{2 f_q \Delta S} \right)^{\vartheta} = S_{\max}\left( \frac{\dot{S}_0}{2 f_q S_{\max}(1-R)} \right)^{\vartheta}. \tag{5.44}$$

The model is initially validated by the study [19] on compressive fatigue of concrete. It shows a wide compatibility for different stress ratios $R = [0.1, 0.3]$ and loading frequencies $f_q = [4, 1, \frac{1}{4}, \frac{1}{16}]$ Hz for specimens with/without fibre reinforcement. Further in the work [20] this model is compared to the deterministic models shown by eqs. (5.9), (5.11) and (5.12) particularly on the performance of frequency effect description. The mean produced by the model eq. (5.43) has better agreement than the others while fitting to the fatigue data with constant stress ratio $R = 0.3$. As proven by a recent study [21] this model is feasible to predict four/three points flexural fatigue life of concrete with variations in the reinforcement.

In conclusion, civil engineers can benefit from the empirical fatigue models because they are simple to implement with explicit model formulations. The S-N relationship is obtained straightforwardly, especially with the deterministic empirical models. After decades of development, the model compatibility is improved, such that both the effect of varies frequency and stress ratio can be described. Meanwhile, probabilistic empirical models are beneficial for fatigue design, as the probability of failure is predictable by direct substitution of loading parameters into the model. While fitting experimental fatigue data, the Weibull distributions are frequently used. With an optimised shape and scale parameter, probabilistic models are able to capture fatigue randomness of concrete in compressive and flexural loading situations. Since external load are simplified as input parameters, it is challenging for empirical models to represent the influence of loading history, such as random loading, change of stress range. The solution provided in [15] is to simplify the random load by its historical mean, such that eq. (5.37) becomes to

$$\mathbb{E}(N_f) = \frac{C}{\mathbb{E}\left[(S_{\max}/S_f)^m\right]}, \tag{5.45}$$

and the classical linear Miner's rule is employed to accumulate the fatigue damage under varies of loading levels, namely

$$D = \sum_{L_s=1}^{\max} \left( \frac{N}{C} \mathbb{E}\left[(S_{\max}/S_f)^m\right] \right)_{L_s}. \tag{5.46}$$

Similarly, a generalised nine-parameter empirical model is exposed in the study [18], to capture fatigue damage under any stress history. Although loading frequency is neglected by this model for simplification purpose, the identification of model parameters requires considerable effort both in the experimental and numerical study.

### 5.2.2 Progressive Approaches

Compared to empirical models, the progressive approach is CDM based. Fatigue is treated as a damage process, which accumulates monotonically during cyclic load. Through studying damage evolution in time[1] $D(t)$, fatigue life is the elapsed time when the critical damage value $D_c$ is reached, namely,

$$D(t) = D_c. \tag{5.47}$$

For concrete, $D_c = 0.3$ is employed to indicate the vanish of material continuity. Since eq. (5.47) is not invertible, solution of fatigue life is often implicit. The relationship between $D_c$ and $N_f$ is interpreted in the study [54] with the hypothesis of having linear damage evolution.

Let function $G(S, f_q, R)$ denote the damage evolution rate $\dot{D}$. The current damage is generally calculated by the integration on time as

$$D(t) = D(t_0) + \int_{t_0}^{t} G(S, f_q, R) d\tau, \tag{5.48}$$

where $D(t_0)$ is the initial damage value. Using the transformation from time to the cycle period one has the approximated damage evolution per cycle

$$\frac{\partial D}{\partial N} = \int_{1\text{cycle}} \dot{D} dt = G \cdot T. \tag{5.49}$$

The fatigue life is a quantity satisfies the following equation

$$\int_0^{D_c} \frac{1}{GT} dD = \int_0^{N_f} dN. \tag{5.50}$$

Apparently, eqs. (5.49) and (5.50) are only valid for constant evolution rate. In reality $\dot{D}$ is often time dependent, and the damage process has to be solved numerically. To explain the implementation procedure, an example of reproducing the S-N relation is presented as follows. Moreover, its deterministic performance is compared to the empirical model [15] and the experimental data provided in [17]. Since the empirical models have no geometry dependency, the following comparative study focuses on the discussion of model parameters. An example of Structural analysis is given in chapter 8.

**Example: S-N curve reproduction** Consider a simple brittle damage evolution law [2],

$$\dot{D} = \left\langle \frac{Y - Y_D}{S} \right\rangle^s \langle \dot{Y} \rangle, \tag{5.51}$$

[1] Also possible in cycles, with the transition between time and period, i.e. $t = N \cdot T$.

with material parameter $S$ and $s$. Damage threshold $Y_D$ is given by

$$Y_D = \begin{cases} \frac{1}{2}\varepsilon_D^2 E, \\ \frac{1}{2}\frac{\sigma_D^2}{E(1-D)}, \end{cases} \tag{5.52}$$

for strain or stress constrained test respectively in which $\varepsilon_D$ and $\sigma_D$ denote the corresponding threshold. The angle brackets are subjected to satisfy the KKT conditions given by eq. (3.49). For cyclic loading and unloading the damage evolution is regularised as follows:

- Damage increases only in the loading phase, i.e. $\dot{Y} > 0$ if the material state is over its threshold. Otherwise, the damage remains its last value;
- During the unloading phase, $\dot{Y} \leq 0$, there is no damage evolution.

For an intuitive understanding of these conditions, the interval for effective damage evolution under an arbitrary strain controlled load ($R = 0.1$, $f_q = 1$ Hz, $\varepsilon_{\max} = 0.01$) is presented in fig. 5.4. Special attentions are paid during the time discretisation, to capture the maximum and minimum load. Besides, very small time steps are needed in practice. Normally, enlarging the damage threshold causes the delay of damage growth, because the number of effective time steps involved in the damage evolution is reduced by this action. This can further induce the change of fatigue life. On S-N diagram the fatigue limit corresponds to the damage threshold.

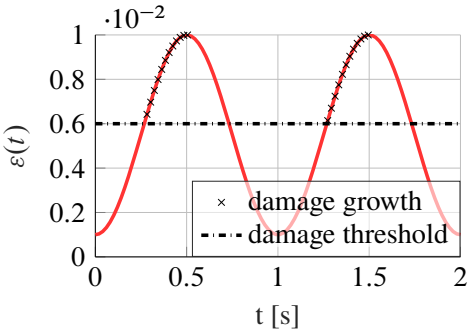


Figure 5.4: Effective damage growth during two cycles with interval above damage threshold marked

According to eq. (3.36), the time derivative of strain energy release rate is obtained as

$$\dot{Y} = E\varepsilon\dot{\varepsilon}. \tag{5.53}$$

Combining eqs. (5.51) and (5.53), an implicit function system for damage evolution is given by

$$\begin{cases} D_{n+1} - D_n = \left\langle \frac{Y_{n+1} - Y_D}{S} \right\rangle^s \left\langle \frac{Y_{n+1} - Y_n}{\Delta t} \right\rangle \cdot \Delta t, \\ Y_{n+1} - Y_n = E\varepsilon_{n+1}(\varepsilon_{n+1} - \varepsilon_n). \end{cases} \tag{5.54}$$

Having the states at $n$, the two unknown variables $D_{n+1}$ and $Y_{n+1}$ can be solved by the Newton-Raphson scheme. If the criteria $D_{n+1} \geq D_c$ is reached, the fatigue life can be converted from the iterated time, namely $n \cdot \Delta t$. Using the loading information from fig. 5.4, an virtual material response within two cycles is obtained via solving eq. (5.54). The results in terms of damage

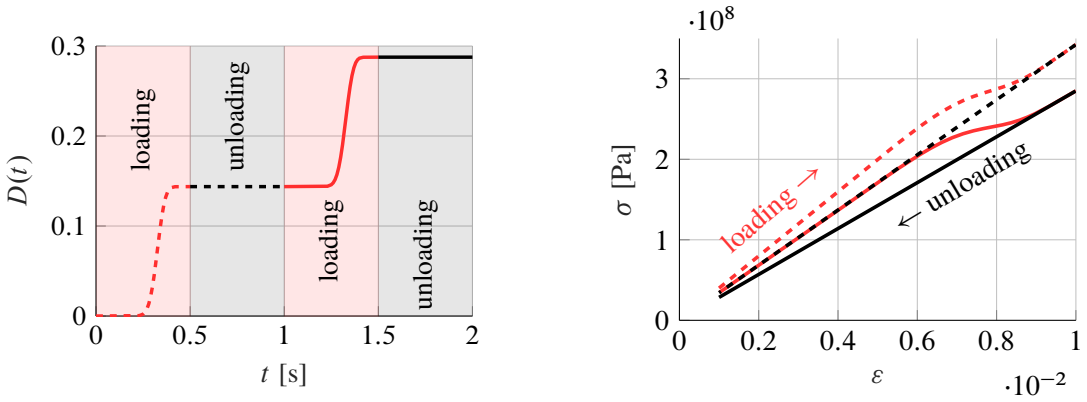


(a) damage evolution (b) strain-stress relationship

Figure 5.5: Material response within two loading cycles computed from eq. (5.54)

evolution and the $\varepsilon - \sigma$ relation are shown in figs. 5.5a and 5.5b respectively. To clearly illustrate the loading-unloading behaviour different colours and line types are used. Comparing to empirical models, these plots show the advantage of using the progressive approach in capturing the detailed material response. Since damage evolution rate is dominated by parameters $s$ and $S$, after calibration it is possible to accurately predict the fatigue life.

The deterministic S-N relation [15] given by eq. (5.37) can be written as

$$\left(\frac{S_{\max}}{S_f}\right)^m = (L_s)^m = \frac{C}{N_f}, \tag{5.55}$$

in which $C = 154.45$ and $m = 24.10$ are suggested in [17] for the concrete material SFRSCC005. The function of parameters, $m$ and $C$, is to control the slope and scale of the S-N curve. For the calibration of $s$, consider the following expression

$$\frac{D_c}{N_f} \approx \frac{\Delta D}{\Delta N} \approx \left\langle \frac{Y_{\max} - Y_D}{S} \right\rangle^s \left\langle \frac{\Delta Y}{\Delta N} \right\rangle, \tag{5.56}$$

as an approximation of eq. (5.54). Since within each cycle $Y_{\max}$ is proportional to $S_{\max}$, eq. (5.56) can be derived as

$$\left(N_f\right)^{-1} \propto \left(S_{\max}\right)^{2s}. \tag{5.57}$$

Comparing to eq. (5.55) one has the approximation $s \approx \frac{1}{2}m$. The influence of parameters $s$ and $S$ on the appearance of reproduced S-N curve are demonstrated in fig. 5.6. The dashed curve is the reference solution given by [17] using the model from Oh [15]. The virtual S-N relations are produced with the damage law in eq. (5.51) using different parameters. In view of figs. 5.6a and 5.6b the slope and scale of the simulated S-N curve can be modified by changing $s$ and $S$ respectively. With calibrated material parameters the S-N relation reproduced by the progressive approach is very close to the empirical result. An error comparison on five different load levels can be seen in table 5.3, where the empirical result is published in [17] using eq. (5.37), and the progressive result is reproduced using eq. (5.51) with $s = 12.05$ and $S = 4.87 \times 10^3$. At each loading level the absolute error of the two approaches is considerably small.

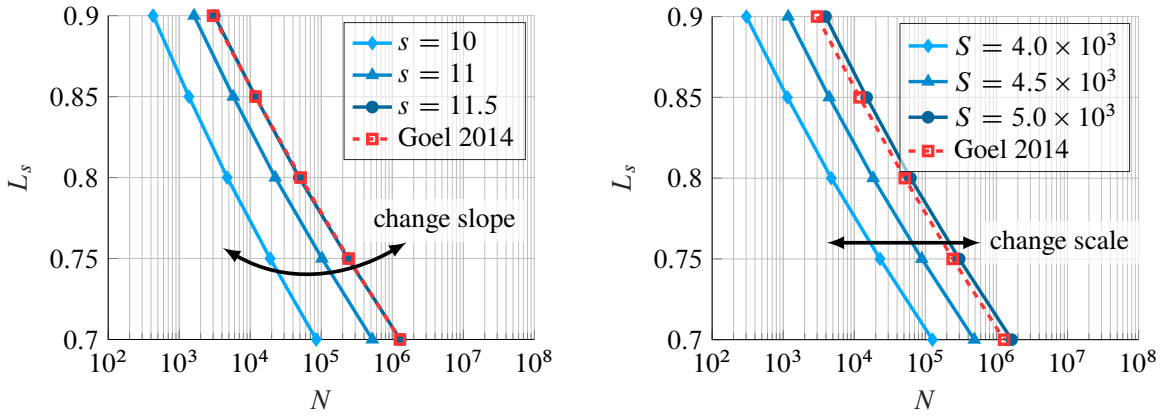


(a) influence of $s$

(b) influence of $S$

Figure 5.6: Appearance of reproduced S-N diagram by changing damage parameters

Table 5.3: Error comparison of simulated fatigue life at five different load levels using empirical and progressive modelling approach

| $L_s : (\frac{S_{\max}}{S_f})$ | 0.9 | 0.85 | 0.8 | 0.75 | 0.7 |
|---|---|---|---|---|---|
| Empirical | 2993 | 11869 | 51162 | 242351 | 1278082 |
| Progressive | 2993 | 11869 | 51163 | 242351 | 1278080 |
| error | 0 | 0 | $1.95\times10^{-5}$ | 0 | $1.56\times10^{-6}$ |

**Example: frequency and mean-stress effect simulation** Progressive approaches rely on the numerical solution of damage evolution, which means fatigue characteristics such as the frequency dependency, mean-stress effect can be generated by a proper modelling of the damage evolution law. Consider the following damage evolution rate,

$$\dot{D} = \left\langle \frac{Y - Y_D}{S} \right\rangle^{s} \langle \dot{Y} \rangle^{s_1} . \tag{5.58}$$

which is identical to eq. (5.51) if parameter $s_1 = 1$. For the case $s_1 \neq 1$ the incremental form of eq. (5.58) given by

$$\frac{D_{n+1} - D_n}{\Delta t} = \left\langle \frac{Y_{n+1} - Y_D}{S} \right\rangle^{s} \left\langle \frac{Y_{n+1} - Y_n}{\Delta t} \right\rangle^{s_1} , \tag{5.59}$$

which has dependency on $\Delta t$, namely, for a fixed number of discretization per loading cycle damage evolution is frequency dependent. Since $\Delta t$ is often much smaller than 1s, changing $s_1$ leads to increase/reduce of damage evolution rate. Comparing to $\dot{D}$ at $s_1 = 1$ an assumption can be made as follows:

$$\begin{cases} \dot{D}(s_1) > \dot{D}(s_1 = 1) & \text{if } s_1 > 1, \\ \dot{D}(s_1) < \dot{D}(s_1 = 1) & \text{if } s_1 < 1. \end{cases} \tag{5.60}$$

By changing the parameter, $s_1$, the frequency effect in term of fatigue life can be observed on the virtual S-N diagram (see fig. 5.8). In this figure the S-N relation at four different frequencies are

evaluated by $s_1 = 0.7$ and $s_1 = 1.3$ respectively. Taking the other parameters identical to eq. (5.51), the simulation result of eq. (5.58) shows that fatigue life can be extended via increasing the loading frequency. This outcome agrees with the assumption made in eq. (5.60), that increasing $s_1$ leads to the rise of damage evolution rate, and the influence at a high loading level is significant.

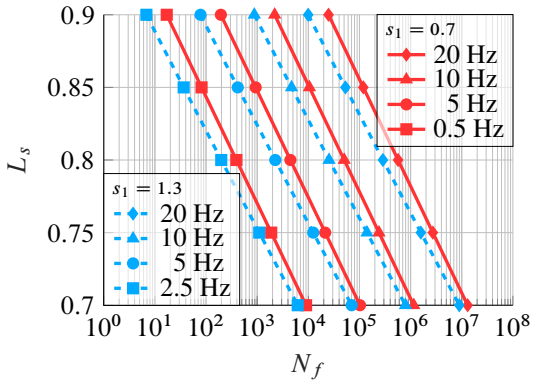


Figure 5.7: General frequency effect generated by two samples of $s_1$ in cooperating with uncalibrated damage parameters

To quantify the influence of $s_1$ on the simulated S-N relation under different loading frequencies, model parameters at 10 Hz are calibrated to meet the reference data at the same configuration given in [17]. In fig. 5.8a fatigue life at 20 Hz is slightly increased by 1.5 times comparing to 10 Hz. After changing frequency to 0.1 Hz, $N_f$ can be reduced intensively up to 5 times. This graphical representation is consistent with the experimental observation reviewed in section 5.1.2 about the loading frequency effect of concrete material. On the contrary, for the simulation $s = 1.3$ (see fig. 5.8b) it appears that reducing the loading frequency can extend the fatigue life. This conflicts with the fatigue behaviour of brittle material in the general sense. Thus, the frequency effect modelled by $s_1 < 1$ is considered. Indeed, a good approximation of $s_1$ depends on a large amount of experimental data from different frequencies. Since $s_1$ has interaction with other damage parameters, any trial of $s_1$ leads to a new calibration of $S$ and $s$. This example also shows that the progressive approach can potentially capture the frequency effect of fatigue damage.

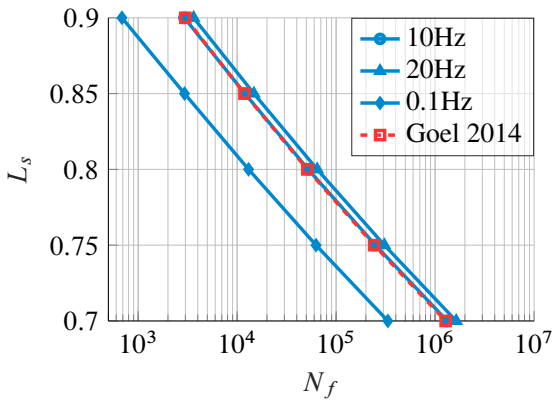


(a) $s_1 = 0.7$: realistic

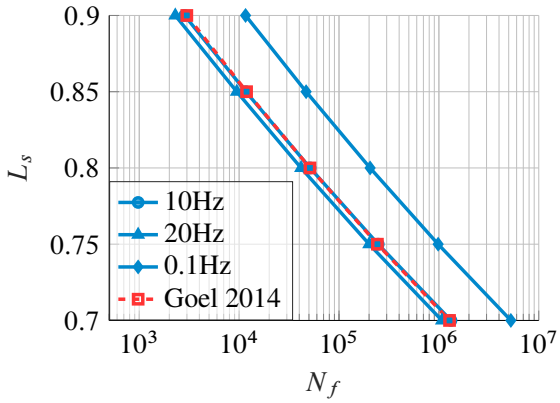


(b) $s_1 = 1.3$: unrealistic

Figure 5.8: Frequency effect modelled by damage evolution with different $s_1$ after parameter calibration

To reproduce the mean-stress effect, different loading ratios are tested using model eq. (5.58) with $s_1 = 0.7$ and $S, s$ calibrated with reference data at 10 Hz and $R = 0.1$. S-N curves for $R$ from $-1$ to 0.8 are demonstrated in fig. 5.9a. The curves are very close to each other indicating that the mean-stress effect in this range is minor. Results for a particular load level 0.7 is plotted in fig. 5.9b. For pure compressive test ($R \geq 0$) with fixed $S_{\max}$, increasing $R$ is equivalent to enlarging $S_{\min}$. Thus, fatigue life is reduced when $R$ approaches to 1. The reversed tension-compression simulation with negative loading ratio up to $R = -1$ also show similar interaction between $N_f$ and $R$. Comparing to the pure tension test, fatigue life can be extended under compression. However, $R = -1$ is a special case with which fatigue life is reduced significantly. Since the S-N relation for all $R$ are almost linear in the log-log plot, it is possible to fit $L_s$ and $N_f$ in the following polynomial

$$\ln L_s = p_1 \ln N_f + p_2, \tag{5.61}$$

in which $p_1$ and $p_2$ denote the linear model parameters.

Table 5.4: Parameter fitting of eq. (5.61)

| $R$ | -1.0 | -0.8 | -0.6 | -0.4 | -0.2 | 0.1 | 0.2 | 0.4 | 0.6 | 0.8 |
|---|---|---|---|---|---|---|---|---|---|---|
| $p_1(\cdot - 10^{-2})$ | 4.136 | 4.145 | 4.145 | 4.145 | 4.144 | 4.143 | 4.143 | 4.142 | 4.142 | 4.140 |
| $p_2(\cdot\, 10^{-1})$ | 2.107 | 2.283 | 2.281 | 2.276 | 2.270 | 2.258 | 2.252 | 2.239 | 2.218 | 2.177 |
| $\|\|\varepsilon\|\|(\cdot\, 10^{-4})$ | 8.380 | 5.614 | 5.446 | 5.587 | 5.906 | 6.176 | 6.289 | 6.500 | 6.550 | 7.156 |

Table 5.4 summarises the fitted parameters and the norm of residual for the loading ratios under test. For a target $N_f$ range from $10^3$ to $10^6$ one can obtain the approximated $L_s$ for each loading ratio using eq. (5.61) in view of table 5.4. According to the Goodman diagram demonstrated in fig. 5.2, the quantities in horizontal and vertical directions are transformed as follows,

$$\begin{cases} \bar{S}/S_u := (S_{\max} + S_{\min})/2S_u \to \frac{L_s(1+R)}{2} := \bar{L}_s, \\ \Delta S/S_u := (S_{\max} - S_{\min})/2S_u \to \frac{L_s(1-R)}{2} := \Delta L_s, \end{cases} \tag{5.62}$$

with two new quantities $\bar{L}_s$ and $\Delta L_s$ defined related to the loading level. By this definition, a similar Goodman diagram regarding to the load level is plotted in fig. 5.10. A general conclusion can be made for all the loading ratios under test, that reducing the loading level leads to an extension of fatigue life.

**Jumping-cycle algorithm** The idea of this algorithm is from linearising the damage evolution, with which the computational effort of high-cycle fatigue can be largely reduced [2]. Although damage evolution in long term is generally non-linear, for a shorter period in HCF damage evolution is often steady, and can be approximated by a linear function. With this assumption the cyclic damage increment, namely $\Delta D/\Delta N$, is treated as a constant for certain cycles $\Delta N^c$. This improves the computational efficiency, that material reaction within these cycles can be extrapolated, rather than computed at each time steps. Due to this extrapolation procedure, the name "jumping-cycle" is given to this algorithm. Often two basic quantities shall be determined by this algorithm, i.e. $\Delta D/\Delta N$

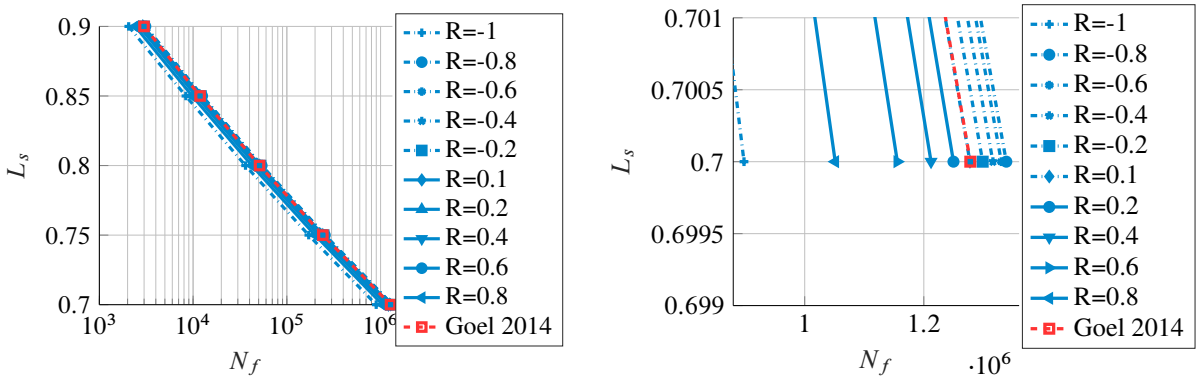


(a) $L_s$ range from 0.7 to 0.9

(b) zoom in at $L_s = 0.7$

Figure 5.9: Simulated fatigue life under different loading ratio with closure parameter $h = 0.2$

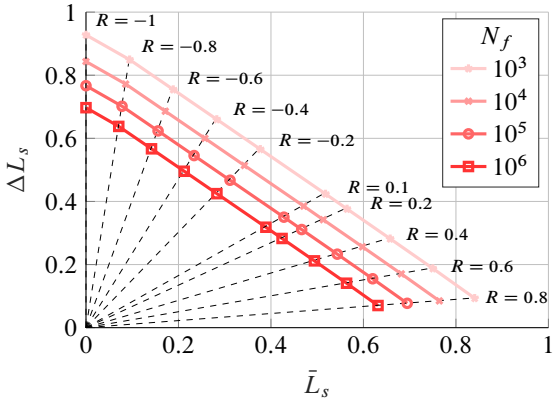


Figure 5.10: A similar Goodman diagram obtained based on fig. 5.9a

and $\Delta N^c$. According to eq. (5.49), damage increments per cycle can be obtained by accumulating its evolution at each time steps, namely

$$\frac{\Delta D}{\Delta N} \approx \sum_{i=1}^{n} \dot{D}\delta t_i, \tag{5.63}$$

where $n$ is the number of time steps per cycle. The number of cycles under extrapolation is calculated using the material parameter $D_{\max}$ as

$$\frac{D_{\max}}{\kappa} = \Delta N^c \cdot \frac{\Delta D}{\Delta N}, \tag{5.64}$$

in which $\kappa$ determines the number of divisions of the whole damage process from zero to its maximum value. For simplicity $D_{\max}$ is set to be identical to the critical damage value $D_c$. After extrapolating $\Delta N^c$ cycles, $\Delta D/\Delta N$ needs to be updated at the beginning of the next division. Generalised to $j$-th division, eq. (5.64) is rewritten as

$$\frac{D_{\max}}{\kappa} = \Delta N_j^c \cdot \left(\frac{\Delta D}{\Delta N}\right)_j, \text{ with } 1 \leq j \leq \kappa. \tag{5.65}$$

Indeed, the initial damage value in the iteration given by eq. (5.54) is set as $D_{\max}/\kappa$ at the beginning of each division. When the maximum damage value is reached, fatigue life is obtained by the

summation, i.e.

$$N_f = \sum_{j=1}^{\kappa} \Delta N_j^c. \tag{5.66}$$

A schematic demonstration of the jumping-cycle algorithm in two example divisions can be seen in fig. 5.11a in which only the first cycle of full computation is needed for each division. Since the computational cost of numerical extrapolation is almost negligible, the total time consumption of HCF simulation can be comparable with finishing $\kappa$ cycles of full computation. The error of fatigue life and the cost of CPU time are introduced as

$$\epsilon_{N_f}^{\kappa,\hat{\kappa}} = \frac{\left\| N_f^{\kappa} - N_f^{\hat{\kappa}} \right\|}{N_f^{\hat{\kappa}}}, \tag{5.67}$$

and

$$t_{\mathrm{CPU}}^{\kappa,\hat{\kappa}} = \frac{t_{\mathrm{CPU}}^{\kappa}}{t_{\mathrm{CPU}}^{\hat{\kappa}}}, \tag{5.68}$$

in which the quantities with a superscript $\hat{\kappa}(\hat{\kappa} \geq \kappa)$ are the references.

Taking again the benchmark problem, i.e. to reproduce the S-N curve in [17] using damage law given by eq. (5.51). Considering $\hat{\kappa} = 220$ the relative cost of $\kappa = 200$ is approximately 4 times higher than the case with $\kappa = 50$ (see fig. 5.11b). The accuracy can also be improved while increasing $\kappa$, with frequently updated damage increments. Since the convergence of error and the growth of cost have different speed, an optimised $\kappa$ is desired to balance the error and cost. An example of $\kappa = 45$ can be given by the cross of the two curves.

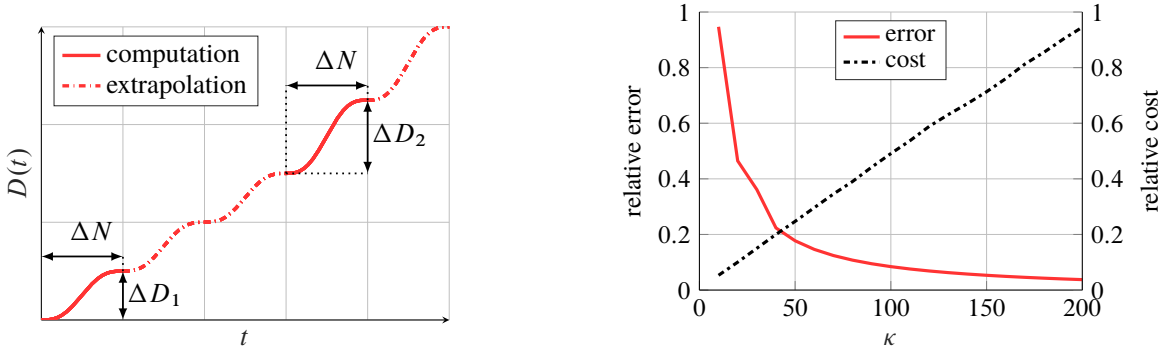


(a) schematic representation

(b) computational error/cost in normalised form

Figure 5.11: Procedure and performance of first order cycle-jumping algorithm

**Second order jumping-cycle algorithm** To improve the accuracy jumping-cycle algorithms based on the second-order extrapolation can be seen in other works [142, 11]. Using Taylor series a quadratic approximation of damage evolution becomes to

$$\frac{D_{\max}}{\kappa} = \Delta N_j^c \cdot \left(\frac{\partial D}{\partial N}\right)_j + \frac{1}{2}\left(\Delta N_j^c\right)^2 \cdot \left(\frac{\partial^2 D}{\partial N^2}\right)_j, \tag{5.69}$$

in which $\frac{\partial D}{\partial N}$ and $\frac{\partial^2 D}{\partial N^2}$ are the first and second order derivative of damage with respect to the cycle. To obtain the two quantities damage increments $\Delta D_{c1}$ and $\Delta D_{c2}$ in two continues cycles $c1$ and $c2$ have to be fully computed, namely

$$\frac{\partial D}{\partial N} = \frac{\Delta D_{c1} + \Delta D_{c2}}{2\Delta N}, \tag{5.70}$$

and

$$\frac{\partial^2 D}{\partial N^2} \approx \frac{\Delta D_{c1} - \Delta D_{c2}}{(\Delta N)^2}. \tag{5.71}$$

The value of $\Delta N_j^c$ is thus obtained by solving the non-linear problem given by eq. (5.69). In fig. 5.12 different algorithms are compared in terms of error and computational cost. The results are normalised by the reference solution with $\hat{\kappa} = 400$ using the second-order extrapolation. Comparing to the first-order method, the second-order algorithm has doubled the cost, whereas the error of fatigue life can be reduced up to 10 times. It means the second-order algorithm requires fewer "jumps" and is able to reproduce more accurate fatigue data. This observation agrees with the conclusion from the previous studies [142, 11] that the second-order jumping algorithm is suitable in fatigue damage computation.

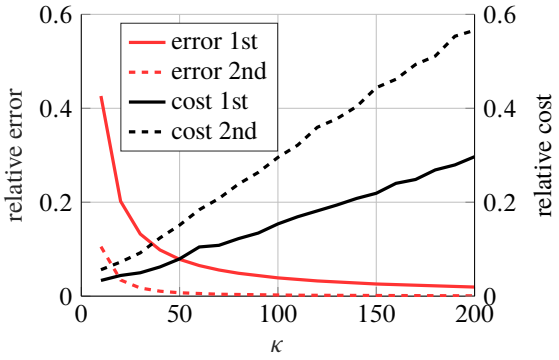


Figure 5.12: Comparison of jumping-cycle performance using first and second order extrapolation

To summarise this chapter, in the first section, fatigue characteristics of brittle material are reviewed, such as frequency and mean-stress effect. Standard testing approaches of fatigue strength under compression, tension and flexural load are also introduced. The second section aims to explain the methods in fatigue life assessment, i.e. empirical and progressive approaches. The empirical methods focus on proposing analytical S-N relations with less attention to the detailed material mechanical reactions. With sophisticated algebraic expressions, empirical models are able to simulate fatigue data, including frequency and loading-ratio effect. Due to the lack of fatigue data, often deterministic S-N relationships are proposed in the early research. Recently improved stochastic empirical models can provide fatigue data, including probabilistic descriptions. Compared to empirical approaches, the progressive approach is CDM based, and the fatigue life is computed from the damage evolution. This method has considerable flexibility to simulate the frequency and mean-stress effect by modelling the progressive damage evolution. The jumping-cycle algorithm is introduced to compute the HCF problem efficiently. Compared to the first-order algorithm, the second-order extrapolation can improve the balance between error and computational effort on fatigue computation. The possibility of reproducing fatigue scatters by modelling the random damage evolution is introduced in the next chapter.

# Chapter 6

# Innovative Phenomenological Stochastic Damage Evolution

Based on the classical works [23, 24, 25], an innovative stochastic damage model for quasi-brittle material is introduced in this chapter. The concept from the literature of modifying deterministic damage evolution as a stochastic differential equation is kept. Special effort is paid on defining proper random distributions. The goal is to solve the common issues in previous studies, such as negative damage increment, conflicts with experimental results.

## 6.1 Modelling Concept

This innovative stochastic damage evolution model is developed within the framework of CDM. The goal is to interpret the phenomenon of the uncertain material stiffness reduction instead of the microstructural heterogeneity. The core of this concept is to extend the mathematical definition of the damage variable as a projection on the time, Euclidean and probability space, namely,

$$\tilde{D}(t, x, \xi_t), \quad \tilde{D} \in \mathcal{T} \times \mathcal{R}^d \times \Omega, \tag{6.1}$$

where $t \in \mathcal{T}$ denote the variable in time, $x \in \mathcal{R}^d$ is the coordinate in n-dimensional Euclidean space and $\xi_t \in \Omega$ is the random variable in the probability space generated at $t$. To maintain the macroscopic continuity, $\tilde{D}$ has to fulfil the requirement

$$0 \leq \tilde{D} \leq D_c. \tag{6.2}$$

For the purpose of simplicity, only isotropic damage is considered by this model. Meanwhile, except for the damage variable, all the other internal variables in CDM remain identical with their original definitions.

Following the assumption of material continuity, the increment of stochastic damage evolution in $\delta t$ can be obtained as

$$d\,\tilde{D} = d\,\tilde{D}(t, x, \xi_t), \quad d\,\tilde{D} \geq 0. \tag{6.3}$$

The expression of $d\,\tilde{D}$ is thus a stochastic differential equation, namely

$$d\,\tilde{D} = g(t, x)dt + h(t, x)d\mathbb{W}_t, \quad d\,\tilde{D} \geq 0 \tag{6.4}$$

in which $g$ and $h$ denote the drift and diffusion of stochastic damage increment respectively. The variable $d\mathbb{W}_t$ is a special stochastic increment, on which further discussion can be seen in section 6.1.2. Comparing to the standard Wiener increment, the only difference is the random number distribution. The time integral on eq. (6.4) gives the stochastic damage evolution as

$$\tilde{D}(t,x,\theta) = D_0(x) + \int_0^t g(s,x)\,ds + \int_0^t h(s,x)\,d\mathbb{W}_s, \tag{6.5}$$

where $D_0(x)$ is the initial damage value at location $x$. The second integral is kept in the Ito way, given by

$$\int_0^t h(s,x)\,d\mathbb{W}_s = \lim_{\Delta t\to 0}\sum_{s=0}^{t} h(s-\Delta t,x)(\mathbb{W}_s - \mathbb{W}_{s-\Delta t}). \tag{6.6}$$

The statistical mean and variance of $\tilde{D}(t,x,\xi_t)$ shall be obtained numerically as

$$\begin{aligned}\mathbb{E}[\tilde{D}(t,x,\theta)] &= \mathbb{E}\left[D_0(x) + \int_0^t g(s,x)\,ds + \int_0^t h(s,x)\,d\mathbb{W}_s\right]\\ &= D_0(x) + \int_0^t g(s,x)\,ds + \mathbb{E}\left[\int_0^t h(s,x)\,d\mathbb{W}_s\right]\\ &= D_t(x) + \mathbb{E}\left[\xi_t\right]\int_0^t h(s,x)\frac{1}{2\sqrt{t}}ds,\end{aligned} \tag{6.7}$$

and

$$\mathbb{V}[\tilde{D}(t,x,\theta)] = \mathbb{V}\left[\int_0^t h(s,x)\,d\mathbb{W}_s\right] = \mathbb{V}[\xi_t]\ \cdot t \cdot \int_0^t h(s,x)ds. \tag{6.8}$$

A demonstration of stochastic damage evolution versus the deterministic one can be seen in fig. 6.1. The uncertain fatigue damage evolution is interpreted as random process realisations.

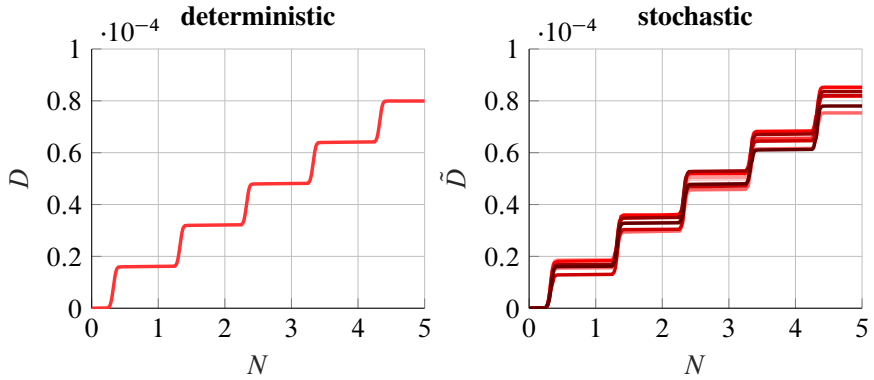


Figure 6.1: Schematic illustration of deterministic and stochastic damage evolution for 5 loading cycles

### 6.1.1 Drift and Diffusion of Stochastic Damage Model

According to eq. (2.11) the drift term in material damage modelling represents the instantaneous change on the mean of damage growing speed, namely

$$g(t,x,\tilde{D}(t)) = \lim_{\Delta t\to 0}\frac{1}{\Delta t}\mathbb{E}\Big[\tilde{D}\,(t+\Delta t,x,\xi_t)-\tilde{D}\,(t,x,\xi_t)\,|\tilde{D}\,(t,x,\xi_t)\Big]. \tag{6.9}$$

It has to be identical with the deterministic evolution rate [23]. In contrast, the diffusion term which governs the intensity of random fluctuations in the material damaging process is defined as

$$h(t,x,\tilde{D}(t)) = \lim_{\Delta t\to 0}\frac{1}{\Delta t}\mathbb{E}\Big[\big(\tilde{D}\,(t+\Delta t,x,\xi_t)-\tilde{D}\,(t,x,\xi_t)\big)^2\,|\tilde{D}\,(t,x,\xi_t)\Big]. \tag{6.10}$$

The exact expression of the diffusion term can vary depending on the modelling purpose. It can be directly proportional to the drift term, e.g. $h=\gamma g$, with which eq. (6.5) becomes to

$$d\,\tilde{D} = g(t,x)(dt+\gamma d\mathbb{W}). \tag{6.11}$$

Alternatively, it can be a constant $\zeta$ to demonstrate the noise in the measure of damage, namely

$$d\,\tilde{D} = g(t,x)dt+\zeta d\mathbb{W}. \tag{6.12}$$

Meanwhile, a polynomial superposition can be applied to mix the above two types of diffusion as

$$d\,\tilde{D} = g(t,x)dt+[(1-\rho)g(t,x)+\rho]\,d\mathbb{W}. \tag{6.13}$$

where $\rho$ is a constant to tune their combination.

### 6.1.2 Stochastic Increment for Damage Modelling

The Wiener increment $d\,W$ based on the standard Gaussian random noise $\xi_t^{\mathrm{N}}\sim N(0,1)$ is mostly used to formulate the stochastic differential equations. According to the property of Gaussian distribution, $d\,W$ can be any real numbers, i.e.

$$-\infty\le d\,W\le+\infty,\quad \xi_t^{\mathrm{N}}\in\mathbb{R}. \tag{6.14}$$

By its thermodynamic constraints, $d\,\tilde{D}$ has to be non-negative for traditional materials. It can be thermodynamically inconsistent to apply classical Wiener increment in the damage evolution process. One practical solution is to modify the Gaussian random number to satisfy the condition $d\,\tilde{D}\ge 0$. Depending on the drift and diffusion, truncated Gaussian distribution and others, e.g. Weibull, log-normal, can be applied. A stochastic increment, which is not evaluated using the standard Gaussian noise, is denoted as $d\,\mathbb{W}$ given by

$$d\,\mathbb{W}_t = \sqrt{\delta t}\,\xi_t. \tag{6.15}$$

Combine eq. (6.15) with the general case of stochastic damage increment in eq. (6.4). The lower bound for the random noise is obtained as

$$\xi_t \ge -\frac{g\sqrt{\delta t}}{h}. \tag{6.16}$$

To maintain the mean of stochastic damage evolution to be identical to the deterministic growth, the expectation of random noise have to be zero, i.e.

$$\mathbb{E}[\tilde{D}(t,x,\xi_t)] = D_t(x) \Leftrightarrow \mathbb{E}[\xi_t] = 0. \tag{6.17}$$

During the random noise generation, the two conditions given by eqs. (6.16) and (6.17) shall be fulfilled. The procedure is as follows:

1. Generate positive random numbers $\xi_t^+$ from e.g. Weibull, log-normal with the expectation given by
$$\mathbb{E}\left[\xi_t^+\right] = +\frac{g\sqrt{\delta t}}{h}. \tag{6.18}$$
2. Obtain zero-mean $\xi_t$ by shifting $\xi_t^+$ with following expression
$$\xi_t = \xi_t^+ - \left(+\frac{g\sqrt{\delta t}}{h}\right). \tag{6.19}$$

Alternatively, if a non-negative random distribution $\mathcal{N}^+(\mu, \nu^2)$ exists for all the random numbers $\{X \geq 0 | X \sim \mathcal{N}^+\}$ with mean and variance specified as $\mu = 1$ and $\nu^2$, $\xi_t$ can be generated from

$$\xi_t \sim \left(\mathcal{N}^+ - 1\right)\frac{g\sqrt{\delta t}}{h}. \tag{6.20}$$

The variance of $\xi_t$ is a key parameter that strongly influences the probabilistic behaviour of $\tilde{D}$. To fit with experimental data, it is convenient to tune the intensity of damage fluctuation by directly working on $\nu^2$ rather than changing the diffusion. Via the parametric study in the following context, the performance of the stochastic random damage model is exposed.

## 6.2 Parametric Study

In this section, three types of random contribution, i.e. proportional, non-proportional and mixed diffusion, are presented to demonstrate their influences on the damage evolution. The stochastic damage model is implemented on a simplified fatigue problem to understand the role of random variables and other parameters (see section 5.2.2). Higher-dimensional structural analysis can be seen in the next chapter.

### 6.2.1 Proportional Diffusion

With proportional diffusion the intensity of damage fluctuation is correlated to the mean [23, 25]. Hypothesis on this type of diffusion is straightforward, because experimental damage data are less scattered when the value is low [22]. By rewriting eq. (6.11) in the incremental form, one has

$$\Delta\tilde{D} = g(t,x)\Delta t\left(1 + \frac{\gamma\xi_t}{\sqrt{\Delta t}}\right), \tag{6.21}$$

which gives the conditions of $\xi_t$ as

$$\begin{cases} \mathbb{E}\left[\xi_t\right] = 0, \\ \xi_t \geq -\dfrac{\sqrt{\Delta t}}{\gamma}. \end{cases} \tag{6.22}$$

According to eq. (6.20), for the case of proportional diffusion $\xi_t$ has to be generated from

$$\xi_t \sim \left(\mathcal{N}^+ - 1\right) \frac{\sqrt{\Delta t}}{\gamma}, \tag{6.23}$$

with which a conclusion on eq. (6.21) can be made as

$$\Delta \tilde{D} \sim \Delta D \cdot \mathcal{N}^+. \tag{6.24}$$

Unlike the work [24] in which the standard Gaussian distribution is employed, a "filtering-algorithm" is needed to reject the random numbers that cannot fulfil the second condition in eq. (6.22). The expectation on the percentage of acceptable Gaussian random number in the total sampling amount is given by

$$\mathbb{E}(\xi_N\%) = 1 - F_N\left(-\frac{\sqrt{\Delta t}}{\gamma}\right)_{\mu_N, \nu_N^2}, \tag{6.25}$$

in which $F_N$ is the Gaussian cumulative distribution function for mean $\mu_N$ and variance $\nu_N$. The "zero-mean" constraint, however, cannot be guaranteed in this case, as the symmetry of Gaussian distribution is alternated by the filtering process, and $\mathbb{E}[\xi_t]$ is shifted to a positive number. This further causes bias between the mean of stochastic damage evolution and its deterministic law. As demonstrated in fig. 6.2 the statistical mean $\mu(\tilde{D})$ of 1000 example trajectories grows faster than the deterministic damage. To solve this problem, two particular random distributions, i.e. the shifted Weibull and log-normal, are designed, with which eq. (6.22) can be strictly satisfied during the random number generation.

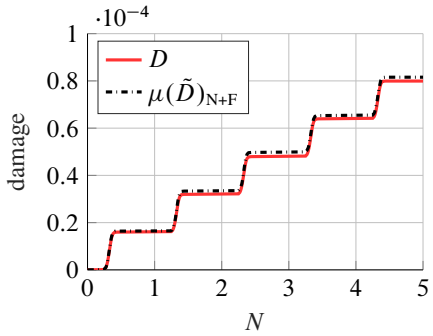


Figure 6.2: Comparison of damage evolution for 5 loading cycles, deterministic vs standard Gaussian with filtering

**Designing process of $\mathcal{N}^+(\mu, \nu^2)$** Theoretically, both Weibull and log-normal are non-negative distributions. The unknown Weibull scale and shape parameters, $u$ and $\alpha$ for a desired mean $\mu$ and variance $\nu^2$ can be obtained by solving the function system,

$$\begin{cases} \mu = u\Gamma\left(1 + \dfrac{1}{\alpha}\right), \\ \nu^2 = u^2\left[\Gamma\left(1 + \dfrac{2}{\alpha}\right) - \left(\Gamma\left(1 + \dfrac{1}{\alpha}\right)\right)^2\right]. \end{cases} \tag{6.26}$$

Similarly, to design a log-normal distribution, its parameters $m_{\log}$ and $v_{\log}^2$ can be solve from

$$\begin{cases} \mu = \exp\left(m_{\log} + v_{\log}^2\right), \\ \nu^2 = \exp\left(2m_{\log} + v_{\log}^2\right)\left(\exp\left(v_{\log}^2\right) - 1\right). \end{cases} \tag{6.27}$$

Taking $\mathcal{N}^+(1,1)$ as example, the Weibull parameters are determined as $u = 1$ and $\alpha = 1$, and for the log-normal distribution with $m_{\log} \approx -0.3466$, $v_{\log}^2 \approx 0.6931$. The probability density function of the above two distributions are plotted in fig. 6.3. By generating damage noise from the two distributions, the statistical mean of 1000 random damage trajectories is nearly identical to the deterministic one (see fig. 6.4). The damage uncertainty is represented by the measure of its standard deviation shown in fig. 6.5. The result produced by Weibull and log-normal noise are almost identical, that the damage standard deviation is enlarged sub-linearly by time. This observation agrees to the general behaviour of Wiener process, i.e. $\sqrt{\mathbb{V}[dW]} = \sqrt{dt}$.

While increasing the desired variance of $\mathcal{N}^+$ from 1 to 10, there is a significant difference in the quality between the generated Weibull and log-normal random numbers. To demonstrate this, let the quality of the random number generation to be measured by the relative error $\epsilon_{(\bullet)}$. The relative error between the quantity $(\bullet)$ and its reference is computed by

$$\epsilon_{(\bullet)} = \left\| \frac{(\bullet) - \text{ref.}}{\text{ref.}} \right\|. \tag{6.28}$$

After solving the Weibull and log-normal parameters for the desired variance $\nu^2 = 10$, the positive random variables are obtained algebraically from the standard Gaussian noise as

$$\begin{cases} \xi_{\log} = \exp\left(m_{\log} + v_{\log}\xi_N\right) & \text{for log-normal,} \\ \xi_{\text{Wb}} = u\left(-\log\left(1 - F_N(\xi_N)\right)\right)^{\frac{1}{\alpha}} & \text{for Weibull.} \end{cases} \tag{6.29}$$

Theoretically, for the same group of $\xi_N$, the Weibull and log-normal random numbers can be generated with identical mean and variance. However, for a considerable large amount of samples, e.g. 100 seeds with $10^6$ random numbers each, the variance of log-normal random number has large difference to its designing target, namely $\mathcal{N}^+(1,10)$ (see fig. 6.6b). This phenomenon is slightly visible for smaller variance $\mathcal{N}^+(1,1)$, though $\epsilon_\nu^{\log}$ is generally larger than the other plotted quantity. In contrast, the designed mean $\mu = 1$ can be well kept for both Weibull and log-normal random numbers without being dramatically influenced by changing the variance. This observation indicates that it is difficult to generate a highly accurate log-normal random number with large variance from standard Gaussian random noise.

**Influence of sampling amount** The number of MC samples is an important factor for the result of random damage evolution, because it influences both the mean and variance. The common agreement is that the statistical mean and variance of random damage trajectories converges by increasing the number of MC realisations [24, 25]. To have a steady convergence plot, the statistical result of damage evolution after 10 cycles from 100 batches with each 16384 trajectories (paths) is

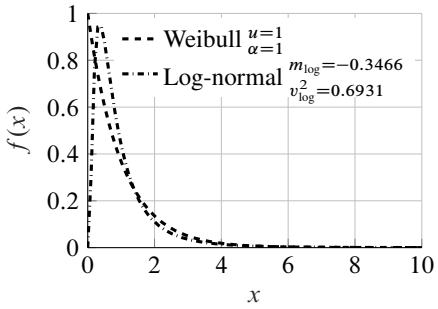


Figure 6.3: Probability density function of the designed Weibull and log-normal distribution with mean $\mu = 1$ and variance $\nu^2 = 1$

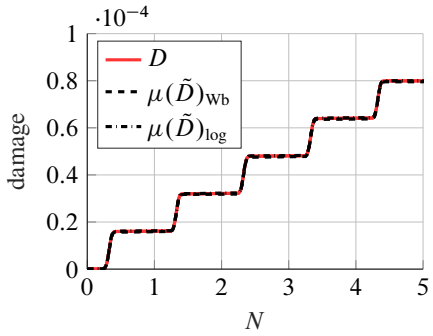


Figure 6.4: Stochastic damage evolution using designed Weibull and log-normal random noise

set as the reference, namely

$$\begin{cases} \dfrac{1}{100}\displaystyle\sum_{\text{batch}=1}^{100} \mu\left(\tilde{D}_{\text{path } 1\to 16384}\right) & \text{ref. mean,} \\ \dfrac{1}{100}\displaystyle\sum_{\text{batch}=1}^{100} \nu\left(\tilde{D}_{\text{path } 1\to 16384}\right) & \text{ref. standard deviation.} \end{cases} \tag{6.30}$$

During the test interval from 128 to 8192 paths, an apparent convergence of both the damage mean and standard deviation using Weibull distribution can be seen in fig. 6.7. The relative error of the statistical mean is near $10^2$ times smaller than the standard deviation. In practices, a reasonable MC sampling amount has to be determined by the actual demand to balance the computational cost and accuracy.

**Influence of jumping-cycle algorithm** The jumping-cycle algorithm strongly influences the stochastic damage evolution since the mean and standard deviation error can be enlarged during the extrapolation process. The benchmark test takes Weibull distribution $\mathcal{N}^+(1,1)$ to generates $10^3$ paths during the damage interval of $[0, 0.1]$ without extrapolation. In comparison, the first and second-order jumping-cycle algorithm is implemented with $\kappa$ varies from 20 to 400. The target is to investigate the applicability of the jumping cycle algorithms on stochastic fatigue damage computation.

A narrow scattered damage band is observable from the benchmark result in fig. 6.8a, whereas both jumping-cycle algorithms introduce large uncertainties. The scatter band of the second-order algorithm is particularly wider than the others (see fig. 6.8b). Meanwhile, around 10% realisations from the second-order algorithm have a significant bias to the benchmark result. This observation

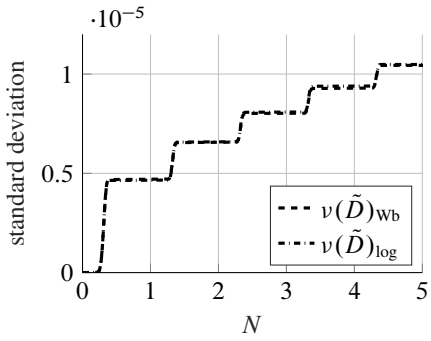


Figure 6.5: Expansion of damage uncertainty using designed Weibull and log-normal random noise

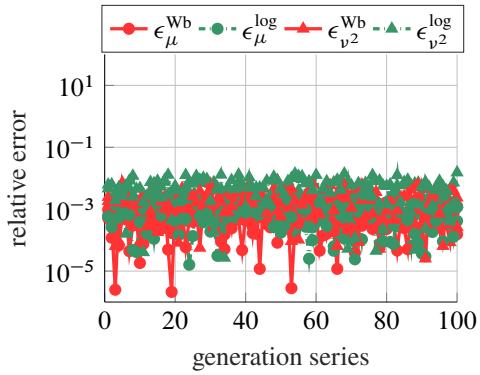


(a) $\mathcal{N}^{+}(1,1)$

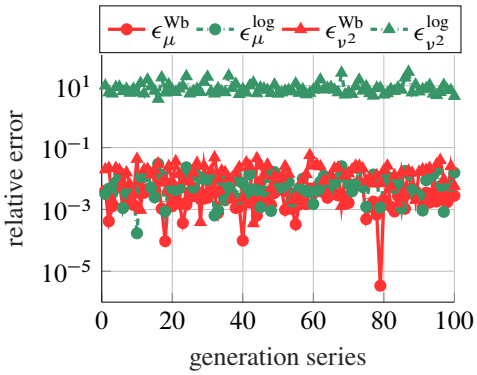


(b) $\mathcal{N}^{+}\left(1,\left(\sqrt{10}\right)^{2}\right)$

Figure 6.6: Quality of non-negative random number generated from Weibull and log-normal distribution

exposes the numerical issue of the high order jumping-cycle algorithm. The solution of second-order extrapolation in eq. (5.69) can be unstable with random damage law. Since the condition, $\Delta D_{c1} \leq \Delta D_{c2}$, cannot be guaranteed for two sequential cyclic increments, the parabola

$$f_j\left(\Delta N_j^c\right) = \frac{1}{2}\left(\Delta N_j^c\right)^2 \cdot \left(\frac{\partial^2 D}{\partial N^2}\right)_j + \Delta N_j^c \cdot \left(\frac{\partial D}{\partial N}\right)_j - \frac{D_{\max}}{\kappa}, \tag{6.31}$$

can be either convex or concave with respect to $\Delta N_j^c$. For the case of concave function, the solution of $\Delta N_j^c$ can be considerable large or even a complex number. It is possible to avoid unreal solution by averaging two sequential damage increments as

$$\Delta \hat{N}_j^c = \left(\frac{D_{\max}}{\kappa}\right) \Big/ \left(\frac{\Delta D_{c1} + \Delta D_{c2}}{2}\right). \tag{6.32}$$

However, it is difficult to set up a proper criteria to filter out the improper $\Delta N_j^c$. Indeed, statistics on the elapsed cycles at the end of damage computation show that the high-order jumping cycle algorithms have advantages to reproduce accurate damage mean. Figure 6.9 illustrates the probability density of $N$ at $\tilde{D}(N) = 0.1$ for three different simulations. The mean obtained by the second-order method is close to the benchmark result, though its variance is large. The influences of $\kappa$ on the statistical results of $N$ are plotted in fig. 6.10 for the interval $\kappa \in [20, 400]$. Compared to the benchmark result, the relative error produced by the first-order method converges distinctively with

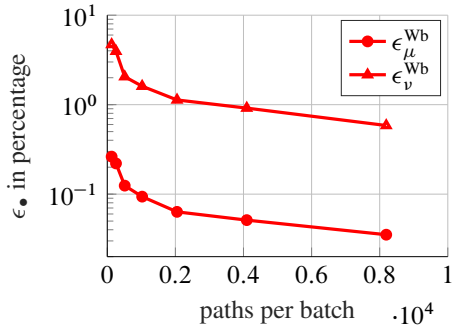


Figure 6.7: Convergence of random damage mean and standard deviation

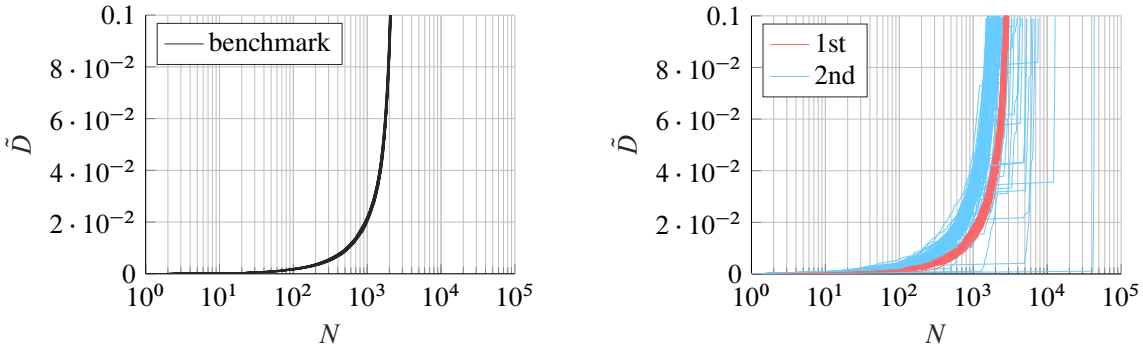


(a) damage scatter benchmark (no jump)

(b) first- and second-order jump ($\kappa = 100$)

Figure 6.8: Stochastic fatigue damage evolution

respect to $\kappa$. In contrast, the second-order algorithm exhibits a convergence problem. Concerning the numerical stability, the classical first-order jumping-cycle algorithm is recommended for random high-cycle fatigue computation.

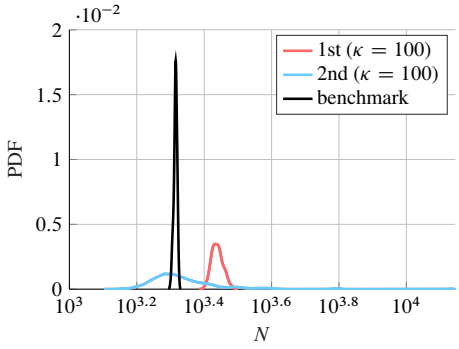


Figure 6.9: Statistics of $N$ given $\tilde{D}(N) = 0.1$

**Reproduction of stochastic S-N relation** In the previous chapter, the S-N curve of concrete material published in [17] can be accurately reproduced using the deterministic damage law. To reach the goal of this study, the proposed model must reproduce the probabilistic S-N relation, fitting both the fatigue mean and variance. As stated in the previous chapter, the fatigue life $N_f$ of reinforced concrete is assumed in [15] to follow the two-parameter Weibull distribution. The shape

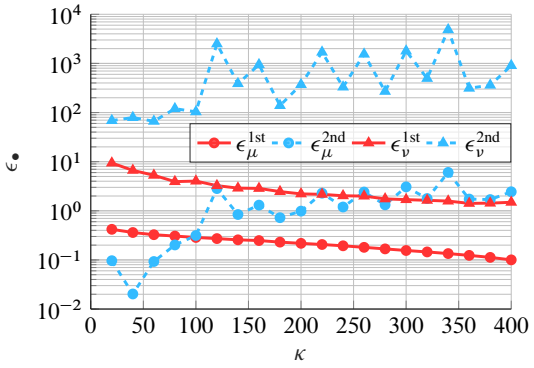


Figure 6.10: Performance of jumping-cycle algorithms with different extrapolation parameters

parameter $\alpha$ is given by

$$\alpha = \sqrt{\frac{\pi^2}{6(\sigma_{\log N})^2}}, \tag{6.33}$$

and the scale parameter (characteristic life) $u$ is defined as

$$u = \exp\left(\frac{0.5772}{\alpha}\right) \cdot \left[C\left(\frac{S_{\max}}{S_f}\right)^{-m}\right]. \tag{6.34}$$

The parameter, $\sigma_{\log N}$, is the estimation of the standard deviation of $\log_{10}(N)$ at a specified loading level, which has the value 0.9448 for SFRSCC005 material. The material parameters $C = 154.45$ and $m = 24.10$ are kept identical to the deterministic model. For different load levels the Weibull parameters can be seen in table 6.1. According to eqs. (5.27) and (5.28) the expectation and standard

Table 6.1: Weibull parameters for five load levels obtained from SFRSCC005 data [17]

| $\alpha$ | $L_s : (\frac{S_{\max}}{S_f})$ | 0.9 | 0.85 | 0.8 | 0.75 | 0.7 |
|---|---|---|---|---|---|---|
| 1.3577 | $u$ | 2741 | 10872 | 46868 | 222010 | 1170810 |

deviation of the fatigue life are approximated by

$$\mu(N) = u\Gamma\left(1 + \frac{1}{\alpha}\right), \tag{6.35}$$

and

$$\nu(N) = \sqrt{u^2\left[\Gamma(1 + \frac{2}{\alpha}) + \Gamma\left(1 + \frac{1}{\alpha}\right)\right]}, \tag{6.36}$$

respectively. The values of $\mu(N)$ and $\nu(N)$ for different load levels are collected in Tab. (6.2), and their correlation is plotted in fig. 6.11. To approach the empirical relation, the positive distribution $\mathcal{N}^+(1, \nu^2)$ and the jumping-cycle parameters must be calibrated carefully.

For proportional diffusion with the Weibull random number $\mathcal{N}^+(1, \nu^2)$, the variance of the damage variable after one full-cycle computation can be roughly described as

$$\mathrm{var}\left[\tilde{D}_{\text{cycle}}^{0\to1}\right] = (\nu \Delta D_c)^2 \, T_c, \tag{6.37}$$

Table 6.2: Expectation and standard deviation of fatigue life for five different load levels using Oh [15] model and Weibull parameters from Goel and Singh [17]

| $L_s : (\frac{S_{\max}}{S_f})$ | 0.9 | 0.85 | 0.8 | 0.75 | 0.7 |
|---|---|---|---|---|---|
| $S_{\max}$ [Pa] | 5.4e6 | 5.1e6 | 4.8e6 | 4.5e6 | 4.2e6 |
| $\mu(N_f)$ | 2993 | 11869 | 51162 | 242351 | 1278082 |
| $\nu(N_f)$ | 2042.33 | 8099.03 | 34912.05 | 165372.84 | 872122.33 |

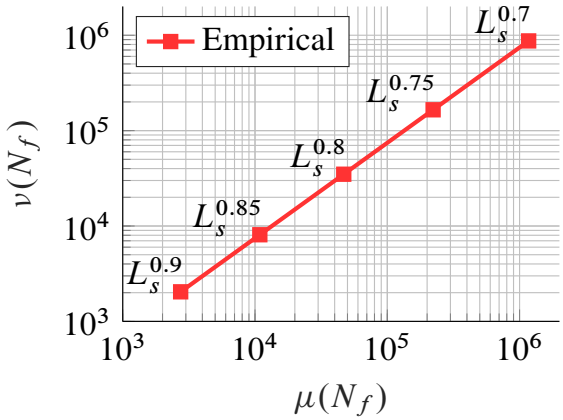


Figure 6.11: Empirical relation between mean and standard deviation of fatigue life

where $\Delta D_c$ is the average damage increment during the period of $T_c$. For very high cycle fatigue, the cyclic increment of damage is almost a constant for 100 cycles. $\nu(\tilde{D})$ has the value $\nu\Delta D_c\sqrt{100T_c}$ if the full-cycle computation is applied in 100 sequential cycles. However, with the jumping cycle algorithm, $\sigma(\tilde{D})$ can reach $100\nu\Delta D_c\sqrt{T_c}$, which is 10 times larger than the previous case. This quantitative analysis provide a general guideline for tuning $\nu$.

Moreover, the jumping factor $\kappa$ significantly influences the fatigue uncertainty. As shown in fig. 6.12 enlarging $\kappa$ leads to a distinctive reduction of the standard deviation of fatigue life. After calibrating the random number and the jumping-cycle parameter, fatigue life computed via stochastic damage evolution law is able to closely fit to the empirical results both in the mean and standard deviation (see Fig. (6.13)). The probability density of the reproduced fatigue life is compared to the experimental data (see fig. 6.14). For each loading levels, their probabilistic behaviour are significantly similar to each other up to the high-cycle regime.

### 6.2.2 Other Types of Diffusion

Equation (6.13) is a general expression of the stochastic damage increment introduced with non-proportional diffusion. If $\rho = 0$ it reduces to the proportional case given by eq. (6.11), whereas if $\rho = 1$ the random damage noise is purely independent from the damage mean, namely identical to eq. (6.12). The numerical study [24] is equivalent to $\rho = 1$ in which the standard Gaussian white noise is implemented without the filtering process. This configuration is acceptable from the perspective of damage measurement, as the measure of damage increment can either be

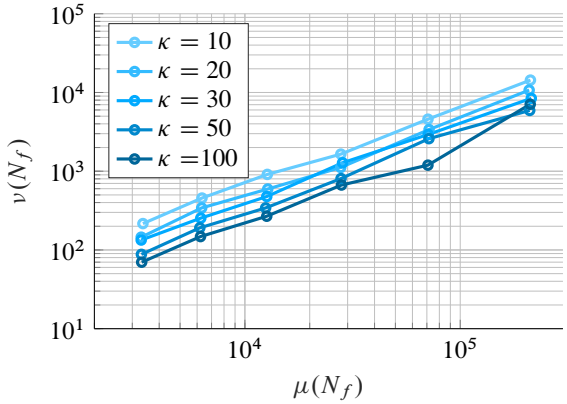


Figure 6.12: Influence of jumping-cycle parameter on the relationship between mean and standard deviation of fatigue life (plotted during calibration trial)

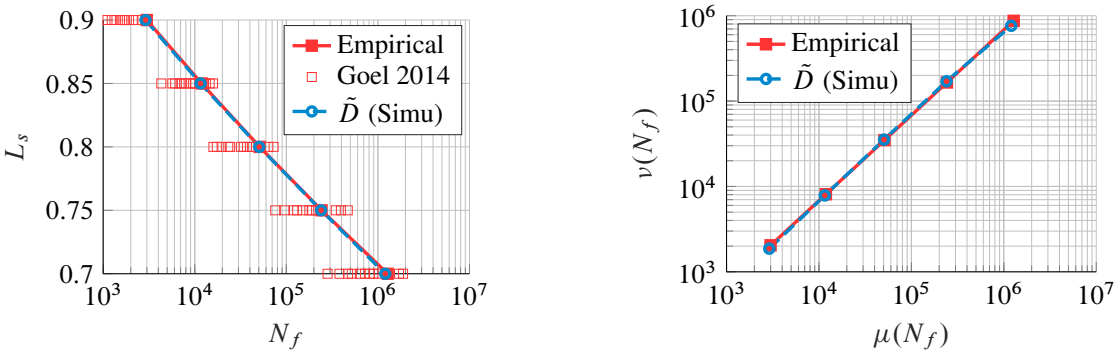


(a) fatigue life in 5 load levels

(b) mean versus standard deviation of fatigue life

Figure 6.13: Reproduction of random fatigue data using stochastic damage law (1D)

positive or negative. Besides, deterministic damage models are developed to generally fit the average value of experimental data, without considering the random behaviour [143]. Towards this specific issue, applying standard Wiener increments is necessary to simulate the noise in damage measure. Numerical investigation using material state uncorrelated white noise is less meaningful to understand the physical mechanism of uncertainty propagation in the damage process. This is because the statistical behaviour of the standard Wiener process is plain with less interpretation in solid mechanics. Due to the lack of data of measurement error, model validation can be very challenging.

Numerically, it is also interesting to see the contribution of the non-proportional diffusion while filtering out the negative damage increments. Take the following equation as an example

$$d\,\tilde{D} = g(t,x)dt + d\mathbb{W}. \tag{6.38}$$

A proper random number has to be generated as

$$\xi_t \sim \left(\mathcal{N}^+(1,\nu^2) - 1\right) g(t,x)\sqrt{\Delta t}, \tag{6.39}$$

to satisfy $\mathbb{E}\left[\tilde{D}(t)\right] = D(t)$ and $d\,\tilde{D} \geq 0$, $\forall t$. Since $g(t,x)$ is time dependent, the distribution of

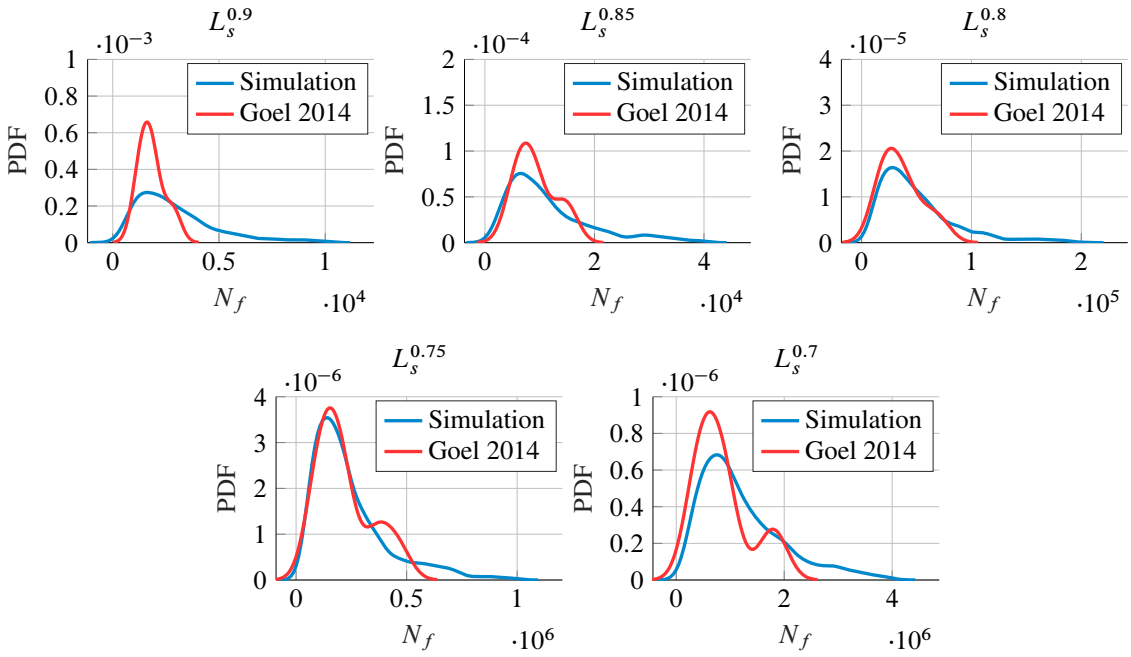


Figure 6.14: Probability density of fatigue life at 5 loading levels

$\xi_t$ varies in time. The standard deviation of $d\tilde{D}$ has an algebraic expression given by

$$\mathbb{S}\left[d\tilde{D}\right] = g\Delta t v = \Delta D v. \tag{6.40}$$

It means the damage uncertainty is very sensitive to the time step size. By tuning $\Delta t$ it is possible to introduce an extra frequency effect besides the deterministic law. A demonstration can be seen in fig. 6.15 that the random damage evolution is boosted dramatically via increasing the loading frequency (see the amplitude of $y$-axle). This kind of frequency effect comes into conflict with experiments, where fatigue life often get extended under higher frequency. Theoretically, the parameter $\rho$ can be calibrated to balance the effect of proportional and non-proportional diffusion. Since the experimental data are difficult to obtain, further investigation on $\rho$ is omitted.

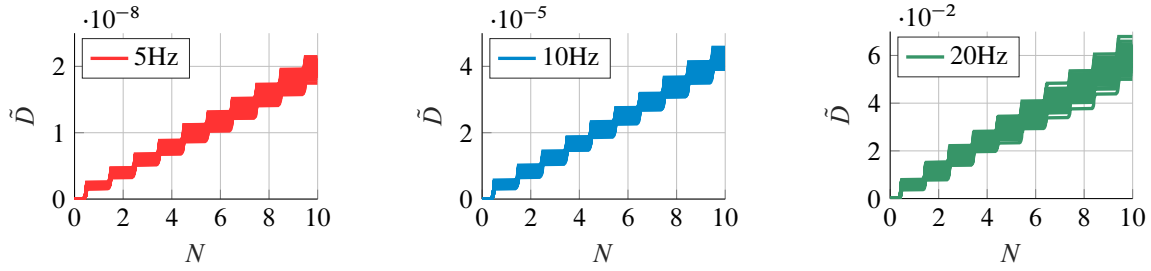


(a) 5Hz (b) 10Hz (c) 20Hz

Figure 6.15: Random fatigue damage using non-proportional diffusion with frequency varies from 5Hz to 20Hz

In practice, the random number generation in eq. (6.39) has certain difficulties because $g(t,x)$ is not explicit for the current time and has to be solved implicitly. The random number $\xi_{t+1}$ at $t+1$

can be generated based on the last drift $g(t, x)$, which is a good approximation of the current one $g(t + 1, x)$. It is necessary to implement a filtering algorithm to ensure the condition $d\tilde{D} \geq 0$. However, this procedure raises again the bias between the damage mean and the deterministic law. One possible solution is to compute the deterministic damage evolution in advance. After that $\xi_{t+1}$ can be generated from the explicit $g(t + 1, x)$. However, this proposal is difficult to associate with the jumping-cycle algorithm since the interval of fully-cycle computation is unique for individual realisation.

In summary, an innovative phenomenological approach based on SDE for random damage modelling is introduced in this chapter. The highlights are

1. Using a sufficiently configured SDE, the realisations of random damage evolution can be statistically unbiased to its deterministic law.

2. The Gaussian white noise is replaced by particularly designed random numbers to satisfy the thermodynamic constraints.

3. With the help of the jumping-cycle algorithm, the proposed stochastic damage law with proportional diffusion is able to reproduce highly accurate fatigue data of brittle material up to the HCF regime.

The previous section demonstrates that the Weibull random number is applicable for a wide range of noise intensity, whereas the log-normal distribution is restricted to simulating small damage randomness. The high-order jumping-cycle algorithms, which have good performance in the deterministic computation, appear stability issues in random fatigue computation.

In contrast to the proportional diffusion, the non-proportional one and its variations can generate an extra frequency effect in the numerical test. However, it is difficult to validate these models because the corresponding experimental data are often not available.

# Chapter 7

# Numerical Implementation

The governing partial differential equations (PDEs) of a solid continuum body are often solved numerically, e.g. using the finite element method. By discretising the object into a finite amount of elements and introducing a time-stepping algorithm, the thermodynamic states can be approximated using the evolution rules. For the random fatigue simulation of concrete, the integration of the stochastic damage law in the classical finite element scheme is introduced.

## 7.1 Finite Element Formulation

**Weak formulation** According to chapter 3 the initial boundary value problem of a deformable continuum body is governed by a set of PDEs. By neglecting the body force $\boldsymbol{f}$, the Cauchy momentum equation in eq. (3.22) for the static mechanical problem can be rewritten as

$$\operatorname{div} \boldsymbol{\sigma} = 0 \quad \text{in } \mathcal{B}. \tag{7.1}$$

The Dirichlet and the Neumann boundary conditions $\bar{\boldsymbol{t}}$, for the displacement and surface traction are given by

$$\begin{cases} \boldsymbol{u} = \bar{\boldsymbol{u}} & \text{on } \partial_u \mathcal{B}, \\ \boldsymbol{t} = \bar{\boldsymbol{t}} & \text{on } \partial_t \mathcal{B}. \end{cases} \tag{7.2}$$

By multiplying an arbitrary test function $\boldsymbol{\eta}$ with eq. (7.1) and using integral over the body, one has

$$G = \int_{\mathcal{B}} \operatorname{div} \boldsymbol{\sigma} \cdot \boldsymbol{\eta} \, dV = 0. \tag{7.3}$$

Applying Gauss's theorem on eq. (7.3) leads to the variational formulation of the boundary value problem, i.e.

$$G = \int_{\mathcal{B}} \boldsymbol{\sigma} : \nabla_x \, \boldsymbol{\eta} \, dV - \int_{\partial\mathcal{B}} \underbrace{\boldsymbol{\sigma} \cdot \boldsymbol{n}}_{:=\boldsymbol{t}} \cdot \boldsymbol{\eta} \, dS = 0, \tag{7.4}$$

in which the operation $\nabla_x(\bullet)$ is performed as

$$\nabla_x(\bullet) = \frac{1}{2}\left[\operatorname{grad}(\bullet) + (\operatorname{grad}(\bullet))^T\right]. \tag{7.5}$$

According to the principle of virtual work, eq. (7.4) yields to

$$G = \delta W_{\text{int}} - \delta W_{\text{ext}} = 0, \tag{7.6}$$

which means the virtual work of internal and external forces, i.e. $\delta W_{\text{int}}$ and $\delta W_{\text{ext}}$, have to be equivalent to each other.

**Linearisation** The constitutive relation of damageable concrete material is often non-linear. In order to approximate the body deformation under external forces, an iterative scheme, e.g. the Newton-Raphson method, is required to solve the governing equations. For an infinitesimal displacement increment $\Delta\boldsymbol{u}$ the linearisation of the variational formulation based on the Taylor expansion is given by

$$G(\boldsymbol{u} + \Delta\boldsymbol{u}) = G(\boldsymbol{u}) + \Delta G(\boldsymbol{u}, \Delta\boldsymbol{u}) + \mathcal{O}, \tag{7.7}$$

in which $\Delta G(\boldsymbol{u}, \Delta\boldsymbol{u})$ is the linear increment of $G$ regarding to $\boldsymbol{u}$, i.e.

$$\Delta G(\boldsymbol{u}, \Delta\boldsymbol{u}) = \frac{\partial G}{\partial \boldsymbol{u}} \Delta\boldsymbol{u}, \tag{7.8}$$

and $\mathcal{O}$ denotes the higher order residual. In the case of displacement independent load, eq. (7.7) can be derived as

$$G(\boldsymbol{u} + \Delta\boldsymbol{u}) = \int_{\mathcal{B}} \boldsymbol{\sigma} : \nabla_x \, \boldsymbol{\eta} \, dV + \int_{\mathcal{B}} \Delta\boldsymbol{\sigma} : \nabla_x \, \boldsymbol{\eta} \, dV - \int_{\partial\mathcal{B}} \boldsymbol{t} \cdot \boldsymbol{\eta} \, dS, \tag{7.9}$$

using the increment of Cauchy stress tensor $\Delta\boldsymbol{\sigma}$. For the regime of small deformation the linearisation of $\Delta\boldsymbol{\sigma}$ is obtained via the material constitutive relation, namely

$$\Delta\boldsymbol{\sigma} = \frac{\partial\boldsymbol{\sigma}}{\partial\boldsymbol{\varepsilon}} \cdot \Delta\boldsymbol{\varepsilon} = \mathbb{D} : \nabla_x \Delta\boldsymbol{u}, \tag{7.10}$$

where $\mathbb{D}$ is the tangent operator of the material constitutive relation in incremental form. Combining eq. (7.10) with eq. (7.9) one has the linearised variational formulation as

$$G(\boldsymbol{u} + \Delta\boldsymbol{u}) = \int_{\mathcal{B}} \boldsymbol{\sigma} : \nabla_x \boldsymbol{\eta} \, dV + \int_{\mathcal{B}} (\mathbb{D} : \nabla_x \Delta\boldsymbol{u}) : \nabla_x \boldsymbol{\eta} \, dV - \int_{\partial\mathcal{B}} \boldsymbol{t} \cdot \boldsymbol{\eta} \, dS. \tag{7.11}$$

**Discretisation** Using the finite element method the continues body $\mathcal{B}$ is divided into $n^e$ elements connected by nodes without overlapping. Let $\Omega_i^e$ denote the domain of each element. The original body is approximated by the collection of all the elementary domains, i.e.

$$\mathcal{B} \approx \bigcup_{i=1}^{n^e} \Omega_i^e := \mathcal{B}^e. \tag{7.12}$$

With the discretisation procedure the displacement field of the continuous problem is interpolated in each individual element from the nodal displacement vector $\boldsymbol{u}^e$ and the shape function matrix $\boldsymbol{N}^e$ as

$$\boldsymbol{u} \approx \boldsymbol{N}^e \boldsymbol{u}^e. \tag{7.13}$$

Similarly, the other quantities e.g. the displacement increment, the surface traction and the arbitrary test function can be approximated as

$$\begin{cases} \Delta \boldsymbol{u} \approx \boldsymbol{N}^e \Delta \boldsymbol{u}^e \\ \boldsymbol{t} \approx \boldsymbol{N}^e \boldsymbol{t}^e \\ \boldsymbol{\eta} \approx \boldsymbol{N}^e \boldsymbol{\eta}^e \end{cases}, \tag{7.14}$$

in which $\Delta \boldsymbol{u}^e$, $\boldsymbol{t}^e$ and $\boldsymbol{\eta}^e$ are the nodal values of the corresponding quantities.

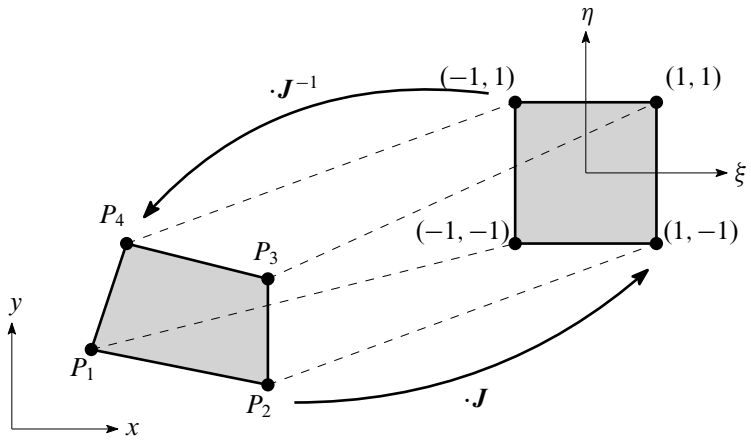


Figure 7.1: Transformation of 2D quadrilateral element between Cartesian and natural coordinates

For efficient finite element computation, the two-dimensional 4-node quadrilateral element (see fig. 7.1) is further implemented in the next chapter. The shape functions that are compatible to this type of element are given by

$$\begin{cases} N_1^e = \frac{1}{4}(1-\xi)(1-\eta) \\ N_2^e = \frac{1}{4}(1+\xi)(1-\eta) \\ N_3^e = \frac{1}{4}(1+\xi)(1+\eta) \\ N_4^e = \frac{1}{4}(1-\xi)(1+\eta) \end{cases}, \tag{7.15}$$

with $\xi$ and $\eta$ denoting the natural (local) coordinates. As a example to demonstrate the discretisation of the displacement field in Cartesian (global) coordinate, the matrix multiplication in eq. (7.13) is performed as

$$\underbrace{\begin{bmatrix} u(x) \\ u(y) \end{bmatrix}}_{\boldsymbol{u}(x,y)} \approx \underbrace{\begin{bmatrix} N_1^e & 0 & N_2^e & 0 & N_3^e & 0 & N_4^e & 0 \\ 0 & N_1^e & 0 & N_2^e & 0 & N_3^e & 0 & N_4^e \end{bmatrix}}_{\boldsymbol{N}^e} \underbrace{\begin{bmatrix} u_x^{P_1} \\ u_y^{P_1} \\ u_x^{P_2} \\ u_y^{P_2} \\ u_x^{P_3} \\ u_y^{P_3} \\ u_x^{P_4} \\ u_y^{P_4} \end{bmatrix}}_{\boldsymbol{u}^e}, \tag{7.16}$$

in which $u_x^{(\bullet)}$ and $u_y^{(\bullet)}$ are the nodal displacement in $x$ and $y$ directions respectively. To apply the isoparametric concept it requires a transformation of the functions from the Cartesian to the natural coordinates, e.g. $\boldsymbol{u}(x, y) \rightarrow \boldsymbol{u}(\xi, \eta)$. Based on the chain rule the transformation between the two coordinates can be obtained by introducing the Jacobian matrix $\boldsymbol{J}$, as

$$\begin{bmatrix} \frac{\partial \boldsymbol{u}}{\partial \xi} \\ \frac{\partial \boldsymbol{u}}{\partial \eta} \end{bmatrix} = \underbrace{\begin{bmatrix} \frac{\partial x}{\partial \xi} & \frac{\partial y}{\partial \xi} \\ \frac{\partial x}{\partial \eta} & \frac{\partial y}{\partial \eta} \end{bmatrix}}_{\boldsymbol{J}} \begin{bmatrix} \frac{\partial \boldsymbol{u}}{\partial x} \\ \frac{\partial \boldsymbol{u}}{\partial y} \end{bmatrix}. \tag{7.17}$$

The quantities $x$ and $y$ in the equation above build the position vector of the material points which are approximated as

$$\underbrace{\begin{bmatrix} x \\ y \end{bmatrix}}_{\boldsymbol{x}} \approx \boldsymbol{N}^e \underbrace{\begin{bmatrix} x^{P_1} & y^{P_1} & x^{P_2} & y^{P_2} & x^{P_3} & y^{P_3} & x^{P_4} & y^{P_4} \end{bmatrix}^T}_{\boldsymbol{x}^e} \tag{7.18}$$

with $(x^{P_\bullet}, y^{P_\bullet})$ denoting the nodal Cartesian coordinates of node $P_\bullet$. To obtain the derivative of the displacement field with regard to the global coordinates, the inverse of the Jacobian matrix, $\boldsymbol{J}^{-1}$, is needed, namely

$$\begin{bmatrix} \frac{\partial \boldsymbol{u}}{\partial x} \\ \frac{\partial \boldsymbol{u}}{\partial y} \end{bmatrix} = \boldsymbol{J}^{-1} \begin{bmatrix} \frac{\partial \boldsymbol{u}}{\partial \xi} \\ \frac{\partial \boldsymbol{u}}{\partial \eta} \end{bmatrix}. \tag{7.19}$$

Based on the coordinate transformation the infinitesimal surface in the global coordinate, $dS$, can be replaced by the determinant of the Jacobian and the local coordinates as

$$dS = dxdy = \det(\boldsymbol{J}) d\xi d\eta. \tag{7.20}$$

For an arbitrary integral with respect to a function $\mathcal{G}$ the implementation of finite element discretisation gives

$$\int_{\mathcal{B}} \mathcal{G}(x, y, z)\, dV \approx \bigcup_{i=1}^{n^e} \int_{\Omega_i^e} \mathcal{G}(x, y, z)\, d\Omega^e = \bigcup_{i=1}^{n^e} \int_{S_i^\square} \mathcal{G}(\xi, \eta)\, t_h \det(\boldsymbol{J})\, dS^\square, \tag{7.21}$$

in which the third direction $z$ is simplified by the element thickness $t_h$, and $S^\square$ is the surface of the discretised element in the local coordinate. Equation (7.21) has to be solved numerically, e.g. using Gauss quadrature method in which $\mathcal{G}$ is evaluated at each Gauss point and further multiplied with the corresponding weight factors $w$. For two dimensional finite element analyses, the numerical integral is performed as

$$\int_{-1}^{+1} \mathcal{G}(\xi, \eta)\, t_h\, d\xi d\eta = \sum_{i=1}^{n_{\text{gp}}} \sum_{j=1}^{n_{\text{gp}}} w_i w_j\, \mathcal{G}(\xi_{\text{gp}}^i, \eta_{\text{gp}}^j)\, t_h. \tag{7.22}$$

The coordinate $(\xi_{\text{gp}}^i, \eta_{\text{gp}}^j)$ depends on the number of Gauss points in each direction $n_g$. Details about the Gauss quadrature method can be reviewed in [144].

**Global iterative scheme** Applying the finite element discretisation on eq. (7.11) gives

$$G(\boldsymbol{u}+\Delta\boldsymbol{u}) \approx \bigcup_{i=1}^{n^e} \boldsymbol{\eta}^T \left( \int_{\Omega_i^e} \boldsymbol{B}^T \boldsymbol{\sigma}\, d\Omega^e\, \boldsymbol{u}_i^e + \int_{\Omega_i^e} \boldsymbol{B}^T : \mathbb{D} : \boldsymbol{B}\, d\Omega^e\, \Delta\boldsymbol{u}_i^e - \int_{\partial\Omega_i^e} \boldsymbol{N}^e \boldsymbol{t}^e\, dS^e \right) = \boldsymbol{0}, \tag{7.23}$$

in which $\boldsymbol{B}$ is the strain-displacement matrix obtained by the derivative of the shape functions with respect to the global coordinate. Let $\boldsymbol{K}$ denote the global stiffness matrix with the expression

$$\boldsymbol{K} = \bigcup_{i=1}^{n^e} \int_{\Omega_i^e} \boldsymbol{B}^T : \mathbb{D} : \boldsymbol{B}\, d\Omega^e. \tag{7.24}$$

Equation (7.23) is thus equivalent to the global problem

$$\boldsymbol{F}^{\text{int}} + \boldsymbol{K}\,\Delta\boldsymbol{u} - \boldsymbol{F}^{\text{ext}} = 0. \tag{7.25}$$

Given the nodal force vector $\boldsymbol{F}^{\text{ext}}$, the global Newton-Raphson scheme for the solution of eq. (7.25) is demonstrated in algorithm 1. The algorithm starts from the initiation of the displacement vector and the global stiffness matrix. During the iteration, the material states are updated by the last trial values. It terminates when the difference between the internal and the external forces sufficient small. The criteria is given by

$$\epsilon = \frac{\|\boldsymbol{r}\|}{\|\boldsymbol{F}^{\text{ext}}\|} \leq tol \quad \text{with} \quad \boldsymbol{r} = \|\tilde{\boldsymbol{F}}^{\text{int}} - \boldsymbol{F}^{\text{ext}}\|, \tag{7.26}$$

where $\epsilon$ is the relative error between the residual and the external force, and $tol$ is the tolerance, a sufficiently small positive number near to zero such as $tol = 10^{-6}$.

**Algorithm 1** Global Newton-Raphson scheme

**Initiation**: nodal displacement vector $\boldsymbol{u}_0$, global stiffness matrix $\boldsymbol{K}_0$

1: Compute $\boldsymbol{F}^{\text{int}}$ and the residual $\boldsymbol{r}$
2: Compute ${}^{\text{tr}}\Delta\boldsymbol{u} = \boldsymbol{K}^{-1}\boldsymbol{r}$
3: Update ${}^{\text{tr}}\boldsymbol{u} = \boldsymbol{u} + {}^{\text{tr}}\Delta\boldsymbol{u}$, compute ${}^{\text{tr}}\boldsymbol{K}$ and ${}^{\text{tr}}\boldsymbol{F}^{\text{int}}$
4: Check convergence with $\epsilon = \frac{\|\boldsymbol{r}\|}{\|\boldsymbol{F}^{\text{ext}}\|}$
5: **if** $\epsilon \leq tol$ **then** accept trial values from step 3
6: **else** go to step 1

## 7.2 Integration of Random Fatigue Damage

For fatigue computation, the amplitude of the surface traction is changing periodically. The external force vector is refreshed at each time step and given as an input of the global Newton-Raphson algorithm. The computation of the global stiffness matrix relies on the knowledge of the

tangent operator, which further depends on the evaluation of internal variables at each integration point. Since the tangent operator has non-linear behaviour beyond the elasticity region, an implicit scheme for updating the internal variables must be integrated into the global scheme (at step 3 of algorithm 1). The details about the integration of random damage evolution and jumping-cycle algorithm are explained in the following contents.

**Local implicit scheme** Giving the material state at $t = i$ and the external force vector $\boldsymbol{F}_{i+1}^{\text{ext}}$ at $t = i + 1$, a trial displacement ${}^{\text{tr}}\boldsymbol{u}_{i+1}$ as a global variable is imported to the local scheme. Due to the application of Gaussian quadrature method at local level the trial strain tensor ${}^{\text{tr}}\boldsymbol{\varepsilon}_{i+1}$ can be calculated at each Gauss point $x_{\text{gp}}(\xi^i, \eta^j)$ through

$$ {}^{\text{tr}}\boldsymbol{\varepsilon}_{i+1}(\xi_{\text{gp}}^i, \eta_{\text{gp}}^j) = \boldsymbol{B}(\xi_{\text{gp}}^i, \eta_{\text{gp}}^j) \cdot \boldsymbol{u}^e. \tag{7.27} $$

To implement the proposed isotropic brittle damage law in section 4.1.3 the strain tensor is decomposed to the deviatoric and hydrostatic part using eqs. (4.25) and (4.26). After that the initial quantities in terms of trial stress ${}^{\text{tr}}\boldsymbol{\sigma}_{i+1}^{k=0}$ and the thermodynamic force ${}^{\text{tr}}Y_{i+1}^{k=0}$ can be obtained using eqs. (4.28) and (4.29). Substituting ${}^{\text{tr}}Y_{i+1}^{k=0}$ and the initial guess ${}^{\text{tr}}D_{i+1}^{k=0} = D_i$ into the dissipation function given by eq. (4.31), the damage evolution is activated at those integration points where the following criteria is fulfilled, namely

$$ F^d({}^{\text{tr}}Y_{i+1}^k,\ {}^{\text{tr}}D_{i+1}^k) > 0. \tag{7.28} $$

Similar to the yield surface concept in the plasticity theory, eq. (7.28) indicates that the current trial ${}^{\text{tr}}D_{i+1}^k$ is out of the damage surface. A local corrector step (return mapping algorithm) is needed such that after the correction the damage variable is back to the damage surface, i.e.

$$ F^d({}^{\text{tr}}Y_{i+1}^k,\ {}^{\text{tr}}D_{i+1}^k) \leq 0. \tag{7.29} $$

Given the previous state of thermodynamic force $Y_i$, the trial increment is calculated using the forward difference as

$$ {}^{\text{tr}}\Delta Y_i^k = {}^{\text{tr}}Y_{i+1}^k - Y_i. \tag{7.30} $$

According to the damage evolution rate given in eq. (4.36), the trial damage increment is given by

$$ {}^{\text{tr}}\Delta D_i^k = \Delta t \left\langle \frac{{}^{\text{tr}}Y_{i+1}^k}{S} \right\rangle^{s_1} \left\langle \frac{{}^{\text{tr}}Y_{i+1}^k - Y_i}{\Delta t} \right\rangle^{s_2}. \tag{7.31} $$

In view of eqs. (6.21), (7.30) and (7.31) the stochastic damage increment for the case of proportional diffusion is obtained as

$$ {}^{\text{tr}}\Delta \tilde{D}_i^k = {}^{\text{tr}}\Delta D_i^k \left(1 + \frac{\gamma \xi_t}{\sqrt{\Delta t}}\right) = f_{\Delta D}\left({}^{\text{tr}}Y_{i+1}^k, Y_i\right), \tag{7.32} $$

with dependence on ${}^{\text{tr}}Y_{i+1}$. Following the designing process in section 6.2.1 suitable random numbers $\xi_{i+1}$ can be generated for the integration points, where the damage evolution is activated. Given the prior damage $\tilde{D}_i$ and ${}^{\text{tr}}Y_{i+1}$, the trial damage is obtained by solving the function system

$$ \begin{cases} {}^{\text{tr}}\tilde{D}_{i+1}^k - \tilde{D}_i - f_{\Delta D}\left({}^{\text{tr}}Y_{i+1}^k, Y_i\right) = 0, \\ F^d({}^{\text{tr}}Y_{i+1}^k,\ {}^{\text{tr}}\tilde{D}_{i+1}^k) = 0. \end{cases} \tag{7.33} $$

After that, the trial tangent operator is updated at each integration point using eq. (4.30). Together with the strain-displacement matrix, the trial local stiffness is computed as

$$ {}^{\mathrm{tr}}\boldsymbol{K}^{e} = \sum_{i=1}^{n_{\mathrm{gp}}} \sum_{j=1}^{n_{\mathrm{gp}}} \boldsymbol{B}^{T}(\xi_{\mathrm{gp}}^{i}, \eta_{\mathrm{gp}}^{j})\ {}^{\mathrm{tr}}\mathbb{D}(\xi_{\mathrm{gp}}^{i}, \eta_{\mathrm{gp}}^{j})\ \boldsymbol{B}(\xi_{\mathrm{gp}}^{i}, \eta_{\mathrm{gp}}^{j}) w_i w_j t_h. \tag{7.34} $$

The local iteration is finished at this point, followed by the assembling of the trial global stiffness matrix ${}^{\mathrm{tr}}\boldsymbol{K}$ and the convergence check at the global level. The interaction between the local and global scheme is visualised in fig. 7.2, and the detailed numerical steps are reviewed in algorithm 2.

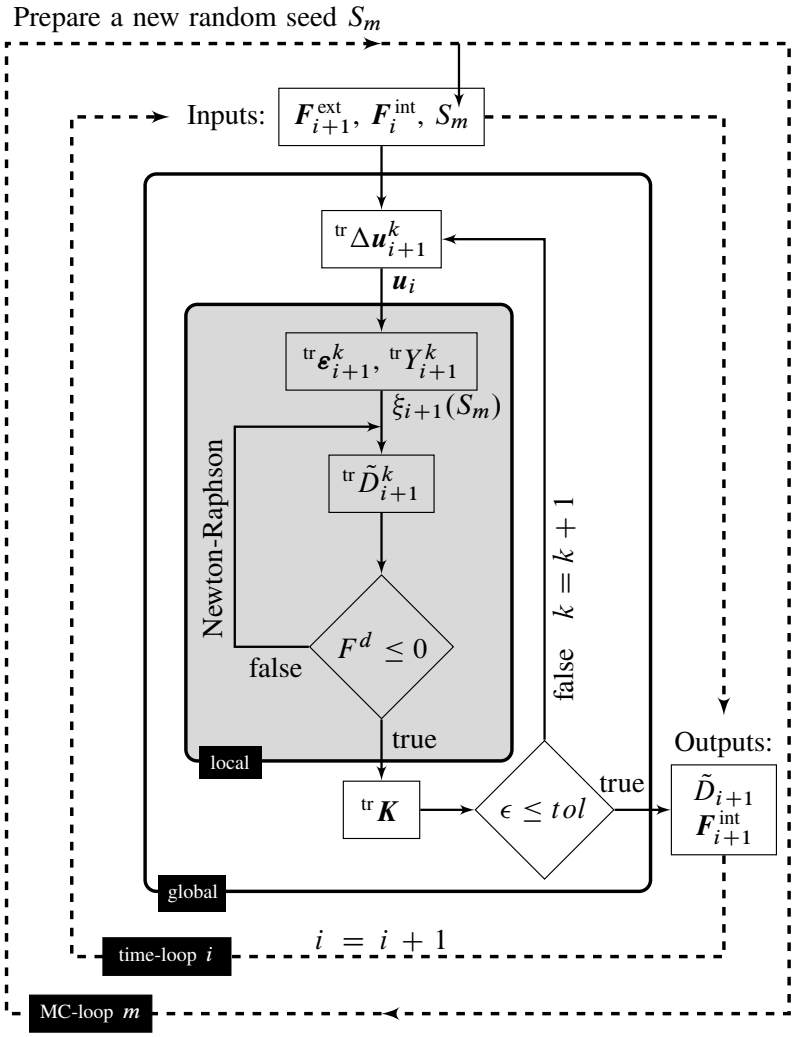


Figure 7.2: Interaction of local and global scheme in the finite element computation

**Algorithm 2** Implicit scheme of finite element computation considering stochastic damage increment

**Input:** $\boldsymbol{F}_{i+1}$ external load at $i+1$, $\xi_{i+1}$ random noise, material states at $t$ and material parameters
**Output:** $\tilde{D}_{i+1}$, material states at $i+1$

1: initial guess for $t+1$

$$ {}^{\mathrm{tr}}\boldsymbol{F}_{i+1}^{\mathrm{int}\,(k)} = \boldsymbol{F}_{i}^{\mathrm{int}},\ {}^{\mathrm{tr}}\boldsymbol{u}_{i+1}^{k=0} = \boldsymbol{u}_{i},\ {}^{\mathrm{tr}}\boldsymbol{K}_{i+1}^{k=0} = \boldsymbol{K}_{i},\ {}^{\mathrm{tr}}D_{i+1}^{k=0} = D_{i}; $$

2: compute residual vector

$$ {}^{\mathrm{tr}}\boldsymbol{r}_{i+1}^{k} = \underbrace{{}^{\mathrm{tr}}\boldsymbol{K}_{i+1}^{k}\,{}^{\mathrm{tr}}\boldsymbol{u}_{i+1}^{k}}_{\boldsymbol{F}_{i+1}^{\mathrm{int}\,(k)}} - \underbrace{\boldsymbol{F}_{i+1}}_{\boldsymbol{F}_{i+1}^{\mathrm{ext}}}; $$

3: **if** $ {}^{\mathrm{tr}}\left\|\boldsymbol{r}_{i+1}^{k}\right\| \Big/ \left\|\boldsymbol{F}_{i+1}\right\| \leq tol$ **then**

4: **return** $D_{i+1} = {}^{\mathrm{tr}}D_{i+1}^{k}$, $\boldsymbol{K}_{i+1} = {}^{\mathrm{tr}}\boldsymbol{K}_{i+1}^{k}$; *// accept trial k and go for the next time step*

5: **else** $k = k+1$;

6: compute displacement increment vector

$$ {}^{\mathrm{tr}}\Delta\boldsymbol{u}_{i+1}^{k} = {}^{\mathrm{tr}}\boldsymbol{r}_{i+1}^{k} / {}^{\mathrm{tr}}\boldsymbol{K}_{i+1}^{k}; $$

7: update displacement vector

$$ {}^{\mathrm{tr}}\boldsymbol{u}_{i+1}^{k} = {}^{\mathrm{tr}}\boldsymbol{u}_{i+1}^{k-1} + {}^{\mathrm{tr}}\Delta\boldsymbol{u}_{i+1}^{k}; $$

8: get strain tensor

$$ {}^{\mathrm{tr}}\boldsymbol{\varepsilon}_{i+1}^{k} = \boldsymbol{B}\ {}^{\mathrm{tr}}\boldsymbol{u}_{i+1}^{k}; $$

9: compute the damage driving force

$$ {}^{\mathrm{tr}}Y_{i+1}^{k} = \frac{1}{2}\,{}^{\mathrm{tr}}\boldsymbol{\varepsilon}_{i+1}^{k} : \mathbb{C} : {}^{\mathrm{tr}}\boldsymbol{\varepsilon}_{i+1}^{k}; $$

10: check the damage criteria

$$ F^{d}({}^{\mathrm{tr}}Y_{i+1}^{k},\ {}^{\mathrm{tr}}D_{i+1}^{k}); $$

11: **if** $F^{d} \leq 0$ **then**

12: go to line2; *// no damage evolution*

13: **else** *// local return mapping to the damage surface* $F^{d} = 0$

14: compute trial stochastic damage by solving eq. (7.33)

$$ {}^{\mathrm{tr}}\tilde{D}_{i+1}^{k}\left(\xi_{i+1},\ {}^{\mathrm{tr}}Y_{i+1}^{k}\right); $$

15: update tangent operator using eq. (4.30)

$$ {}^{\mathrm{tr}}\mathbb{D}_{i+1}^{k}\left({}^{\mathrm{tr}}\tilde{D}_{i+1}^{k}\right); $$

16: update local stiffness matrix with eq. (7.34)

$$ {}^{\mathrm{tr}}\boldsymbol{K}_{i+1}^{e\,(k)} = \boldsymbol{K}_{i+1}^{e\,(k)}\left({}^{\mathrm{tr}}\mathbb{D}_{i+1}^{k}\right); $$

17: Assemble of global stiffness matrix $ {}^{\mathrm{tr}}\boldsymbol{K}_{i+1}^{k}$;

18: let $k = k+1$ and go to line 2;

**Choose of different stochastic integrals** The stochastic integrals are generally compared in section 2.2. The fundamental difference between the Ito and Stratonovich integral is the integration point $\tau_i$ chosen form the time interval $[t_{i-1}, t_i]$. Let $\theta_\tau \in [0, 1]$, and $\tau_i = (1 - \theta_\tau)t_{i-1} + \theta_\tau t_i$. The Ito integral is equivalent to $\theta_\tau = 0$ whereas the Stratonovich integral is $\theta_\tau = 0.5$ [145]. One can demonstrate the difference by rewriting eq. (6.5) in the incremental way. For the stochastic damage evolution at a specified Gauss point, given the damage state $\tilde{D}_i$ at $t_i$, $\tilde{D}_{i+1}$ is computed via the Ito integral as

$$\tilde{D}_{i+1} = \tilde{D}_i + g_i \Delta t + h_i \Delta \mathbb{W}. \tag{7.35}$$

Since the drift term is identical to the deterministic damage evolution rate $g_i$ is approximated using the forward difference of $\dot{Y}$ as

$$g_i = \dot{D}_i = \left\langle \frac{Y_i}{S} \right\rangle^{s_1} \left\langle \frac{Y_{i+1} - Y_i}{\Delta t} \right\rangle^{s_2} = f_g(Y_{i+1}, Y_i) \propto h_i. \tag{7.36}$$

Equation (7.35) can be then written as

$$\tilde{D}_{i+1} = \tilde{D}_i + f_{\Delta D}\left(Y_{i+1}, Y_i\right), \tag{7.37}$$

which is an implicit scheme depending on $t_{i+1}$.

In contrast, according to the equivalence relation given in eq. (2.19), while applying the Stratonovich integral on eq. (7.35) one has

$$\tilde{D}_{i+1} = \tilde{D}_i + \left( g_i - \frac{1}{2} \underbrace{\frac{h_{i+1} - h_i}{\Delta D}}_{\frac{\partial h}{\partial D}} h_i \right) \Delta t + \frac{h_{i+1} + h_i}{2} \Delta \mathbb{W}, \tag{7.38}$$

in which the term $h_{i+1}$ requires the knowledge of $Y_{i+2}$ such as

$$h_{i+1} \propto g_{i+1} = \left\langle \frac{Y_{i+1}}{S} \right\rangle^{s_1} \left\langle \frac{Y_{i+2} - Y_{i+1}}{\Delta t} \right\rangle^{s_2}. \tag{7.39}$$

This is incompatible with the classical return-mapping scheme because it is challenging to compute the internal variables at $t_{i+1}$, which depends on an unknown quantity at $t_{i+2}$.

Alternatively, using the backward difference to evaluate $\dot{Y}$ can reduce the complexity. In this case, eq. (7.35) is represented by the Ito integral as an explicit scheme, namely

$$\tilde{D}_{i+1} = \tilde{D}_i + f_{\Delta D}\left(Y_i, Y_{i-1}\right). \tag{7.40}$$

To improve the accuracy the drift and diffusion terms can be evaluated at the right point $t_{i+1}$ during the subinterval $[t_i, t_{i+1}]$. Similarly, a fully implicit scheme using the Stratonovich integral can be obtained by replacing $g_i$ with $g_{i+1}$ in eq. (7.38) as

$$\tilde{D}_{i+1} = \tilde{D}_i + \left( g_{i+1} - \frac{1}{2} \frac{h_{i+1} - h_i}{\Delta D} h_{i+1} \right) \Delta t + \frac{h_{i+1} + h_i}{2} \Delta \mathbb{W}. \tag{7.41}$$

However, by reviewing eqs. (7.38) and (7.41), it is difficult to guarantee the diffusion to be proportional to its drift, regardless of the finite difference method. This observation is in accordance

with the conclusion from previous studies [23, 22, 32]. For a concise iterative formula with guaranteed numerical accuracy, the Ito integral and the implicit Euler method are implemented in further numerical investigations. The scheme is expressed as

$$\tilde{D}_{i+1} = \tilde{D}_i + g_{i+1}\Delta t + h_{i+1}\Delta \mathbb{W}, \tag{7.42}$$

with

$$h_{i+1} \propto g_{i+1} = \left\langle \frac{Y_{i+1}}{S} \right\rangle^{s_1} \left\langle \frac{Y_{i+1} - Y_i}{\Delta t} \right\rangle^{s_2}. \tag{7.43}$$

**Monte-Carlo loop** For many scientific computing platforms, the Mersenne-Twister is often the default algorithm to generate pseudo-random numbers. This algorithm allows the generation result to be repeatable using the same random seed [146]. In practices, the random seed is created based on the current time of the operating system (OS) to avoid repeatability. For the FE-analyse of $m$ MC samples, an independent seed value has to be assigned to individual computation. As shown in fig. 7.2, a new random seed $S_m$ is prepared at the beginning of each MC iteration and taken by the FE-scheme to generate the damage increment noise during the local iteration. After finishing $m$-series of FE-computation, one has $m$ realisations of the damage evolution at each integration point.

**Integration of the jumping-cycle algorithm** After a full cycle of finite element computation the cyclic damage increment is converted to the damage growth in time as

$$\frac{\Delta D}{\Delta N} = \sum_{i=1}^{n_{\Delta t}} \Delta D_i, \tag{7.44}$$

with $n_{\Delta t}$ denoting the number of time steps per cycle. Depending on the value of $\Delta D_i$, $\frac{\Delta D}{\Delta N}(N, x_{\mathrm{gp}})$ can vary at each integration point. Especially for the effect of damage concentration in structural analysis, the extrapolation strategy has to be developed to have an unified number of jump for the global iteration. Given a fixed demand of extrapolation in damage $\frac{D_c}{\kappa}$ the value of $\Delta N$ is determined at the weakest Gauss point, where the highest cyclic damage increment is measured, namely

$$\Delta N = \frac{D_c}{\kappa} \Big/ \max\left[\frac{\delta D}{\delta N}(N, x_{\mathrm{gp}})\right] \text{[1]}. \tag{7.45}$$

After an extrapolation procedure, if the highest damage value is below $D_c$, the damage field is imported to the subsequent full-cycle FE computation. During the jumping-cycle scheme, the extrapolated and the fully computed number of cycles are saved as temporary variables to calculate the fatigue life. The iteration terminates when the critical damage value 0.3 is reached. The corresponding number of cycles is recorded as the fatigue life $N_f$.

[1] the first order jumping-cycle algorithm is applied here to be consistent with the conclusion from section 6.2.1

# Chapter 8

# Finite Element Computation of Four-Point Flexural Fatigue Problem

The stochastic damage evolution law for brittle material proposed in the previous chapter is implemented on the four-point flexural fatigue problem of concrete beam structure solved by the finite element method. This particular example is selected for two main reasons. First, mechanical reaction under bending load has sufficient complexity. It contains compressive, tensive and shearing deformation, which is desired for testing the proposed deterministic brittle damage model, especially for the simulation of the unilateral effect. Second, flexural fatigue data are reported by many laboratory studies [17, 21] on which statistical analysis can be applied to calibrate the random damage model.

Compared to other studies [24, 25], this study aims to verify the model using structural analysis. The classical finite element method is associated with the jumping-cycle algorithm to efficiently reproduce HCF data. For multiple random damage realisations, the Monte-Carlo method is implemented. The simulation is often computationally heavy, due to the demand on large time interval and enormous samples. For high computational efficiency, the following numerical test takes a two dimensional FE model. The experimental data in terms of fatigue life provided in [17] has to be agreed by the reproduced virtual fatigue data both in the mean and variance.

## 8.1 Deterministic Computation

To be identical to the geometry of concrete specimen in [17], the beam demonstrated in fig. 8.1 has a length $L = 0.5$ m and a cross-sectional area of $A = 0.1$ m$\times$0.1 m. The distance between the two supporting points at the bottom and the two loading points at the top are $L_s = 0.45$ m and $L_i = 0.1$ m respectively. The two concentrated loads are identical with the maximum amplitude $F_{\mathrm{M}} = -11.5$ kN, the loading ratio $R = 0.1$ and the frequency $f = 10$ Hz. To reduce the complexity, this model is simplified as a two-dimensional plane stress problem with the thickness of $t_h = 0.1$ m. As an example, a 10$\times$50 finite element mesh can be seen in fig. 8.2. The boundary condition of the displacement constraints for the left and right supporting points are $U_x^L = U_y^L = 0$ and $U_y^R = 0$. The material is a reinforced concrete with 0.5% steel-fibre (SFRSCC005) with parameters collected in table 8.1.

According to laboratory observations, the main failure form of the concrete beam under the

flexural test is the tension failure. In contrast, the compressive failure at the loading and supporting points are negligible. Indeed, the highest damage value shall appear at the bottom side, middle of the two supporting points, where the macroscopic cracks get first initialised. For the numerical test, fatigue life is determined by the damage at the weakest element averaged from the corresponding integration points. Once the critical damage value is reached at this element, the current cycle is a good approximation of the experimental fatigue life. Instead of introducing the simple displacement constraints for the support pins, it is often more accurate to introduce contact mechanics to the FE analysis of the four-point bending problem. This approach is avoided due to the high computational cost of the contact problem.

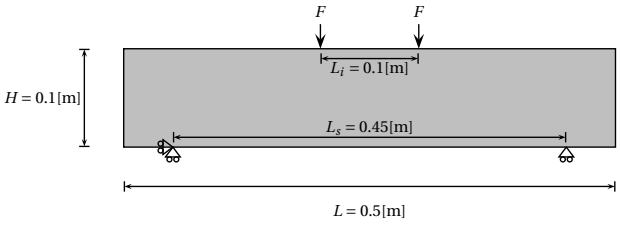


Figure 8.1: Geometry of the beam structure under four-point bending test

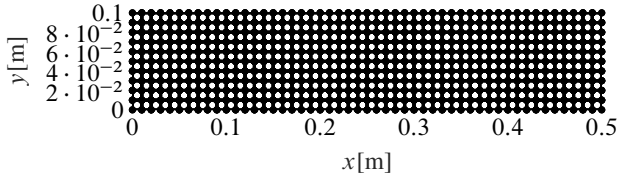


Figure 8.2: 2D FE mesh discretised by 500 uniform four-node elements

Table 8.1: Calibrated material parameters of SFRSCC005

| $E$ | $\nu_c$ | $S$ | $s$ | $s_1$ | $Y_D$ | $D_c$ |
|---|---|---|---|---|---|---|
| 42 GPa | 0.2 | 1.51kPa$^2$ | 11.05 | 1 | 4.5kPa | 0.3 |

**Influences of constitutive parameters** After applying the newly proposed brittle constitutive relation in eq. (4.27) with a trial $\varphi = 1$, a contour plot of the extrapolated damage value on the whole structure can be seen in fig. 8.3. Under this setting, both the deviatoric and the hydrostatic stress affect the damage evolution. Due to the concentrated shear stress, the damage is localised at the loading and supporting points, whereas it is minor at the bottom centre. An evident mesh-size effect is also observable after comparing the two different meshes, showing that damage concentration is stronger with finer mesh. For another trial test of $\varphi = 0$ the results are illustrated in fig. 8.4, showing nearly no mesh dependency. In this case, only the hydrostatic stress in the tensile direction is in charge of damage growth. Though the compressive hydrostatic stress at the top centre of the beam is intensive, the damage is almost invisible at this location. This means the unilateral effect

has been successfully simulated. As an outcome from these trials, to capture a realistic location of crack initiation, a proper $\varphi$ has to be determined to balance the contribution of deviatoric and hydrostatic stress. Since it is difficult to classify the specimen as a short or long beam, the span of $L/H = 5, \varphi = 0.2$ is used in the following tests to enable the shear conduced damage. Meanwhile, the level of damage concentration at the bottom is governed by the parameter $s$ in the damage law. As can be read from fig. 8.5 the size of the weak area is dramatically reduced by $s = 15$. It means more intensive concentration of damage in comparison to fig. 8.4 with $s = 11.05$.

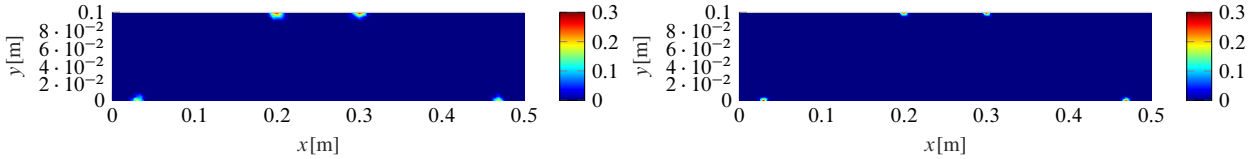


(a) 10×50 mesh (b) 20×100 mesh

Figure 8.3: Damage with $\varphi = 1$

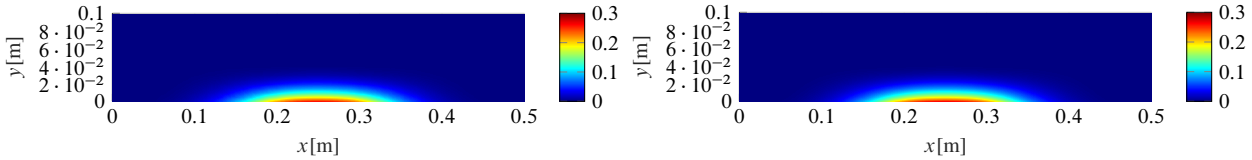


(a) 10×50 mesh (b) 20×100 mesh

Figure 8.4: Damage field with $\varphi = 0$

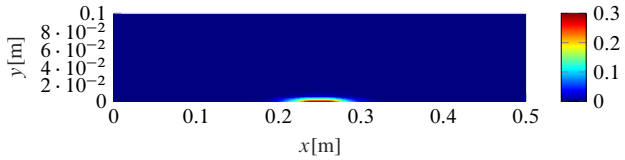


Figure 8.5: Damage field with $\varphi = 0$, $s = 15$ on 20×100 mesh

**Influences of time discretisation and jumping parameter** The exact shape of the loading wave is not given by the literature [17]. To understand the influence of time-step size on fatigue life, two proposals, i.e. saw-tooth and sinus-shaped loading waves (see fig. 8.6), are compared.

To capture the maximum and minimum value of the loading wave, the number of time discretisation per cycle $n_{\Delta t}$ is configured as a multiple of the number 4 ranging from 40 to 1000. According to fig. 8.7, for deterministic computation the time discretisation is a dominant factor in comparison to $\kappa$. Meanwhile, the sinus load shows better convergence speed than the saw-tooth like load if the time step size reduces. In the following numerical test, the sinus load with $n_{\Delta t} = 400$, i.e. $\Delta t = 2.5e-4$ s, is applied. For high cycle computation, the robust first-order jumping cycle algorithm with $\kappa = 100$ is implemented after a full-cycle FE computation.

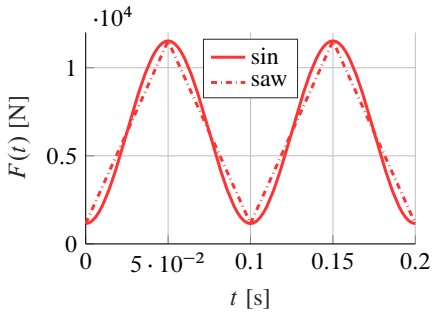


Figure 8.6: Sinus and saw-tooth shaped loading wave with amplitude $F_M$ (identical to $L_s = 1$)

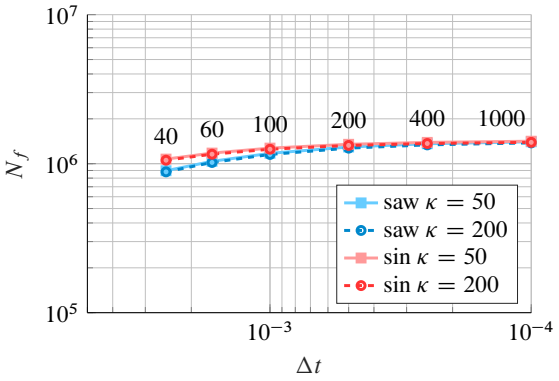


(a) Convergence of fatigue life estimation regarding to time step size

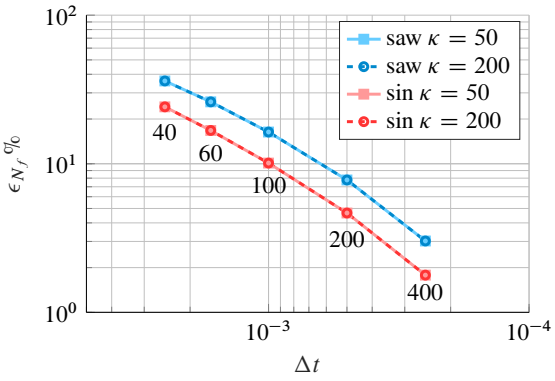


(b) Relative error of fatigue life with respect to the reference estimation using $\Delta t = 1e-4\,\mathrm{s}$

Figure 8.7: Influence of time discretisation per cycle on fatigue life estimation

**Reproduced S-N curve** By taking the five load levels from 0.7 to 0.9, the amplitude of the concentrated force is adjusted via $L_s \cdot F_M$ for the corresponding levels. As illustrated in fig. 8.8 the computed fatigue life for each level is able to fit with the empirical relation. The relative error is generally very low (smaller than 1%) for all the loading levels, which means the deterministic model parameters are accurately calibrated.

## 8.2 Monte-Carlo Simulation

For each MC realisation, the proposed quasi-brittle damage law is computationally efficient because plasticity is not involved in the local return mapping algorithm but only the damage surface. The random damage law with proportional diffusion is mainly analysed in this section. The random number generated from the positive distribution $\mathcal{N}^+(1,1)$ is the first trial for FE analysis, which is compared later to the results with different variances.

**Effect of the jumping-cycle procedure and sampling amount** The influence of the jumping-cycle algorithm on random fatigue damage evolution in the concrete structure is analysed via 1000 realisations. As shown in fig. 8.9, the influence of $\kappa$ is far more significant on the standard deviation

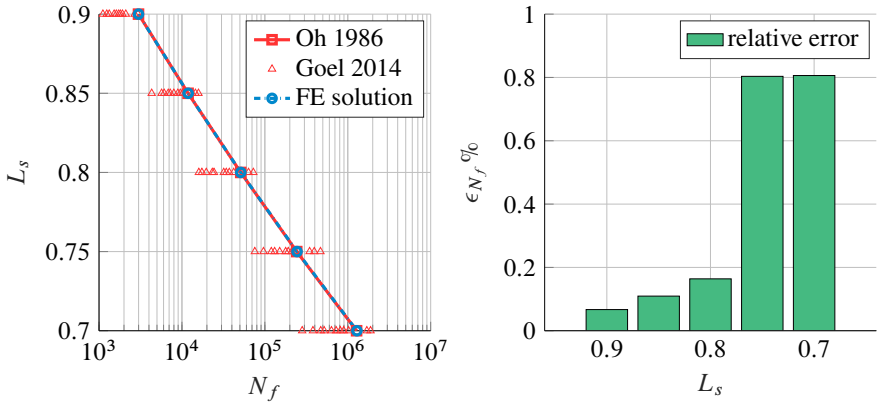


Figure 8.8: Deterministic results versus empirical S-N relation and experimental data

than on the fatigue mean. The setting $\kappa = 100$ is necessary to guarantee a relative error smaller than 1%. Moreover, the MC sampling amount $N^p$ for structural analysis is also determined as $\kappa = 100$. The results are plotted in fig. 8.10. Compared to the statistical mean, the error of standard deviation converges slow. A similar observation can be seen in fig. 6.7 from section 6.2.1. Since $\kappa = 100$ indicates the minimum number of full-cycle computation, for every single specimen with 400 discretisations per cycle, one needs to solve the global FE problem $4 \times 10^4$ times in total. The cost on a single CPU core at 5GHz is around 1700 seconds ($\approx$ 30 minutes). The value $N^p$ is set as 1000 to balance the cost and the estimation accuracy.

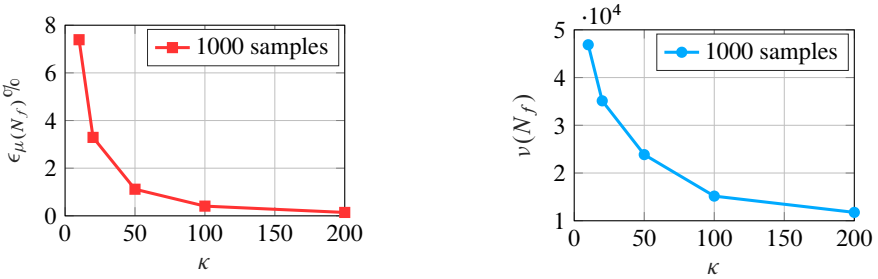


(a) relative error of mean

(b) standard deviation

Figure 8.9: Influence of $\kappa$ on 2D FE results in terms of the statistics on random fatigue life

**Stochastic fatigue damage evolution** Consider the material parameters in table 8.1 and the settings for the numerical scheme namely $\Delta t = 2.5 \times 10^{-4}$ s, $\kappa = 100$ and $N^p = 1000$. The mean of the damage field is illustrated in fig. 8.11. It is similar to the deterministic result. With $\varphi = 0.2$ the shear-induced damage at the loading and supporting points becomes minor, compared to the damage at the bottom. For examples, the damage evolution of the element at the bottom centre for the load level $L_s = 0.7$ up to $10^6$ cycles is plotted in fig. 8.12a where the width of the confident interval increases during the number of cycles. Particularly, the uncertainty in the number of cycles increases sub-linearly versus the mean. This relation is plotted in fig. 8.12b. At the end of damage evolution $\tilde{D} = D_c$, statistics on the fatigue life is shown in fig. 8.13. The probabilistic

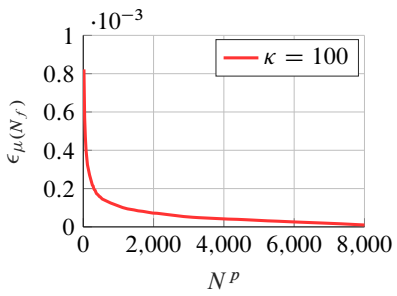


(a) relative error of mean

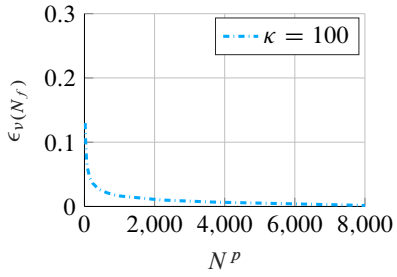


(b) relative error of standard deviation

Figure 8.10: Influence of sampling amount on 2D FE results in terms of the statistics on random fatigue life

density of the simulated fatigue life data is nearly symmetric (see fig. 8.13a) while taking the mean $\mu(N_f) = 1.17 \times 10^6$. The probability of failure represented by the CDF of the generated data is illustrated in fig. 8.13b. The uncertainty in the reproduced fatigue life based on $\mathcal{N}^+(1,1)$ is much smaller than the experimental data. One possible solution is to increase the noise intensity in the random variable. In the following context, the results of Weibull and Gaussian random number with different variances are presented. It shows the applicability and limitations of the two random numbers in structural fatigue analysis.

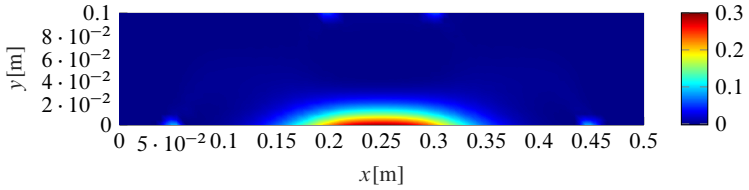


Figure 8.11: Field of damage mean

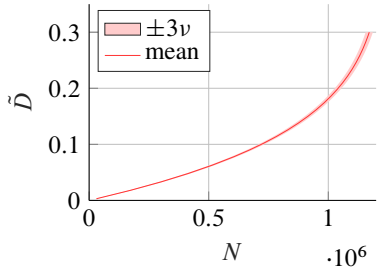


(a) damage evolution

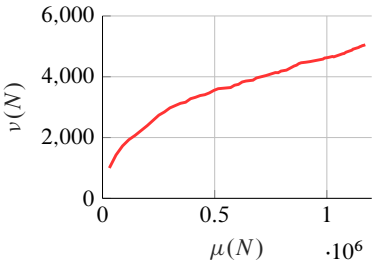


(b) uncertain in cycle

Figure 8.12: Damage evolution at $L_s = 0.7$ with probabilistic information

**Weibull versus Gaussian random number** The procedures for generating thermodynamically consistent random numbers from a designed distribution are declared in section 6.2.1. While

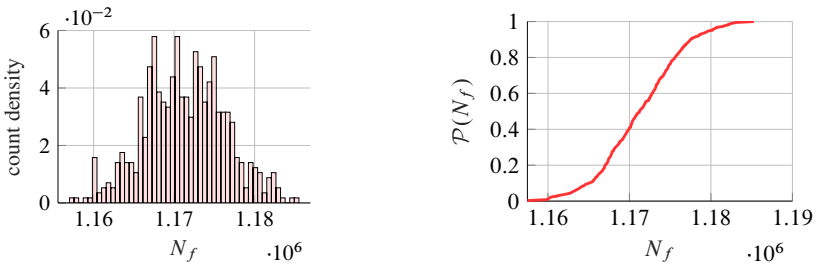


(a) histogram of density (b) probability of failure

Figure 8.13: Statistics on fatigue life

preparing the random numbers, the Weibull distribution has to be shifted to zero mean, and the Gaussian white noise requires a filtering procedure. In this test, a Weibull distribution with ten times larger standard deviation, namely $\mathcal{N}^+(1, 10^2)$, is employed to demonstrate its performance in comparison to the filtered Gaussian random noise. For good readability, random numbers generated from different distributions are named as follows:

$$\xi_t \sim \begin{cases} N(0,1) \cdot \sqrt{\Delta t}/3 & \text{GS;} \\ N(0,10^2) \cdot \sqrt{\Delta t}/3 & \text{GL;} \\ \left[\mathcal{N}^+(1,1) - 1\right] \cdot \sqrt{\Delta t}/3 & \text{WBS;} \\ \left[\mathcal{N}^+(1,10^2) - 1\right] \cdot \sqrt{\Delta t}/3 & \text{WBL;} \end{cases} \tag{8.1}$$

The short forms "GS", "GL", "WBS" and "WBL" correspond to the Gaussian (G) and Weibull (WB) random number with small (S) and large (L) variance.

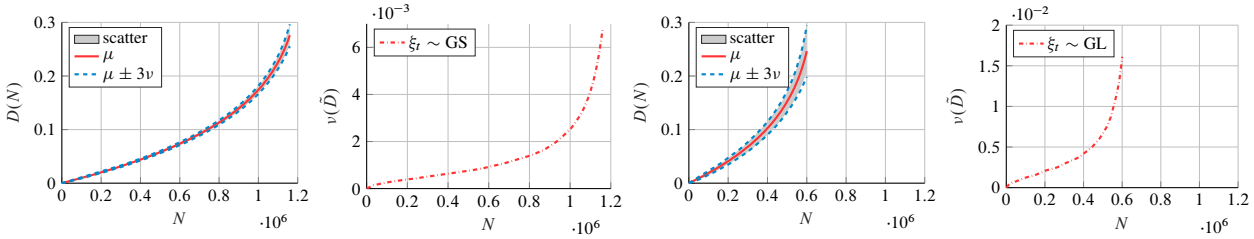


(a) scatter band GS (b) uncertainty propagation (c) scatter band GL (d) uncertainty propagation

Figure 8.14: Solution with the Gaussian random number

In view of figs. 8.14a, 8.14b, 8.15a and 8.15b, both the scatter band of damage evolution and the propagation of uncertainty are very close. The reason is that the filtering procedure on the Gaussian noise with small variance has minor effect. However, this effect becomes drastic in figs. 8.14c and 8.14d because the evolution speed is significantly increased. In this case, the mean of the accepted Gaussian random number is shifted from zero to positive. In contrast, the Weibull distribution is able to maintain the damage evolution rate by its mean while increasing the uncertainty (see figs. 8.15c and 8.15d).

Continue this comparison on the five load levels. The results using Gaussian random variable with two different variance configurations can be seen infig. 8.16a. With the GS variables, the

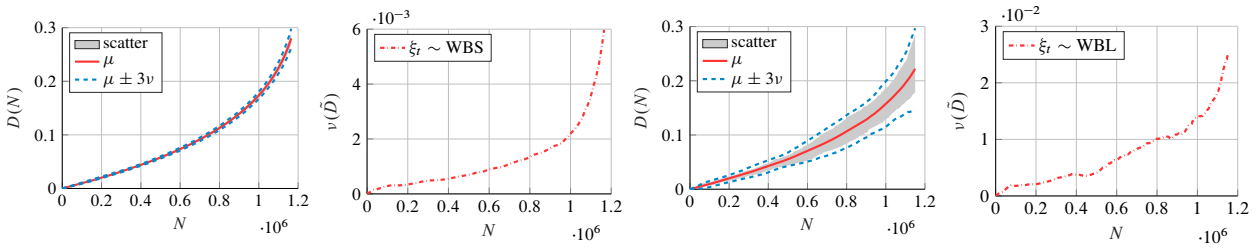


(a) scatter band WBS (b) uncertainty propagation (c) scatter band WBL (d) uncertainty propagation

Figure 8.15: Solution with the Weibull random number

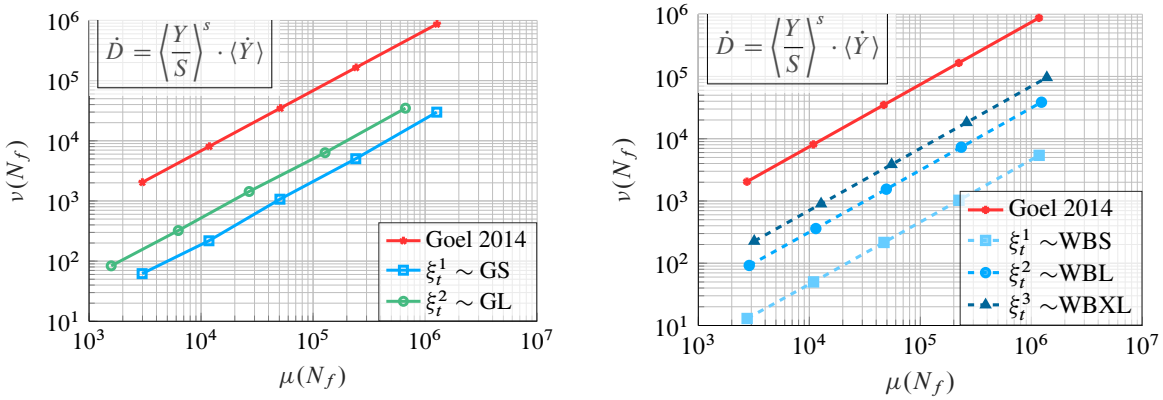


(a) Gaussian with filtering (b) shifted Weibull

Figure 8.16: Comparison of statistics on the fatigue life computed from five loading levels using the Weibull and Gaussian random number

computed fatigue life agrees with the empirical result in the mean for all the levels. However, the bias in the vertical direction shows that the standard deviation of the simulation is approximately thirty times smaller than the experiment. It is expected to close this gap by increasing the randomness in the damage evolution, e.g. using random noise with larger variance. However, the variance of fatigue life with the GL random number can only be slightly improved, whereas its mean is significantly shifted. This outcome is consistent to the results shown in figs. 8.14b and 8.14d.

On the contrary, increasing the Weibull random number variance is able to continuously enlarge the fatigue uncertainty without introducing obvious bias in the fatigue mean (see fig. 8.16b). Indeed, the Weibull distribution, WBXL, with an extra-large (XL) variance $\nu^2 = 20^2$ is further implemented. Compared to the WBL, WBXL introduces approximately doubled standard deviation in the fatigue life. Theoretically, it is possible to meet the empirical relation by further enlarging the Weibull variance. In practice, it is difficult to converge to the empirical data, possibly due to two reasons. First, generating accurate Pseudo random variables with a small mean, e.g. $\mu = 1$, and a large variance, is difficult for modern computers [147]. Second, it is a variance reducing procedure to obtain the element-wise damage value by averaging the solution at the integration points [148]. The results can be improved by obtaining the fatigue life at the weakest Gauss point. Nevertheless, the empirical relation can be inaccurate due to poorly estimated parameters, as for each load level, only 13 experimental results are given [17].

**Reproduction of the P-S-N diagram** As stated in the introduction, it is desired to reproduce the fatigue diagram, including probabilistic information, for reliability analyses. With sufficient fatigue samples, the estimated probabilistic density function $f(N_f, L_s)$ can be obtained for each load levels. Numerically, by refining the number of loading levels from 5 to 1000 in the interval $L_s = [0.7, 0.9]$, and applying uniform discretisation of the variable $N_f = [3 \times 10^3, 2 \times 10^6]$, it is possible to have the approximated value of $f(N_f, L_s)$ as gridded data. After implementing the classical bilinear interpolation, the S-N relation with probabilistic information is illustrated as a P-S-N diagram in fig. 8.17a. The fatigue mean and the 95% confident interval for each load levels are plotted in lines. Figure 8.17b is a visualisation of the three-dimensional P-S-N surface. For example, the projection at northeast is the approximated probability density of loading level while taking $N_f = 10^3$ as the designing target.

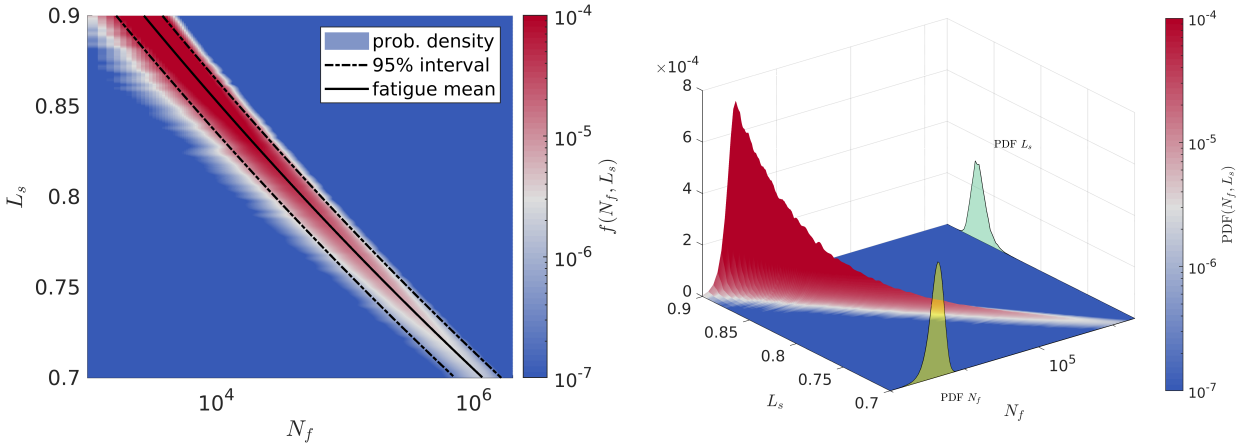


(a) (b)

Figure 8.17: Reproduced probabilistic S-N relation

# Conclusion and Remarks

In this work, a stochastic process inspired phenomenological approach is developed to simulate the uncertain damage evolution during the material fatigue process. In the framework of continuum damage mechanics, the deterministic damage evolution is modified as a stochastic differential equation. Many numerical investigations show that the proposed model can reproduce highly accurate virtual fatigue data for concrete structure up to the high-cycle regime. Compared to previous researches, the highlights of this study are:

- The model applicability is verified on the four-point flexural fatigue problem via finite element analysis.
- Particular attention is paid to evaluating random damage increments to ensure the consistency of thermodynamic principles. Through generating random variables from a uniquely designed positive distribution, the solution is statistically unbiased to the deterministic evolution law.

Since the accumulation of brittle damage has a significant role in the fatigue failure of concrete material, a deterministic quasi-brittle damage law is newly developed with the main purpose to capture the unilateral effect. While designing this model, a large number of modelling concepts are reviewed. The controlling factor of damage evolution is assigned to the damage conjugated thermodynamic force, i.e. the elastic energy release rate, neither the stress nor the strain. This study uses a specific parameter to adjust the contribution of the deviatoric and hydrostatic components in the damage driving thermodynamic force, without introducing extra damage variables or using high-order damage tensors. For the specified flexural problem, damage under shear and compression is largely reduced to represent the main damage form of the concrete beam in reality.

Several modelling approaches of damage uncertainty from literature are compared in this study. The phenomenological approach, which considers the damage evolution as a stochastic process, is CDM consistent. However, approaches based on micro-mechanics and statistics have difficulties to describe the transition between different scales. Another common weakness of these models is that they assume the macroscopic damage evolution law to be a cumulative distribution function, which is far from laboratory observations.

The empirical fatigue models are often used to describe the deterministic S-N relation with which fatigue life is derived as an explicit function of the external load. Besides, advanced models are developed to fit the distribution parameters of the empirical fatigue life. The empirical approaches in general have remarkable model simplicity. However, the description of the fundamental mechanism of uncertain fatigue damage evolution is often missing. The progressive approach, which models damage evolution by the physical law, has considerable flexibility in capturing the fatigue phenomenons, such as the frequency and loading ratio effect. Compared to the empirical

models, the progressive approach can produce similar deterministic S-N relation once the material parameters are adequately calibrated. Meanwhile, high-cycle fatigue computation can benefit from jumping-cycle algorithms. By comparing the difference of damage increments in two subsequent cycles, the second-order method shows a better balance between cost and accuracy.

The parameter study of the random damage model on a one dimensional problem shows that the classical Wiener process is not suitable for stochastic damage evolution. Indeed, the random increment has to be composed from coloured noises such as Weibull and truncated Gaussian. The statistical mean of the random damage paths can accurately approximate the deterministic solution, and the expansion of damage variance is sub-linear in time. The uncertainty in damage and fatigue life can be significantly enlarged while using the first-order jumping-cycle algorithm. In contrast, the high-order algorithm has convergence problem to extrapolate reasonable damage evolution samples. With calibrated parameters, the fatigue scatters reproduced from the simplified problem can fit closely to the experimental data. For other types of stochastic diffusions, e.g. non-proportional and its variations, their distributions are time-dependent and have correlation to the current drift value. The non-proportional diffusion cannot guarantee the mean of damage noise to be zero. However, it can introduce an extra frequency effect in the damage evolution.

The finite element solution on the four-point flexural fatigue problem is a systematic demonstration of the model capability both in the deterministic and stochastic computation. The accurately reproduced deterministic fatigue data indicates that the estimation of flexural fatigue life based on the damage value in the weakest finite element is applicable for brittle material. For the stochastic simulation, the main difficulty is to reproduced the fatigue variance. While using the Gaussian random number, a filtering process is needed, which shifts the fatigue evolution away from its deterministic low. This effect becomes evident with large noise variance. The Weibull random number, which is not designed to evaluate stochastic process by the mathematical definition, exhibits good simulation results.

Usually, it is difficult to approximate the fatigue life for a specified stress level on which the experimental data is not available. This study provides a new phenomenological approach in the CDM framework to predict the random fatigue behaviour. Based on the robust finite element method and limited fatigue samples, it is possible to obtain a wide range of S-N relation with accurate probabilistic descriptions. The framework of modifying deterministic evolution laws as a stochastic processes is very general because the material parameters can be directly adopted from classical solid mechanics. This modelling approach can be planted in advanced finite element methods to simulate complicated material behaviours including ductile, creep and large deformations. Since the reproduced fatigue data contain detailed information of the damage evolution and the simulation is considerably cheaper than traditional fatigue experiment, this study is helpful to data-driven modelling approaches, which rely on large amount of high-quality training data. In the future, it can be compared to the homogenised macroscopic solution from mesoscale approaches. Also, numerical simulation considering spatial correlation between random damage increments might be interesting. Since the classical MC method is computationally heavy, a multi-level MC method applied in the spatial and temporal domain can possibly reduce the cost.

# List of Literature

## References


[1] Jaap Schijve et al. *Fatigue of structures and materials*. Springer, 2001.

[2] Jean Lemaitre and Rodrigue Desmorat. *Engineering damage mechanics: ductile, creep, fatigue and brittle failures*. Springer Science & Business Media, 2005.

[3] Dimitrios G Pavlou. "The theory of the SN fatigue damage envelope: generalization of linear, double-linear, and non-linear fatigue damage models". In: *International Journal of Fatigue* 110 (2018), pp. 204–214.

[4] Nadja Oneschkow. "Fatigue behaviour of high-strength concrete with respect to strain and stiffness". In: *International Journal of Fatigue* 87 (2016), pp. 38–49.

[5] Rodrigue Desmorat et al. "Two scale damage model and related numerical issues for thermo-mechanical high cycle fatigue". In: *European Journal of Mechanics-A/Solids* 26.6 (2007), pp. 909–935.

[6] Mainak Bhattacharyya et al. "A LATIN-PGD model reduction approach for the simulation of fatigue damage". In: *COMPLAS 2017-XIV International Conference on Computational Plasticty, Barcelona, Spain*. 2017.

[7] Peter Heek and Peter Mark. "Multiaxial and variable amplitude fatigue of concrete". In: *Civil Engineering Design* 1.3-4 (2019), pp. 87–96.

[8] Rodrigue Desmorat. "Anisotropic damage modeling of concrete materials". In: *International Journal of Damage Mechanics* 25.6 (2016), pp. 818–852.

[9] Liang Zhang et al. "An anisotropic continuum damage model for high-cycle fatigue". In: *Mechanics of Advanced Materials and Structures* (2020), pp. 1–15.

[10] Jean Lemaitre and Jean-Louis Chaboche. *Mechanics of solid materials*. Cambridge university press, 1994.

[11] Vitaliy M Kindrachuk and Jörg F Unger. "A Fourier transformation-based temporal integration scheme for viscoplastic solids subjected to fatigue deterioration". In: *International Journal of Fatigue* 100 (2017), pp. 215–228.

[12] Mainak Bhattacharyya et al. "A kinetic two-scale damage model for high-cycle fatigue simulation using multi-temporal Latin framework". In: *European Journal of Mechanics-A/Solids* 77 (2019), p. 103808.

[13] Mainak Bhattacharyya et al. “A Model Reduction Technique in Space and Time for Fatigue Simulation”. In: *Multiscale Modeling of Heterogeneous Structures*. Springer, 2018, pp. 183–203.

[14] Shadi Alameddin et al. “Large time increment approach for fatigue damage computations”. In: *PAMM* 17.1 (2017), pp. 231–232.

[15] Byung Hwan Oh. “Fatigue analysis of plain concrete in flexure”. In: *Journal of Structural Engineering* 112.2 (1986), pp. 273–288.

[16] S Goel, SP Singh, and P Singh. “Flexural fatigue strength and failure probability of self compacting fibre reinforced concrete beams”. In: *Engineering Structures* 40 (2012), pp. 131–140.

[17] S Goel and SP Singh. “Fatigue performance of plain and steel fibre reinforced self compacting concrete using S–N relationship”. In: *Engineering Structures* 74 (2014), pp. 65–73.

[18] Enrique Castillo and Alfonso Fernández-Canteli. *A unified statistical methodology for modeling fatigue damage*. Springer Science & Business Media, 2009.

[19] Luis Saucedo et al. “A probabilistic fatigue model based on the initial distribution to consider frequency effect in plain and fiber reinforced concrete”. In: *International Journal of Fatigue* 48 (2013), pp. 308–318.

[20] Arthur Medeiros et al. “Effect of the loading frequency on the compressive fatigue behavior of plain and fiber reinforced concrete”. In: *International Journal of Fatigue* 70 (2015), pp. 342–350.

[21] José Ríos et al. “Probabilistic flexural fatigue in plain and fiber-reinforced concrete”. In: *Materials* 10.7 (2017), p. 767.

[22] Kazimierz Sobczyk and BF Spencer Jr. *Random fatigue: from data to theory*. Academic Press, 2012.

[23] CW Woo and DL Li. “A general stochastic dynamic model of continuum damage mechanics”. In: *International journal of solids and structures* 29.23 (1992), pp. 2921–2932.

[24] Vadim V Silberschmidt. “Dynamics of stochastic damage evolution”. In: *International Journal of Damage Mechanics* 7.1 (1998), pp. 84–98.

[25] B Bhattcharya and Bruce Ellingwood. *A damage mechanics based approach to structural deterioration and reliability*. Tech. rep. Nuclear Regulatory Commission, Washington, DC (United States). Div. of Engineering Technology; Oak Ridge National Lab., TN (United States); Johns Hopkins Univ., Baltimore, MD (United States). Dept. of Civil Engineering, 1998, 1998.

[26] Denis Breysse. “Probabilistic formulation of damage-evolution law of cementitious composites”. In: *Journal of engineering mechanics* 116.7 (1990), pp. 1489–1510.

[27] S Kandarpa, DJ Kirkner, and BF Spencer Jr. “Stochastic damage model for brittle materials subjected to monotonic loading”. In: *Journal of engineering mechanics* 122.8 (1996), pp. 788–795.

[28] W Li et al. "Effect of loading type on fatigue properties of high strength bearing steel in very high cycle regime". In: *Materials Science and Engineering: A* 528.15 (2011), pp. 5044–5052.

[29] Z Yu et al. "A simple damage model for concrete considering irreversible mode-II microcracks". In: *Fatigue & Fracture of Engineering Materials & Structures* 39.11 (2016), pp. 1419–1432.

[30] Decheng Feng, Xiaodan Ren, and Jie Li. "Stochastic damage hysteretic model for concrete based on micromechanical approach". In: *International Journal of Non-Linear Mechanics* 83 (2016), pp. 15–25.

[31] Vadim V Silberschmidt and Jean-Louis Chaboche. "Effect of stochasticity on the damage accumulation in solids". In: *International Journal of Damage Mechanics* 3.1 (1994), pp. 57–70.

[32] Peter E Kloeden and Eckhard Platen. *Numerical solution of stochastic differential equations*. Vol. 23. Springer Science & Business Media, 2013.

[33] Kazimierz Sobczyk. *Stochastic differential equations: with applications to physics and engineering*. Vol. 40. Springer Science & Business Media, 2013.

[34] Alexei Chechkin and Ilya Pavlyukevich. "Marcus versus Stratonovich for systems with jump noise". In: *Journal of Physics A: Mathematical and Theoretical* 47.34 (2014), p. 342001.

[35] Peter E Kloeden and Eckhard Platen. "Stratonovich and Itô stochastic taylor expansions". In: *Mathematische Nachrichten* 151.1 (1991), pp. 33–50.

[36] Peter E Kloeden and Eckhard Platen. "Higher-order implicit strong numerical schemes for stochastic differential equations". In: *Journal of statistical physics* 66.1-2 (1992), pp. 283–314.

[37] Pamela Marion Burrage. "Runge-Kutta methods for stochastic differential equations". In: (1999).

[38] Alka Chadha and Swaroop Nandan Bora. "Stability analysis for neutral stochastic differential equation of second order driven by Poisson jumps". In: *Journal of Mathematical Physics* 58.11 (2017), p. 112703.

[39] Maziar Raissi and George Em Karniadakis. "Hidden physics models: Machine learning of nonlinear partial differential equations". In: *Journal of Computational Physics* 357 (2018), pp. 125–141.

[40] Yoshihiro Saito and Taketomo Mitsui. "Stability analysis of numerical schemes for stochastic differential equations". In: *SIAM Journal on Numerical Analysis* 33.6 (1996), pp. 2254–2267.

[41] Desmond J Higham. "An algorithmic introduction to numerical simulation of stochastic differential equations". In: *SIAM review* 43.3 (2001), pp. 525–546.

[42] Desmond J Higham. "Mean-square and asymptotic stability of the stochastic theta method". In: *SIAM journal on numerical analysis* 38.3 (2000), pp. 753–769.

[43] Gunther Leobacher and Friedrich Pillichshammer. *Introduction to Quasi-Monte Carlo integration and applications*. Springer, 2014.

[44] Alexander Buchholz, Florian Wenzel, and Stephan Mandt. “Quasi-Monte-Carlo variational inference”. In: *arXiv preprint arXiv:1807.01604* (2018).

[45] Paul Glasserman. *Monte Carlo methods in financial engineering*. Vol. 53. Springer Science & Business Media, 2013.

[46] Pierre L’Ecuyer. “Quasi-Monte Carlo methods with applications in finance”. In: *Finance and Stochastics* 13.3 (2009), pp. 307–349.

[47] Damien Lamberton and Bernard Lapeyre. *Introduction to stochastic calculus applied to finance*. Chapman and Hall/CRC, 2011.

[48] Friedemann N Schietzold et al. “Development of fuzzy probability based random fields for the numerical structural design”. In: *GAMM-Mitteilungen* 42.1 (2019), e201900004.

[49] Sergei Kucherenko, Daniel Albrecht, and Andrea Saltelli. “Exploring multi-dimensional spaces: A comparison of Latin hypercube and quasi Monte Carlo sampling techniques”. In: *arXiv preprint arXiv:1505.02350* (2015).

[50] Mona M Dannert et al. “A probability-box approach on uncertain correlation lengths by stochastic finite element method”. In: *PAMM* 18.1 (2018), e201800114.

[51] Sebastian Fink and Udo Nackenhorst. “Simulation of Uncertain Inelastic Material Behaviour using the Stochastic Finite Element Method”. In: *PAMM* 14.1 (2014), pp. 265–266.

[52] Liam Comerford, Ioannis A Kougioumtzoglou, and Michael Beer. “On quantifying the uncertainty of stochastic process power spectrum estimates subject to missing data”. In: *International Journal of Sustainable Materials and Structural Systems* 2.1-2 (2015), pp. 185–206.

[53] Lazar M Kachanov. “Rupture time under creep conditions”. In: *International journal of fracture* 97.1 (1999), pp. 11–18.

[54] Jean Lemaitre. *A course on damage mechanics*. Springer Science & Business Media, 1986.

[55] Yu. N. Rabotnov, F. A. Leckie, and W. Prager. “Creep Problems in Structural Members”. In: *Journal of Applied Mechanics* 37.1 (1970), pp. 249–249.

[56] Sumio Murakami. *Continuum damage mechanics: a continuum mechanics approach to the analysis of damage and fracture*. Vol. 185. Springer Science & Business Media, 2012.

[57] Jean Lemaitre. “A continuous damage mechanics model for ductile fracture”. In: *Journal of engineering materials and technology* 107.1 (1985), pp. 83–89.

[58] Jean Lemaitre. “How to use damage mechanics”. In: *Nuclear engineering and design* 80.2 (1984), pp. 233–245.

[59] CL Chow and Y Wei. “A model of continuum damage mechanics for fatigue failure”. In: *International Journal of Fracture* 50.4 (1991), pp. 301–316.

[60] Jean-Louis Chaboche. “Constitutive equations for cyclic plasticity and cyclic viscoplasticity”. In: *International journal of plasticity* 5.3 (1989), pp. 247–302.

[61] Jacky Mazars and Gilles Pijaudier-Cabot. “Continuum damage theory—application to concrete”. In: *Journal of engineering mechanics* 115.2 (1989), pp. 345–365.

[62] JJ Marigo. “Modelling of brittle and fatigue damage for elastic material by growth of microvoids”. In: *Engineering Fracture Mechanics* 21.4 (1985), pp. 861–874.

[63] Abdenour Alliche. “Damage model for fatigue loading of concrete”. In: *International Journal of Fatigue* 26.9 (2004), pp. 915–921.

[64] R Desmorat, F Ragueneau, and H Pham. “Continuum damage mechanics for hysteresis and fatigue of quasi-brittle materials and structures”. In: *International journal for numerical and analytical methods in geomechanics* 31.2 (2007), pp. 307–329.

[65] Zdeněk P Bažant and Byung H Oh. “Crack band theory for fracture of concrete”. In: *Matériaux et construction* 16.3 (1983), pp. 155–177.

[66] J Lubliner et al. “A plastic-damage model for concrete”. In: *International Journal of Solids and Structures* 25.3 (1989), pp. 299–326.

[67] Zdeněk P Bažant and Jaime Planas. *Fracture and size effect in concrete and other quasibrittle materials*. Routledge, 2019.

[68] Dusan Krajcinovic and Manuel Americo G Silva. “Statistical aspects of the continuous damage theory”. In: *International Journal of Solids and Structures* 18.7 (1982), pp. 551–562.

[69] Jie Li and Xiaodan Ren. “Stochastic damage model for concrete based on energy equivalent strain”. In: *International Journal of Solids and Structures* 46.11-12 (2009), pp. 2407–2419.

[70] Abedulgader Baktheer and Rostislav Chudoba. “Classification and evaluation of phenomenological numerical models for concrete fatigue behavior under compression”. In: *Construction and Building Materials* 221 (2019), pp. 661–677.

[71] Michael N Fardis, Bunu Alibe, and John L Tassoulas. “Monotonic and cyclic constitutive law for concrete”. In: *Journal of engineering mechanics* 109.2 (1983), pp. 516–536.

[72] Anna Pandolfi and Alberto Taliercio. “Bounding surface models applied to fatigue of plain concrete”. In: *Journal of engineering Mechanics* 124.5 (1998), pp. 556–564.

[73] Junsong Liang, Xiaodan Ren, and Jie Li. “A competitive mechanism driven damage-plasticity model for fatigue behavior of concrete”. In: *International Journal of Damage Mechanics* 25.3 (2016), pp. 377–399.

[74] Jacky Mazars. “Application de la mécanique de l’endommagement au comportement non linéaire et à la rupture du béton de structure”. In: *These de Docteur es Sciences presentee a L’Universite Pierre et Marie Curie-Paris 6* (1984).

[75] Jacky Mazars. “A description of micro-and macroscale damage of concrete structures”. In: *Engineering Fracture Mechanics* 25.5-6 (1986), pp. 729–737.

[76] VA Lubarda, D Krajcinovic, and S Mastilovic. “Damage model for brittle elastic solids with unequal tensile and compressive strengths”. In: *Engineering Fracture Mechanics* 49.5 (1994), pp. 681–697.

[77] Enrico Papa and Alberto Taliercio. “Anisotropic damage model for the multiaxial static and fatigue behaviour of plain concrete”. In: *Engineering Fracture Mechanics* 55.2 (1996), pp. 163–179.

[78] Su Murakami and K Kamiya. “Constitutive and damage evolution equations of elastic-brittle materials based on irreversible thermodynamics”. In: *International Journal of Mechanical Sciences* 39.4 (1997), pp. 473–486.

[79] Rodrigue Desmorat, Fabrice Gatuingt, and Frédéric Ragueneau. “Nonlocal anisotropic damage model and related computational aspects for quasi-brittle materials”. In: *Engineering Fracture Mechanics* 74.10 (2007), pp. 1539–1560.

[80] JW Ju. “On energy-based coupled elastoplastic damage theories: constitutive modeling and computational aspects”. In: *International Journal of Solids and structures* 25.7 (1989), pp. 803–833.

[81] Jeeho Lee and Gregory L Fenves. “Plastic-damage model for cyclic loading of concrete structures”. In: *Journal of engineering mechanics* 124.8 (1998), pp. 892–900.

[82] André Hürkamp and Udo Nackenhorst. “A stochastic homogenization scheme for damaged composites”. In: *PAMM* 12.1 (2012), pp. 431–432.

[83] Artur Ganczarski and L Barwacz. “Low cycle fatigue based on unilateral damage evolution”. In: *International Journal of Damage Mechanics* 16.2 (2007), pp. 159–177.

[84] Rodrigue Desmorat and Sabine Cantournet. “Modeling microdefects closure effect with isotropic/anisotropic damage”. In: *International Journal of Damage Mechanics* 17.1 (2008), pp. 65–96.

[85] JP Cordebois and F Sidoroff. “Damage induced elastic anisotropy”. In: *Mechanical Behavior of Anisotropic Solids/Comportment Méchanique des Solides Anisotropes*. Springer, 1982, pp. 761–774.

[86] M Fassin et al. “An anisotropic damage and fracture model based on a second order damage tensor”. In: *Proceedings of the 6th European Conference on Computational Mechanics (ECCM 6)*. Glasgow United Kingdom. 2018.

[87] Pierre Ladeveze. “On an anisotropic damage theory”. In: *Proc. CNRS Int. Coll* 351 (1983), pp. 355–363.

[88] Jean Lemaitre, Rodrigue Desmorat, and Maxime Sauzay. “Anisotropic damage law of evolution”. In: *European Journal of Mechanics-A/Solids* 19.2 (2000), pp. 187–208.

[89] CL Chow and Y Wei. “Constitutive modeling of material damage for fatigue failure prediction”. In: *International Journal of Damage Mechanics* 8.4 (1999), pp. 355–375.

[90] P Ladeveze and J Lemaitre. “Damage effective stress in quasi unilateral conditions”. In: *16th International congress of theoretical and applied mechanics, Lyngby, Denmark*. 1984.

[91] Si Hai Mai et al. “A continuum damage modeling of quasi-static fatigue strength of plain concrete”. In: *International journal of fatigue* 37 (2012), pp. 79–85.

[92] Marek Fassin, Stephan Wulfinghoff, and Stefanie Reese. “A gradient-extended elastic isotropic damage model considering crack-closure”. In: *Proceedings of the 7th GACM Colloquium on Computational Mechanics for Young Scientists from Academia and Industry*. 2017, pp. 305–311.

[93] Jan Carmeliet and Hugo Hens. “Probabilistic nonlocal damage model for continua with random field properties”. In: *Journal of engineering mechanics* 120.10 (1994), pp. 2013–2027.

[94] W Zhang et al. “Stochastic Material Modeling for Fatigue Damage Analysis”. In: *Virtual Design and Validation*. Springer, 2020, pp. 329–347.

[95] Denis Breysse. “A probabilistic formulation of the damage evolution law”. In: *Structural safety* 8.1-4 (1990), pp. 311–325.

[96] Xiaodan Ren and Jie Li. “Hysteretic deteriorating model for quasi-brittle materials based on micromechanical damage approach”. In: *International Journal of Non-Linear Mechanics* 46.1 (2011), pp. 321–329.

[97] Alten F Grandt Jr. *Fundamentals of structural integrity: damage tolerant design and nondestructive evaluation*. John Wiley & Sons, 2003.

[98] MK Lee and BIG Barr. “An overview of the fatigue behaviour of plain and fibre reinforced concrete”. In: *Cement and Concrete Composites* 26.4 (2004), pp. 299–305.

[99] C Thomas et al. “Fatigue limit of recycled aggregate concrete”. In: *Construction and Building Materials* 52 (2014), pp. 146–154.

[100] Benard Isojeh, Maria El-Zeghayar, and Frank J Vecchio. “Fatigue behavior of steel fiber concrete in direct tension”. In: *Journal of Materials in Civil Engineering* 29.9 (2017), p. 04017130.

[101] Benard Isojeh, Maria El-Zeghayar, and Frank J Vecchio. “Concrete damage under fatigue loading in uniaxial compression”. In: *ACI Mater. J* 114.2 (2017), pp. 225–235.

[102] Ulrike Karr et al. “Very high cycle fatigue testing of concrete using ultrasonic cycling”. In: *Materials Testing* 59.5 (2017), pp. 438–444.

[103] Jesús Mínguez et al. “Plain and Fiber-Reinforced Concrete Subjected to Cyclic Compressive Loading: Study of the Mechanical Response and Correlations with Microstructure Using CT Scanning”. In: *Applied Sciences* 9.15 (2019), p. 3030.

[104] H Mayer. “Recent developments in ultrasonic fatigue”. In: *Fatigue & Fracture of Engineering Materials & Structures* 39.1 (2016), pp. 3–29.

[105] R Schuller et al. “VHCF properties of nitrided 18Ni maraging steel thin sheets with different Co and Ti content”. In: *Fatigue & Fracture of Engineering Materials & Structures* 38.5 (2015), pp. 518–527.

[106] Daniel Backe, Frank Balle, and Dietmar Eifler. “Fatigue testing of CFRP in the Very High Cycle Fatigue (VHCF) regime at ultrasonic frequencies”. In: *Composites Science and Technology* 106 (2015), pp. 93–99.

[107] Sebastian Schneider, Ralf Herrmann, and Steffen Marx. “Development of a resonant fatigue testing facility for large-scale beams in bending”. In: *International Journal of Fatigue* 113 (2018), pp. 171–183.

[108] J Mazars, Y Berthaud, and S Ramtani. “The unilateral behaviour of damaged concrete”. In: *Engineering Fracture Mechanics* 35.4-5 (1990), pp. 629–635.

[109] Joseph F Lamond and James H Pielert. “Significance of tests and properties of concrete and concrete-making materials”. In: ASTM West Conshohocken, PA, 2006.

[110] MA Rashid, MA Mansur, and P Paramasivam. "Correlations between mechanical properties of high-strength concrete". In: *Journal of Materials in Civil Engineering* 14.3 (2002), pp. 230–238.

[111] BW Xu and HS Shi. "Correlations among mechanical properties of steel fiber reinforced concrete". In: *Construction and Building Materials* 23.12 (2009), pp. 3468–3474.

[112] Xudong Chen, Shengxing Wu, and Jikai Zhou. "Influence of porosity on compressive and tensile strength of cement mortar". In: *Construction and Building Materials* 40 (2013), pp. 869–874.

[113] F Mujika et al. "Determination of tensile and compressive moduli by flexural tests". In: *Polymer testing* 25.6 (2006), pp. 766–771.

[114] F Mujika. "On the difference between flexural moduli obtained by three-point and four-point bending tests". In: *Polymer Testing* 25.2 (2006), pp. 214–220.

[115] J Fischer, B Stawarczyk, and CHF Hämmerle. "Flexural strength of veneering ceramics for zirconia". In: *journal of dentistry* 36.5 (2008), pp. 316–321.

[116] X Zhu, JW Jones, and JE Allison. "Effect of frequency, environment, and temperature on fatigue behavior of E319 cast-aluminum alloy: Small-crack propagation". In: *Metallurgical and Materials Transactions A* 39.11 (2008), pp. 2666–2680.

[117] X Zhu, JW Jones, and JE Allison. "Effect of frequency, environment, and temperature on fatigue behavior of E319 cast aluminum alloy: stress-controlled fatigue life response". In: *Metallurgical and Materials Transactions A* 39.11 (2008), pp. 2681–2688.

[118] Noriko Tsutsumi, Yukitaka Murakami, and Véronique Doquet. "Effect of test frequency on fatigue strength of low carbon steel". In: *Fatigue & Fracture of Engineering Materials & Structures* 32.6 (2009), pp. 473–483.

[119] Benjamin Guennec et al. "Effect of the loading frequency on fatigue properties of JIS S15C low carbon steel and some discussions based on micro-plasticity behavior". In: *International Journal of Fatigue* 66 (2014), pp. 29–38.

[120] Y Furuya. "Effect of Frequency on Giga-Cycle Fatigue Properties for Low-temperature-Temperes SNCM439 Steel". In: *Transactions of the Japan Society of Mechanical Engineers, Series A* 68.667 (2002), pp. 447–483.

[121] Aiguo Zhao et al. "Effects of strength level and loading frequency on very-high-cycle fatigue behavior for a bearing steel". In: *International journal of Fatigue* 38 (2012), pp. 46–56.

[122] RJ Morrissey, DL McDowell, and T Nicholas. "Frequency and stress ratio effects in high cycle fatigue of Ti-6Al-4V". In: *International Journal of Fatigue* 21.7 (1999), pp. 679–685.

[123] O Graf and E Brenner. "Experiments for investigating the resistance of concrete under often repeated compression loads". In: *Bulletin* 1 (1934), pp. 17–25.

[124] John Washburn Murdock. *A critical review of research on fatigue of plain concrete*. Tech. rep. University of Illinois at Urbana Champaign, College of Engineering, 1965.

[125] Helmut Weigler and Werner Freitag. *Dauerschwell-und Betriebsfestigkeit von Konstruktions-Leichtbeton.* Ernst, 1975.

[126] Dietmar Klausen. *Festigkeit und Schädigung von Beton bei häufig wiederholter Beanspruchung*. Technische Hochschule Darmstadt, 1978.

[127] A Jansen. "Research to fatigue behaviour of topping on prefabricated concrete girders". PhD thesis. Master thesis, Delft University of Technology, 1996, 128 p. (in Dutch), 1996.

[128] R Al-Rousan and M Issa. "Fatigue performance of reinforced concrete beams strengthened with CFRP sheets". In: *Construction and Building Materials* 25.8 (2011), pp. 3520–3529.

[129] Sumit Arora and Surinder Pal Singh. "Fatigue strength and failure probability of concrete made with RCA". In: *Magazine of Concrete Research* 69.2 (2016), pp. 55–67.

[130] Theodore Nicholas. *High cycle fatigue: a mechanics of materials perspective*. Elsevier, 2006.

[131] Herbert J Sutherland and John F Mandell. "Optimized constant-life diagram for the analysis of fiberglass composites used in wind turbine blades". In: *Journal of solar energy engineering* 127.4 (2005), pp. 563–569.

[132] M Kawai and M Koizumi. "Nonlinear constant fatigue life diagrams for carbon/epoxy laminates at room temperature". In: *Composites Part A: Applied Science and Manufacturing* 38.11 (2007), pp. 2342–2353.

[133] Anastasios P Vassilopoulos, Behzad D Manshadi, and Thomas Keller. "Influence of the constant life diagram formulation on the fatigue life prediction of composite materials". In: *International journal of fatigue* 32.4 (2010), pp. 659–669.

[134] Anastasios P Vassilopoulos. *Fatigue life prediction of composites and composite structures*. Woodhead, 2019.

[135] Knut Aas-Jakobsen. *Fatigue of concrete beams and columns*. Division of Concrete Struc. Norwegian Institute of Technology, 1970.

[136] B Zhang, DV Phillips, and K Wu. "Effects of loading frequency and stress reversal on fatigue life of plain concrete". In: *Magazine of concrete research* 48.177 (1996), pp. 361–375.

[137] Peiyin Lü, Qingbin Li, and Yupu Song. "Damage constitutive of concrete under uniaxial alternate tension–compression fatigue loading based on double bounding surfaces". In: *International journal of solids and structures* 41.11-12 (2004), pp. 3151–3166.

[138] Thomas TC Hsu. "Fatigue of plain concrete". In: *Journal Proceedings*. Vol. 78. 4. 1981, pp. 292–305.

[139] EJ Gumbel. "Parameters in the distribution of fatigue life". In: *Journal of the Engineering Mechanics Division* 89.5 (1963), pp. 45–64.

[140] SP Singh and SK Kaushik. "Flexural fatigue analysis of steel fiber-reinforced concrete". In: *Materials Journal* 98.4 (2001), pp. 306–312.

[141] Kyriaki Corinna Datsiou and Mauro Overend. "Weibull parameter estimation and goodness-of-fit for glass strength data". In: *Structural Safety* 73 (2018), pp. 29–41.

[142] D Cojocaru and Anette M Karlsson. "A simple numerical method of cycle jumps for cyclically loaded structures". In: *International Journal of fatigue* 28.12 (2006), pp. 1677–1689.

[143] Fabio Biondini and Dan M Frangopol. *Bridge Maintenance, Safety, Management, Resilience and Sustainability: Proceedings of the Sixth International IABMAS Conference, Stresa, Lake Maggiore, Italy, 8-12 July 2012*. CRC Press, 2012.

[144] Eduardo A de Souza Neto, Djordje Peric, and David RJ Owen. *Computational methods for plasticity: theory and applications*. John Wiley & Sons, 2011.

[145] Tianhai Tian and Kevin Burrage. "Implicit Taylor methods for stiff stochastic differential equations". In: *Applied Numerical Mathematics* 38.1-2 (2001), pp. 167–185.

[146] Makoto Matsumoto and Takuji Nishimura. "Dynamic creation of pseudorandom number generators". In: *Monte-Carlo and Quasi-Monte Carlo Methods 1998*. Springer, 2000, pp. 56–69.

[147] William L Dunn and J Kenneth Shultis. *Exploring monte carlo methods*. Elsevier, 2011.

[148] Vissarion Papadopoulos and Dimitris G Giovanis. *Stochastic Finite Element Methods: An Introduction*. Springer, 2017.

# Curriculum Vitae

**Personal Information**

Weiran Zhang
born on March 8th, 1991 in Henan, P.R.C.

**School Education**

| | |
|---|---|
| 09.1997-06.2002 | Primary School Zhengyang |
| 09.2002-06.2005 | Middle School Zhengyang |
| 09.2005-06.2008 | High School Luoshan |
| 09.2008-06.2009 | High School Zhengyang |

**University Education**

| | |
|---|---|
| 09.2009-06.2013 | Bachelor: Quality and Reliability Engineering<br>Zhengzhou Institute of Aeronautical Industry Management |
| 10.2013-05.2016 | Master: Computational Sciences in Engineering<br>Technical University of Braunschweig |

**Professional Experience**

| | |
|---|---|
| 11.2016-10.2019 | Research assistant at Institute of Mechanics and Computational Mechanics, Leibniz University Hannover |

Hannover, July 2021

# Research and Seminar Reports

**Institut für Baumechanik und Numerische Mechanik**
**Gottfried Wilhelm Leibniz Universität Hannover**

Reports that have been published so far:

S 73/1 Seminar über Thermodynamik und Kontinuumsmechanik, Hannover 1973.

F 75/1 "Die Spannungsberechnung im Rahmen der Finite-Element-Methode", R. Ahmad, Dissertation, April 1975.

F 76/1 "Zur Theorie und Anwendung der Stoffgleichungen elastisch-plastisch- viskoser Werkstoffe", H. Mentlein, Dissertation, April 1976.

F 77/1 Seminar über lineare und geometrisch nichtlineare Schalentheorie einschließlich Stabilitätstheorie, Hannover 1978.

F 77/2 "Beitrag zur Berechnung von Gründungsplatten mit Hilfe der Finite- Element-Methode", H. Meyer, Dissertation, Juli 1977.

F 77/3 "Zur Berechnung der Eigenfrequenzen und Eigenschwingungsformen räumlich vorgekrümmter und vorverwundener Stäbe" J. Möhlenkamp, Dissertation, Dezember 1977.

F 77/4 "Zur Theorie und Berechnung geometrisch und physikalisch nichtlinearer Kontinua mit Anwendung der Methode der finiten Elemente", J. Paulun, Dissertation, Dezember 1977.

F 78/1 2. Seminar über Thermodynamik und Kontinuumsmechanik, Hannover 1978.

F 79/1 "Theoretische und numerische Behandlung geometrisch nichtlinearer viskoplastischer Kontinua", K.-D. Klee, Dissertation, Februar 1979.

F 79/2 "Zur Konstruierbarkeit von Variationsfunktionalen für nichtlineare Probleme der Kontinuumsmechanik", J. Siefer, Dissertation, Oktober 1979.

F 80/1 "Theoretische und numerische Behandlung gerader Stäbe mit endlichen Drehungen", M. Kessel, Dissertation, Februar 1980.

F 81/1 "Zur Berechnung von Kontakt- und Stoßproblemen elastischer Körper mit Hilfe der Finite-Element-Methode", P. Wriggers, Dissertation, Januar 1981.95

F 81/2 “Stoffgleichungen für Steinsalze unter mechanischer und thermischer Beanspruchung”, J. Olschewski, E. Stein, W. Wagner, D. Wetjen, geänderte Fassung eines Zwischenberichtes zum BMFT-Forschungsvorhaben KWA 1608/5.

F 82/1 “Konvergenz und Fehlerabschätzung bei der Methode der Finiten Elemente”, R. Rohrbach, E. Stein, Abschlußbericht eines VW- Forschungsvorhabens, Februar 1982.

F 82/2 “Alternative Spannungsberechnung in Finite-Element- Verschiebungsmodellen”, C. Klöhn, Dissertation, November 1982

F 83/1 Seminar über nichtlineare Stabtheorie, Hannover 1983.

F 83/2 “Beiträge zur nichtlinearen Theorie und inkrementellen Finite- Element-Berechnung dünner elastischer Schalen”, A. Berg, Dissertation, Juli 1983.

F 83/3 “Elastoplastische Plattenbiegung bei kleinen Verzerrungen und großen Drehungen”, J. Paulun, Habilitation, September 1983.

F 83/4 “Geometrisch nichtlineare FE-Berechnung von Faltwerken mit plastisch / viskoplastischem Deformationsverhalten”, M. Krog, Dissertation, Dezember 1983.

F 85/1 Verleihung der Ehrendoktorwürde des Fachbereichs Bauingenieur- und Vermessungswesen der Universität Hannover an die Herren Prof. Dr. Drs. h.c. J.H. Argyris, Dr.-Ing. H. Wittmeyer.

F 85/2 “Eine geometrisch nichtlineare Theorie schubelastischer Schalen mit Anwendung auf Finite-Element-Berechnungen von Durchschlag- und Kontaktproblemen”, W. Wagner, Dissertation, März 1985.

F 85/3 “Geometrisch/physikalisch nichtlineare Probleme - Struktur und Algorithmen - ”, GAMM-Seminar im Februar 1985 in Hannover.

F 87/1 “Finite-Elemente-Berechnungen ebener Stabtragwerke mit Fließgelenken und großen Verschiebungen”, R. Kahn, Dissertation, Oktober 1987.

F 88/1 “Theorie und Numerik schubelastischer Schalen mit endlichen Drehungen unter Verwendung der Biot-Spannungen”, F. Gruttmann, Dissertation, Juni 1988.

F 88/2 “Optimale Formgebung von Stabtragwerken mit Nichtlinearitäten in der Zielfunktion und in den Restriktionen unter Verwendung der Finite-Element-Methode”, V.Berkhahn, Dissertation, Oktober 1988.

F 88/3 “Beiträge zur Theorie und Numerik großer plastischer und kleiner elastischer Deformationen mit Schädigungseinfluß”, R. Lammering, Dissertation, November 1988.

F 88/4 “Konsistente Linearisierungen in der Kontinuumsmechanik und ihrer Anwendung auf die Finite-Elemente-Methode”, P. Wriggers, Habilitation, November 1988.96

F 88/5 “Mathematische Formulierung und numerische Methoden für Kontaktprobleme auf der Grundlage von Extremalprinzipien”, D. Bischoff, Habilitation, Dezember 1988.

F 88/6 “Zur numerischen Behandlung thermomechanischer Prozesse”, C. Miehe, Dissertation, Dezember 1988.

F 89/1 “Zur Stabilität und Konvergenz gemischter finiter Elemente in der linearen Elastizitätstheorie”, R. Rolfes, Dissertation, Juni 1989.

F 89/2 “Traglastberechnungen von Faltwerken mit elastoplastischen Deformationen”, K.-H. Lambertz, Dissertation, November 1989.

F 89/3 “Transientes Kriechen und Kriechbruch im Steinsalz”, U. Heemann, Dissertation, November 1989.

F 89/4 “Materialgesetze zum Verhalten von Betonkonstruktionen bei harten Stößen”, E. Stein, P. Wriggers, T. Vu Van & T. Wedemeier, Dezember 1989.

F 89/5 “Lineare Konstruktion und Anwendungen von Begleitmatrizen”, C. Carstensen, Dissertation, Dezember 1989.

F 90/1 “Zur Berechnung prismatischer Stahlbetonbalken mit verschiedenen Querschnittformen für allgemeine Beanspruchungen”, H. N. Lucero-Cimas, Dissertation, April 1990.

F 90/2 “Zur Behandlung von Stoß- Kontaktproblemen mit Reibung unter Verwendung der Finite-Element-Methode”, T. Vu Van, Dissertation, Juni 1990.

F 90/3 “Netzadaption und Mehrgitterverfahren für die numerische Behandlung von Faltwerken”, L. Plank, Dissertation, September 1990.

F 90/4 “Beiträge zur Theorie und Numerik finiter inelastischer Deformationen”, N. Müller-Hoeppe, Dissertation, Oktober 1990.

F 90/5 “Beiträge zur Theorie und Numerik von Materialien mit innerer Reibung am Beispiel des Werkstoffes Beton”, T. Wedemeier, Dissertation, Oktober 1990.

F 91/1 “Zur Behandlung von Stabilitätsproblemen der Elastostatik mit der Methode der Finiten Elemente”, W. Wagner, Habilitation, April 1991.

F 91/2 “Mehrgitterverfahren und Netzadaption für lineare und nichtlineare statische Finite-Elemente-Berechnungen von Flächentragwerken”, W. Rust, Dissertation, Oktober 1991.

F 91/3 “Finite Elemente Formulierung im Trefftzschen Sinne für dreidimensionale anisotrop-elastische Faserverbundstrukturen”, K. Peters, Dissertation, Dezember 1991.

F 92/1 “Einspielen und dessen numerische Behandlung von Flächentragwerken aus ideal plastischem bzw. kinematisch verfestigendem Material”, G. Zhang, Dissertation, Februar 1992.97

F 92/2 “Strukturoptimierung stabilitätsgefährdeter Systeme mittels analytischer Gradientenermittlung”, A. Becker, Dissertation, April 1992.

F 92/3 “Duale Methoden für nichtlineare Optimierungsprobleme in der Strukturmechanik”, R. Mahnken, Dissertation, April 1992.

F 93/1 “Kanonische Modelle multiplikativer Elasto-Plastizität. Thermodynamische Formulierung und numerische Implementation”, C. Miehe, Habilitation, Dezember 1993.

F 93/2 “Theorie und Numerik zur Berechnung und Optimierung von Strukturen aus isotropen, hyperelastischen Materialien”, F.-J. Barthold, Dissertation, Dezember 1993.

F 94/1 “Adaptive Verfeinerung von Finite-Element-Netzen für Stabilitätsprobleme von Fläschentragwerken”, E. Stein, B. Seifert, W. Rust, Forschungsbericht, Oktober 1994.

F 95/1 “Adaptive Verfahren für die Formoptimierung von Flächentragwerken unter Berücksichtigung der CAD-FEM-Kopplung”, A. Falk, Dissertation, Juni 1995.

F 96/1 “Theorie und Numerik dünnwandiger Faserverbundstrukturen”, F. Gruttmann, Habilitation, Januar 1996.

F 96/2 “Zur Theorie und Numerik finiter elastoplastischer Deformationen von Schalenstrukturen”, B. Seifert, Dissertation, März 1996.

F 96/3 “Theoretische und algorithmische Konzepte zur phänomenologischen Beschreibung anisotropen Materialverhaltens”, J. Schröder, Dissertation, März 1996.

F 96/4 “Statische und dynamische Berechnungen von Schalen endlicher elastischer Deformationen mit gemischten finiten Elementen”, P. Betsch, Dissertation, März 1996.

F 96/5 “Kopplung von Finiten Elementen und Randelementen für ebene Elastoplastizität mit Impelementierung auf Parallelrechnern”, M. Kreienmeyer, Dissertation, März 1996.

F 96/6 “Theorie und Numerik dimensions- und modeladaptiver Finite- Elemente-Methoden von Fläschentragwerken”, S. Ohnimus, Dissertation, Juni 1996.

F 96/7 “Adaptive Finite Elemente Methoden für MIMD-Parallelrechner zur Behandlung von Strukturproblemen mit Anwendung auf Stabilitätsprobleme”, O. Klaas, Dissertation, Juli 1996.

F 96/8 “Institutsbericht 1971-1996 aus Anlaß des 25-jährigen Dienstjubiläums von Prof. Dr.-Ing. Dr.-Ing. E.h. Dr. h.c. mult. Erwin Stein”, Dezember 1996.

F 97/1 “Modellierung und Numerik duktiler kristalliner Werkstoffe”, P. Steinmann, Habilitation, August 1997.

F 97/2 “Formoptimierung in der Strukturdynamik”, L. Meyer, Dissertation, September 1997.98

F 97/3 “Modellbildung und Numerik für Versagensprozesse in Gründungen von Caisonwellenbrechern”, M. Lengnick, Dissertation, November 1997.

F 98/1 “Adaptive gemischte finite Elemente in der nichtlinearen Elastostatik und deren Kopplung mit Randelementen”, U. Brink, Dissertation, Februar 1998.

F 98/2 “Theoretische und numerische Aspekte zur Parameteridentifikation und Modellierung bei metallischen Werkstoffen”, R. Mahnken, Habilitation, Juli 1998.

F 98/3 “Lokalisierung und Stabilität der Deformation wassergesättigter bindiger und granularer Böden”, J. M. Panesso, Dissertation, August 1998.

F 98/4 “Theoretische und numerische Methoden in der angewandten Mechanik mit Praxisbeispielen”, R. Mahnken (Hrsg.), Festschrift anlässlich der Emeritierung von Prof. Dr.-Ing. Dr.-Ing. E.h. h.c. mult. Erwin Stein, November 1998.

F 99/1 “Eine h-adaptive Finite-Element-Methode für elasto-plastische Schalenproblem in unilateralem Kontakt”, C.-S. Han, Dissertation, Juli 1999.

F 00/1 “Ein diskontinuierliches Finite-Element-Modell für Lokalisierungsversagen in metallischen und granularen Materialien”, C. Leppin, Dissertation, März 2000.

F 00/2 “Untersuchungen von Strömungen in zeitlich veränderlichen Gebieten mit der Methode der Finiten Elementen”, H. Braess, Dissertation, März 2000.

F 00/3 “Theoretische und algorithmische Beiträge zur Berechnung von Faserverbundschalen”, J. Tessmer, Dissertation, März 2000.

F 00/4 “Theorie und Finite-Element-Methode für die Schädigungsbeschreibung in Beton und Stahlbeton”, D. Tikhomirov, Dissertation, August 2000.

F 01/1 “A C1 - continuous formulation for finite deformation contact”, L. Krstulovic-Opara, Dissertation, Januar 2001.

F 01/2 “Strain Localisation Analysis for Fully and Partially Saturated Geomaterials”, H. Zhang, Dissertation, Januar 2001.

F 01/3 “Meso-makromechanische Modellierung von Faserverbundwerkstoffen mit Schädigung”, C. Döbert, Dissertation, April 2001.

F 01/4 “Thermomechanische Modellierung gummiartiger Polymerstrukturen”, S. Reese, Habilitation, April 2001.

F 01/5 “Thermomechanisches Verhalten von Gummimaterialien während der Vulkanisation - Theorie und Numerik -”, M. Andre, Dissertation, April 2001.

F 01/6 “Adaptive FEM für elastoplastische Deformationen - Algorithmen und Visualisierung”, M. Schmidt, Dissertation, Juni 2001.

F 01/7 “Verteilte Algorithmen für h-, p- und d-adaptive Berechnungen in der nichtlinearen Strukturmechanik”, R. Niekamp, Dissertation, Juni 2001.99

F 01/8 “Theorie und Numerik zur Berechnung und Optimierung von Strukturen mit elastoplastischen Deformationen”, K. Wiechmann, Dissertation, Juli 2001.

F 01/9 “Direct Computation of Instability Points with Inequality using the Finite Element Method”, H. Tschöpe, Dissertation, September 2001.

F 01/10 “Theorie und Numerik residualer Fehlerschätzer für die Finite- Elemente-Methode unter Verwendung äquilibrierter Randspannungen”, S. Ohnimus, Habilitation, September 2001.

F 02/1 “Adaptive Algorithmen für thermo-mechanisch gekoppelte Kontaktprobleme”, A. Rieger, Dissertation, August 2002.

F 02/2 “Consistent coupling of shell- and beam-models for thermo-elastic problems”, K.Chavan, Dissertation, September 2002.

F 03/1 “Error-controlled adaptive finite element methods in large strain hyperelasticity and fracture mechanics”, M. Rüter, Dissertation, Mai 2003.

F 03/2 “Formulierung und Simulation der Kontaktvorgänge in der Baugrund- Tragwerks-Interaktion”, A. Haraldsson, Dissertation, Juni 2003.

F 03/3 “Concepts for Nonlinear Orthotropic Material Modeling with Applications to Membrane Structures”, T. Raible, Dissertation, Juni 2003.

F 04/1 “On Single- and Multi-Material arbitrary Lagrangian-Eulerian Approaches with Application to Micromechanical Problems at Finite Deformations”, D. Freßmann, Dissertation, Oktober 2004.

F 04/2 “Computational Homogenization of Microheterogeneous Materials at Finite Strains Including Damage”, S. Löhnert, Dissertation, Oktober 2004.

F 05/1 “Numerical Micro-Meso Modeling of Mechanosensation driven Osteonal Remodeling in Cortical Bone”, C. Lenz, Dissertation, Juli 2005.

F 05/2 “Mortar Type Methods Applied to Nonlinear Contact Mechanics”, K.A. Fischer, Dissertation, Juli 2005.

F 05/3 “Models, Algorithms and Software Concepts for Contact and Fragmentation in Computational Solid Mechanics”, C. Hahn, Dissertation, November 2005.

F 06/1 “Computational Homogenization of Concrete”, S. Moftah, Dissertation, Januar 2006.

F 06/2 “Reduction Methods in Finite Element Analysis of Nonlinear Structural Dynamics”, H. Spiess, Dissertation, Februar 2006.

F 06/3 “Theoretische und algorithmische Konzepte zur Beschreibung des beanspruchungsadaptiven Knochenwachstums”, B. Ebbecke, Dissertation, März 2006.100

F 06/4 “Experimentelle Untersuchungen an elastomeren Werkstoffen”, M. Dämgen, Dissertation, Dezember 2006.

F 07/1 “Numerische Konzepte zur Behandlung inelastischer Effekte beim reibungsbehafteten Rollkontakt”, M. Ziefle, Dissertation, Februar 2007.

F 07/2 “Begleitbuch zur Leibniz-Ausstellung”, Hrsg: E. Stein, P. Wriggers, 2007.

F 07/3 “Modellierung und Simulation der hochfrequenten Dynamik rollender Reifen”, M. Brinkmeier, Dissertation, Juni 2007.

F 07/4 “Computational Homogenization of micro-structural Damage due to Frost in Hardened Cement Paste”, M. Hain, Dissertation, Juli 2007.

F 07/5 “Elektromechanisch gekoppelte Kontaktmodellierung auf Mikroebene”, T. Helmich, Dissertation, August 2007.

F 07/6 “Dreidimensionales Diskretes Elemente Modell für Superellipsoide”, C. Lillie, Dissertation, Oktober 2007.

F 07/7 “Adaptive Methods for Continuous and Discontinuous Damage Modeling in Fracturing Solids”, S.H. Reese, Dissertation, Oktober 2007.

F 08/1 “Student Projects of Micromechanics”, Hrsg: U. Nackenhorst, August 2008.

F 09/1 “Theory and Computation of Mono- and Poly- crystalline Cyclic Martensitic Phase Transformations”, G. Sagar, Dissertation, August 2009.

F 09/2 “Student projects of Micromechanics”, D. Balzani and U. Nackenhorst, Course Volume, Oktober 2009.

F 09/3 “Multiscale Coupling based on the Quasicontinuum Framework, with Application to Contact Problems”, W. Shan, Dissertation, November 2009.

F 10/1 “A Multiscale Computational Approach for Microcrack Evolution in Cortical Bone and Related Mechanical Stimulation of Bone Cells”, D. Kardas, Dissertation, September 2010.

F 11/1 “Ein Integrales Modellierungskonzept zur numerischen Simulation der Osseointegration und Langzeitstabilität von Endoprothesen”, A.Lutz, Dissertation, Oktober 2011.

F 12/1 “Ein physikalisch motiviertes Reifen-Fahrbahnmodell für die Gesamtfahrzeugsimulation”, R. Chiarello, Dissertation, Februar 2012.

F 13/1 “Thermomechanical Analysis of Tire Rubber Compounds in Rolling Contact”, A.Suwannachit, Dissertation, September 2012.

F 13/2 “Towards a Finite Element Model for Fluid Flow in the Human Hip Joint”, K. Fietz, Dissertation, September 2013.101

F 14/1 “Micro-Mechanically Based Damage Analysis of Ultra High Performance Fibre Reinforced Concrete Structures with Uncertainties”, A. Hürkamp, Dissertation, Dezember 2013.

F 14/2 “Numerical Solution of High-Dimensional Fokker-Planck Equations with Discontinuous Galerkin Methods”, F. Loerke, Dissertation, Dezember 2013.

F 14/3 “Numerische Simulation probabilistischer Schädigungsmodelle mit der Stochastischen Finite Elemente Methode”, P. Jablonski, Dissertation, September 2014.

F 15/1 “On a Finite Element Approach for the Solution of a Mechanically Stimulated Biochemical Fracture Healing Model”, A. Sapotnick, Dissertation, November 2015.

F 15/2 “Simulation of Elastic-Plastic Material Behaviour with Uncertain Material Parameters. A Spectral Stochastic Finite Element Method Approach”, S. Fink, Dissertation, November 2015.

F 15/3 “A Fully Micro-mechanically Motivated Material Law for Filled Elastomer”, O. Stegen, Dissertation, Februar 2016.

F 16/1 “A modified adaptive harmony search algorithm approach on structural identification and damage detection”, M.Jahjouh, Dissertation, Januar 2016,

F17/1 “Computation Simulation of Piezo-electrically Stimulated Bone Adaption Surrounding Activated Teeth Implants”, A.Shirazibeheshtiha, Dissertation, Januar 2017.

F 17/2 “A Constitutive Contact Model for Homogenized Tread-Road Interaction in Rolling Resistance Computations”, R.Bayer, Dissertation, Februar 2017.

F 17/3 “A Posteriori Error Estimates for Advanced Galerkin Methods”, M.O. Rüter, Habilitation, November 2017.

F 17/4 “Probabilistische Finite Element Modellierung des mechanischem Materialverhaltens von Salzgestein”, M. Grehn, Dissertation, Dezember 2017.

F 18/1 “Modelling and numerical simulation for the prediction of the fatigue strength of airsprings”, N.K.Jha, Dissertation, März 2018.

F 18/2 “A model reduction approach in space and time for fatigue damage simulation”, M.Bhattacharya, Dissertation, Mai 2018.

F 18/3 “Numerical investigation on hydrogen embrittlement of metallic pipeline structures”, M.Möhle, Dissertation, Mai 2018.

F 18/5 “A stochastic fatigue model for casted aluminium structures", Govindarajan Narayanan, Dissertation, August 2018.

F 20/01 “A Micro-mechanically Motivated Approach for Modelling the Oxidative Aging Process of Elastomers", Darcy Beurle, Dissertation, December 2019.

F 20/02 “A Semi-incremental Model Order Reduction Approach for Fatigue Damage Computations", Shadi Alameddin, Dissertation, January 2020.

F 20/03 “A Coupled ALE Lagrangian Approach for the Simulation of Treaded Tires", Thirumal Alagu Palanichamy, Dissertation, August 2020.

F 21/01 “A parametric modeling concept for predicting biomechanical compatibility in total hip arthroplasty", Maximilian Bittens, Dissertation, July 2021.

F 21/02 “Stochastic Modelling and Numerical Simulation of Fatigue Damage", Weiran Zhang, Dissertation, July 2021.

In continuum damage mechanics, fatigue is a phenomenon associated with a continuous material stiffness reduction. Numerically, it can be simulated as an accumulation of damage process. Since the resistance of concrete material reduces drastically after the initiation of macroscopic cracks, fatigue life can be approximated using damage models as the number of cycles by which the material continuity vanishes. The fatigue scatter is an interpretation of material heterogeneity and uncertain external influences. It can be reproduced by treating the damage evolution as a stochastic process.

Inspired by the application of the stochastic process in molecular physics, the deterministic damage evolution rate of the Lemaitre model is modified as a stochastic differential equation to characterise the random damage increment. The implicit Euler scheme associated with Monte-Carlo simulation is demonstrated as a practical approach to solve the stochastic integration problem. The stochastic damage model is designed carefully to obey the thermodynamic principles and the deterministic damage law. Particular efforts are addressed to determine suitable random distributions, avoiding negative random damage increments in individual realisations, to have a statistically unbiased mean. To adequately approximate the high-cycle fatigue damage with random noise, the "jumping-cycle" algorithms with different extrapolation strategies are investigated.

This damage model is further implemented in the simulation of four-point flexural fatigue of concrete beam, solved by the finite element method. The numerically reproduced fatigue data closely fit the published experimental results and the empirical solution, both in the mean and standard deviation. Compared to the Gaussian white noise, the Weibull random variable has broad applicability to simulate random fatigue damage and other physical processes.

ISBN 978-3-935732-54-3